



A Systematic View of Ten New Black Hole Spins

Paul A. Draghis¹ , Jon M. Miller¹ , Abderahmen Zoghbi^{2,3,4} , Mark Reynolds^{1,5} , Elisa Costantini^{6,7} , Luigi C. Gallo⁸, and John A. Tomsick⁹

¹ Department of Astronomy, University of Michigan, 1085 South University Avenue, Ann Arbor, MI, 48109, USA; pdraghis@umich.edu

² Department of Astronomy, University of Maryland, College Park, MD, 20742, USA

³ HEASARC, Code 6601, NASA/GSFC, Greenbelt, MD, 20771, USA

⁴ CRESST II, NASA Goddard Space Flight Center, Greenbelt, MD, 20771, USA

⁵ Department of Astronomy, Ohio State University, 140 W 18th Avenue, Columbus, OH, 43210, USA

⁶ SRON Netherlands Institute for Space Research, Niels Bohrweg 4, 2333 CA Leiden, The Netherlands

⁷ Anton Pannekoek Astronomical Institute, University of Amsterdam, P.O. Box 94249, 1090 GE Amsterdam, The Netherlands

⁸ Department of Astronomy & Physics, Saint Mary's University, 923 Robie Street, Halifax, Nova Scotia, B3H 3C3, Canada

⁹ Space Sciences Laboratory, 7 Gauss Way, University of California, Berkeley, CA, 94720-7450, USA

Received 2022 October 5; revised 2022 December 11; accepted 2023 January 2; published 2023 March 22

Abstract

The launch of NuSTAR and the increasing number of binary black hole (BBH) mergers detected through gravitational wave observations have exponentially advanced our understanding of BHs. Despite the simplicity owed to being fully described by their mass and angular momentum, BHs have remained mysterious laboratories that probe the most extreme environments in the universe. While significant progress has been made in the recent decade, the distribution of spin in BHs has not yet been understood. In this work, we provide a systematic analysis of all known BHs in X-ray binary systems (XBs) that have previously been observed by NuSTAR, but have not yet had a spin measurement made using the “relativistic reflection” method obtained from those data. By looking at all the available archival NuSTAR data of these sources, we measure 10 new BH spins: IGR J17454-2919 – $a = 0.97^{+0.03}_{-0.17}$; GRS 1758-258 – $a = 0.991^{+0.007}_{-0.019}$; MAXI J1727-203 – $a = 0.986^{+0.012}_{-0.159}$; MAXI J0637-430 – $a = 0.97 \pm 0.02$; Swift J1753.5-0127 – $a = 0.997^{+0.001}_{-0.003}$; V4641 Sgr – $a = 0.86^{+0.04}_{-0.06}$; 4U 1543-47 – $a = 0.98^{+0.01}_{-0.02}$; 4U 1957+11 – $a = 0.95^{+0.02}_{-0.04}$; H 1743-322 – $a = 0.98^{+0.01}_{-0.02}$; and MAXI J1820+070 – $a = 0.988^{+0.006}_{-0.028}$ (all uncertainties are at the 1σ confidence level). We discuss the implications of our measurements on the entire distribution of stellar-mass BH spins in XBs, and we compare them with the spin distribution in BBHs, finding that the two distributions are clearly in disagreement. Additionally, we discuss the implications of this work on our understanding of how the “relativistic reflection” spin measurement technique works, and discuss possible sources of systematic uncertainty that can bias our measurements.

Unified Astronomy Thesaurus concepts: BHs (162); Stellar mass BHs (1611); Astrophysical BHs (98); Accretion (14); X-ray binary stars (1811)

1. Introduction

It is believed that black holes (BHs) were first thought of almost 240 yr ago (Michell 1784), and then rediscovered 132 yr later, in 1915, when Karl Schwarzschild found a solution of general relativity that would describe a BH (Schwarzschild 1999). In 1972, 57 yr later, multiple independent studies concluded that the system Cygnus X-1 must harbor a BH (Bolton 1972; Tananbaum et al. 1972; Webster & Murdin 1972), making this the first BH detected through electromagnetic radiation. In 2015, 43 yr later, gravitational wave (GW) signals from the merging event of two BHs was first detected (Abbott et al. 2016), and only three years later, the first direct image of the shadow of a Kerr BH was obtained (Event Horizon Telescope Collaboration et al. 2019). Even though our understanding of BHs has grown exponentially in the past few decades, and even though BHs are intrinsically simple objects described entirely by their mass and angular momentum, many questions remain unanswered. This includes, perhaps most interestingly, a complete understanding of the origin and magnitude of BH rotation.

The third Gravitational Wave Transient Catalog (GWTC-3; The LIGO Scientific Collaboration et al. 2021a) contains 90 probable GW candidates of merging events observed by Advanced LIGO (aLIGO) and Advanced Virgo (AdV). On this sample, The LIGO Scientific Collaboration et al. (2021b) inferred that the spin distribution of the most rapidly spinning BH of the two in the binary black hole (BBH) system peaks near 0.4,¹⁰ with the 1st and 99th percentiles at $0.07^{+0.05}_{-0.03}$ and 0.80 ± 0.08 , respectively, while the spin distribution of the less rapidly spinning BHs in BBH peaks around 0.2, with 99% of the distribution below $0.54^{+0.09}_{-0.08}$. The spin distribution in these systems is inconsistent with the spin distribution in X-ray binary systems (XBs) at more than 99.9% confidence (Fishbach & Kalogera 2022), hinting at different formation mechanisms between the two populations of BHs. However, it is important to mention that the BH spins obtained based on GW measurements are not directly measured from the observations, rather they are calculated using various models and theoretical assumptions based on the observable quantities in the GW events.



Original content from this work may be used under the terms of the [Creative Commons Attribution 4.0 licence](#). Any further distribution of this work must maintain attribution to the author(s) and the title of the work, journal citation and DOI.

¹⁰ The dimensionless spin parameter is given by $a = cJ/GM^2$, where, in general, $-0.998 \leq a \leq 0.998$ (Thorne 1974). However, for the BHs in a BBH system, the absolute magnitude of the spin and the orientation of the spin vector are reported.

Current estimates (Abbott et al. 2020a) predict that with KAGRA joining the aLIGO/AdV collaboration and with the detectors reaching their designed sensitivity, 79^{+89}_{-44} BBH mergers are expected to be detected during O4, which is expected to begin in 2023 May. In the near future, the distribution of spin measurements both pre- and post-merger will become increasingly statistically significant. In contrast, there have been ~ 70 XB BH candidates discovered since the beginning of the era of X-ray astronomy, of which only ~ 20 have been confirmed dynamically (see the updated results of Corral-Santana et al. 2016). In addition to the $\sim 1\text{--}3$ new BH candidates discovered every year, this number is expected to increase significantly in the future, in the era of 30 m optical telescopes and X-ray probes such as AXIS (Mushotzky et al. 2019). By looking at the distribution of BH spins in XB and comparing it to that of the spins in BBH mergers, we begin to look into the final destiny of stars, the origin of BHs, and the nature of BBH systems. Fully describing the two distributions of BH spins is essential to providing a unified understanding of stellar-mass BH formation and evolution. This will help us to understand the entire BH population, whether or not the two seemingly distinct BH populations have a common origin, and what factors might lead to different median properties. It is therefore important to measure spins in the greatest possible number of stellar-mass BHs in XB.

The spins of BHs in XB are most often measured through either continuum fitting (see e.g., Gou et al. 2009; Steiner et al. 2012; Sreehari et al. 2020; Zhao et al. 2021) or relativistic disk reflection (see, e.g., Brenneman & Reynolds 2006; Miller et al. 2009; Draghis et al. 2020b; Dong et al. 2022). For a detailed review of BH spin measurement techniques, see Reynolds (2021). Continuum fitting models the shape of the emission from the accretion disk around a BH, but requires prior knowledge of the BH mass, distance to the system, accretion rate, and inclination of the inner accretion disk. Additionally, continuum fitting measurements depend on an assumption of the spectral hardening factor and the nature of the hard emission (i.e., direct and reflected coronal emission) in the observations.

Relativistic reflection (George & Fabian 1991) models the distortion of spectral features (mainly the Fe K α spectral line, present at 6.4 keV for neutral gas, and the Compton hump present above ~ 20 keV) in order to infer the proximity of the emitting matter to the BH. The fluorescent Fe K line is produced when one of the two K-shell electrons of an Fe atom is ejected by an ionizing X-ray photon incoming from the compact corona. Following the photoionization, an L-shell electron can decay to the K shell by releasing 6.4 keV of energy either as a photon (with 34% probability) or as an Auger electron (with 66% probability). As an Fe atom becomes more ionized, the reduced number of screening electrons in the upper shells increases the energy difference between the K and L shells, therefore causing the fluorescent photons to be emitted with progressively higher energies, up to 6.97 keV for H-like Fe XXVI, where due to the lack of electrons in the K shell, the Auger effect cannot occur and the Fe K line is produced through recombination with a free electron. Unlike the soft incident X-ray photons which are preferentially absorbed by the accretion disk, the hard X-ray photons are preferentially Compton scattered, leading to a broad spectral shape above ~ 20 keV, referred to as the “Compton hump.”

By virtue of it being a relative measurement, this method infers distances from the BH in units of gravitational radii ($r_g = GM/c^2$), making it an ideal tool for measuring the spin of BHs for which there are no mass or distance estimates. However, while relativistic reflection does not require prior information about the BH in the system, similarly to the continuum fitting method, it also depends on the assumption that the optically thick, geometrically thin accretion disk (Shakura & Sunyaev 1973) extends all the way to the innermost stable circular orbit (ISCO) and that matter within the ISCO is on plunging orbits and has no time to contribute significantly to the observed flux. As the size of the ISCO is determined by gravity (Bardeen et al. 1972; Novikov & Thorne 1973), relativistic reflection measures the size of the BH’s ISCO, directly probing the BH spin. The assumption of an inner disk edge consistent with the ISCO is motivated by numerical simulations (see, e.g., Reynolds & Fabian 2008; Shafee et al. 2008; Schnittman et al. 2016) and observational results (see, e.g., Steiner et al. 2010; Salvesen et al. 2013; García et al. 2015) suggesting that for Eddington fractions between $10^{-3} \lesssim L_{\text{disk}}/L_{\text{Edd}} \lesssim 0.3$, there is a sharp inner disk boundary, consistent with the ISCO. It is important to note that works such as Tomsick et al. (2009) and Xu et al. (2020a) find evidence of disk truncation at Eddington fractions of 0.14% and 0.18%, suggesting that while possible in the low Eddington regime, it is not always a requirement for the accretion disk to extend to the ISCO.

Additionally, relativistic reflection depends on assumptions regarding the properties of the compact corona that produces the radiation incident of the disk, which is then reprocessed (“reflected”). Most current models either assume a “lamp-post” geometry, or parameterize the emissivity of the corona in terms of radial emissivity indices, which remove the need for a geometrical description of the corona. Lastly, the inclination of the inner disk regions also has an effect on determining spectral features, and is usually treated as a free parameter in reflection models. While some studies assume that the inclination of the inner disk is the same as the orbital inclination, it is not necessarily the case, and the two can be different due to disk tearing and the Bardeen–Petterson effect (Bardeen & Petterson 1975; Nealon et al. 2015; Liska et al. 2021).

The launch of NuSTAR (Harrison et al. 2013) in 2012 revolutionized relativistic reflection spin measurements, with the size of the sample of measured stellar-mass BH spins more than tripling through the addition of measurements made using NuSTAR data. This improvement is attributable to the wide bandpass that NuSTAR offers, the high sensitivity and spectral resolution at high energies, and the fact that the instrument does not suffer from effects such as pileup. The top panels of Figure 1 show the product of the effective area and the live-time fraction of some major X-ray observatories and the bottom panels show the typical number of counts as a function of the number of resolution elements in the 5–7 keV (left) and 20–40 keV (right) bands, with the size of the points being proportional to the signal-to-noise ratio (S/N). The number of counts was estimated for a source with a flux of 1 Crab, accounting for the effective area of the instrument, the live-time fraction, and an estimated typical duration of an observation obtained through an analysis of archival observations. In the 5–7 keV band, NuSTAR offers a combination of high S/N, large number of counts, and sufficient number of resolution elements to observe accurately the shape of the Fe K line. In the 20–40 keV band,

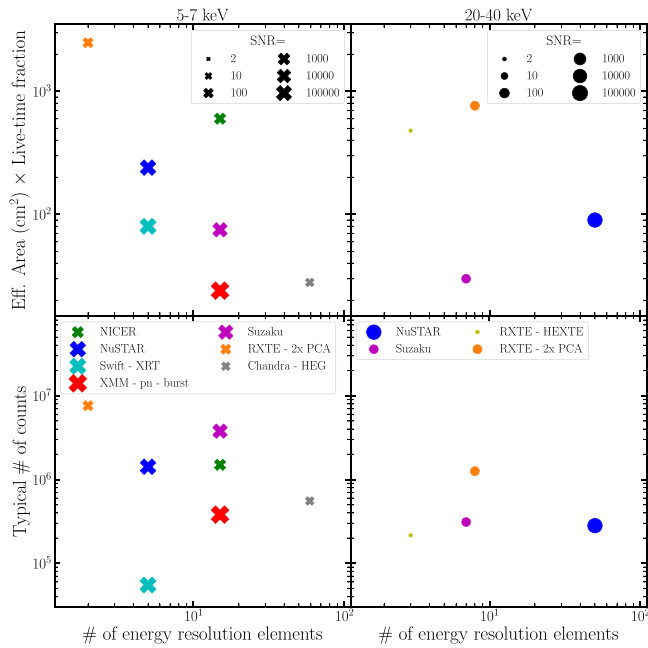


Figure 1. The top panels show the effective area multiplied by the approximate live-time fraction during observations vs. the number of energy resolution elements in the 5–7 keV (left) and 20–40 keV (right) bands for some major X-ray observatories. The bottom panels show the typical number of counts per observation vs. the number of energy resolution elements in the same bands. The point sizes are proportional to the typical S/N during the observations. All values are estimated for a source with a flux of 1 Crab, using typical exposure duration for each observatory: 20 ks for NuSTAR, 5 ks for NICER, 1 ks for Swift, 20 ks for XMM-Newton, 80 ks for Suzaku, 5 ks for RXTE, and 30 ks for Chandra.

when compared to other instruments, NuSTAR provides unparalleled capabilities to describe the Compton hump feature of reflection spectra. All these advantages make NuSTAR the most appropriate instrument for spin measurements through relativistic reflection.

There are (on the order of ~ 40) examples of individual BH spin measurements in papers adopting different methods. Additionally, most spin measurements report only statistical uncertainties, while the systematic uncertainties of the methods have not yet been properly understood, due to the effects mentioned above. This is particularly important for measurements such as that of MAXI J1803-298, where Feng et al. (2022c) found $a = 0.991 \pm 0.001$, or of EXO 1846-031, where Draghis et al. (2020b) measured $a = 0.997^{+0.001}_{-0.002}$, where even though the accuracy is probably very high, the precision of the measurement is likely overestimated.

We aim to make a comprehensive, uniform treatment of BH spin with entirely consistent methods and systematic errors, which is needed in order to understand completely the events that create BHs, the evolution of BHs in binary systems, accretion onto BHs, the relativistic effects on the matter surrounding them, and the origins of the population of massive BHs in binary mergers observed through GWs. Therefore, we analysed the entire sample of archival NuSTAR observations of XBs harboring BHs that did not previously have a spin measurement obtained through relativistic reflection from NuSTAR data. The sources were selected initially based on the BHs identified in the WATCHDOG (Tetarenko et al. 2016) and BackCAT (Corral-Santana et al. 2016) catalogs, followed by a survey of journal literature indicating BH candidates. We excluded sources that presented evidence of thermonuclear

bursts (or burst-like behavior) in order to exclude neutron star candidates. We analysed 24 sources across 115 observations, and measured 10 new BH spins. We describe our data analysis methods in Section 2, we present the analysis that led to the 10 new measurements in Section 3, and discuss the sources for which a spin measurement was not possible in Appendix C. In Section 4, we present the updated distribution of BH spins in XBs. Lastly, we summarize our results and discuss their implications in Section 5.

2. Data Analysis

All the NuSTAR spectra were extracted using the nustardas v2.1.1 routines in Heasoft v6.29c, using the NuSTAR CALDB version 20211103. The spectra from the two NuSTAR FPM detectors were extracted from circular regions with $120''$ radius centered at the location of the source, taken from the header of the event file. Background spectra were extracted from annuli with an inner radius of $200''$ and an outer radius of $300''$, concentric with the source region, and subtracted from the source spectra. Our choice of background region does not significantly change the background spectrum when compared to the spectrum extracted from a circular background region selected on a different location on the detector. This is especially the case since the observed sources are generally bright, with count rates larger than a few counts per second. For additional explanation regarding this choice of source and background regions, together with the impact that this might have on the reported results, see Appendix A. The spectra are then binned using the “optimal” binning scheme presented by Kaastra & Bleeker (2016), using the “ftgrouppha” ftool, and truncated at the energy where the background emission begins to dominate over the source spectrum.

The spectral analysis was performed using Xspec v12.12.0g (Arnaud 1996), using χ^2 statistics with standard weighting, and using the leven minimization method. Throughout the analysis, we used the wilms abundances (Wilms et al. 2000) and the vern photoelectric absorption cross sections (Verner et al. 1996).

When fitting NuSTAR spectra from the two FPM detectors, it is customary to link all parameters of the model for the spectra from the two detectors and to allow a multiplicative constant offset between the spectra. However, this sometimes produces different residuals when fitting the two spectra, especially at low energies ≤ 5 keV (see, e.g., Draghis et al. 2023). Therefore, instead of adopting a multiplicative constant to account for the difference between the spectra from the two FPM NuSTAR detectors, we allowed the normalizations of the model components to be different for the models describing the two spectra, linking all other parameters. This method not only accounts for differences in the absolute flux sensitivity between the detectors, but also for possible variations in spectral response. For example, instead of fitting the two spectra with the model `constant *TBabs * (diskbb+powerlaw)` and linking all parameters except for the `constant` component, we fit the two spectra using the model `TBabs * (diskbb+powerlaw)`, but allowing the normalization of the `diskbb` and `powerlaw` components to vary between the two detectors and linking all other parameters, therefore introducing one extra free parameter. Despite having one extra free parameter, the quality of the fits is almost always significantly improved by allowing free normalizations when compared to having a multiplicative constant account for the

difference between spectra, and the parameters of the models are not generally strongly influenced. By using this method, the fits can better constrain the shape of the continuum without forcing the reflection features to account for instrumental differences between the detectors. This allows us to distinguish more clearly the reflection features from the underlying continuum.

2.1. Choice of Models

In order to test the possible systematic effects introduced through our choice of models, throughout our analysis we start by fitting spectra with a baseline array of seven models. First, all models include a `TBabs` component in order to describe galactic absorption along the line of sight, using the value estimated by the web version of the N_{H} column density FTOOL¹¹ for each source as a starting point. The value of the column density does significantly influence the quality of the fits. With NuSTAR offering excellent sensitivity across a broad bandpass, the continuum is well determined and so, the column density can also be well constrained. In previous similar studies, the column density is usually not correlated with the measured spin value, provided that the low-energy continuum is properly modeled. Second, in order to describe emission from the accretion disk, we include a `diskbb` component to all models, even those describing observations that occurred during particularly hard states. If the `diskbb` component is not required by the model, the temperature of the disk and/or the normalization of the component will be driven to values indicating that the component does not contribute significantly to the model. Lastly, to describe coronal emission, we add a `powerlaw` component. While this does not probe the effects of relativistic reflection, it allows us to quantify statistically if reflection is present: we can compare this to the quality of the fit with models that account for reflection in order to probe if reflection is indeed present. This gives us the first model variation, in Xspec language `TBabs * (diskbb + powerlaw)`.

In order to model the reflection features, we used the `relxill` v.1.4.3 (Dauser et al. 2014; García et al. 2014) family of models. For a complete description of the models, their variations, and of all model parameters, see the website of the model,¹² Section 3.1 in Draghis et al. (2021b), or Appendix A in Draghis et al. (2023). We note that since the analysis was performed, an updated version of `relxill` was launched (v2.0—Dauser et al. 2022) that includes the effects of returning radiation on the observed spectra. However, since the main focus of the paper is to measure the spins of the compact objects in the systems, and since the addition of returning radiation does not influence spin measurements significantly (see Figure 12(b) in Dauser et al. 2022), we chose to continue using version 1.4.3 in our analysis.

To probe the extent of the theoretical assumptions of the `relxill` family of models, we replace the `powerlaw` component with six variations of the `relxill` components. In order to test the effect of the assumption regarding the shape of the underlying continuum, we test both the simple `relxill` variant and `relxillCp`. To test the effect of the assumed coronal geometry, we also test the `relxilllp` variant, which assumes a “lamp-post” geometry, while the previous two

models attempt to measure the coronal emissivity directly, without assuming a “lamp-post” geometry. Lastly, in order to probe the effect of the density of the accretion disk, we also tested the `relxillD` variant. However, when allowing the disk density to vary, it is almost always unconstrained by the fits, as the effects of higher disk densities are mainly noticeable at energies below the lower limit of the NuSTAR bandpass. Pairing NuSTAR data with spectra with lower energy coverage such as NICER or Swift/XRT, and in the future, HEX-P (Madsen et al. 2018), will allow for more careful constraints of accretion disk density. Therefore, we test three variations of the `relxillD` component, by fixing the disk density at $n = 10^{15}$, 10^{17} , and 10^{19} cm^{-3} . This gives us the array of six reflection components that we used to describe relativistic reflection, by replacing the `powerlaw` component in our first model variation. We leave all other parameters in the models free, with the exception of the outer disk radius, which we fix at $r_{\text{out}} = 990 r_g$. As the radial emissivity profiles of the coronal emission are generally steep, the outer regions of the disk contribute insignificantly to the total observed emission, making the outer disk radius nearly impossible to constrain for such systems. Therefore, we fixed this parameter at nearly the maximum value allowed in the model. Additionally, unless otherwise noted, we fix the inner disk radius at $r_{\text{in}} = r_{\text{ISCO}}$ for observations that occur while the source was at an Eddington fraction between $10^{-3} \lesssim L_{\text{disk}}/L_{\text{Edd}} \lesssim 0.3$, calculated using the flux in the 0.1–10 keV band and the measurements in the literature for the BH mass and distance to the systems. Where no mass or distance measurements were available, we analyse the observations that fall within this Eddington fraction range when assuming generic values for these parameters (e.g., $M_{\text{BH}} \sim 8 \pm 4 M_{\odot}$ and $d \sim 10 \pm 5 \text{ kpc}$).

2.2. MCMC Analysis

After fitting the data with our baseline array of models and finding the best-fit solution for each `relxill` variant tested, we ran a Markov Chain Monte Carlo (MCMC) analysis on the models performing best in terms of the χ^2 statistic. In cases where identifying the best-performing models was not trivial, we calculated the Akaike Information Criterion (AIC; Akaike 1974) and the Bayesian Information Criterion (BIC; Schwarz 1978) using the following formulas:

$$\text{AIC} = N \ln(\chi^2/N) + 2N_{\text{var}}, \quad (1)$$

$$\text{BIC} = N \ln(\chi^2/N) + \ln(N)N_{\text{var}}, \quad (2)$$

where N is the number of data bins and N_{var} is the number of variables in the model.

We used the best-fit parameter combination to generate a Gaussian proposal distribution for initiating the walkers in the MCMC analysis, and used uniform priors in the range allowed by the parameters in the model. For running the MCMC analysis, we used the Xspec `emcee` implementation written by A. Zoghbi.¹³ We chose the number of walkers in the analysis as a large integer, on the order of several (4–5) times the number of free parameters in the analysis. In order to ensure chain convergence, we ran the chains for $3\text{--}4000 \times \tau_f$, where τ_f

¹¹ <https://heasarc.gsfc.nasa.gov/cgi-bin/Tools/w3nh/w3nh.pl>

¹² <http://www.sternwarte.uni-erlangen.de/dauser/research/relxill/>

¹³ https://zoghbi-a.github.io/xspec_emcee/

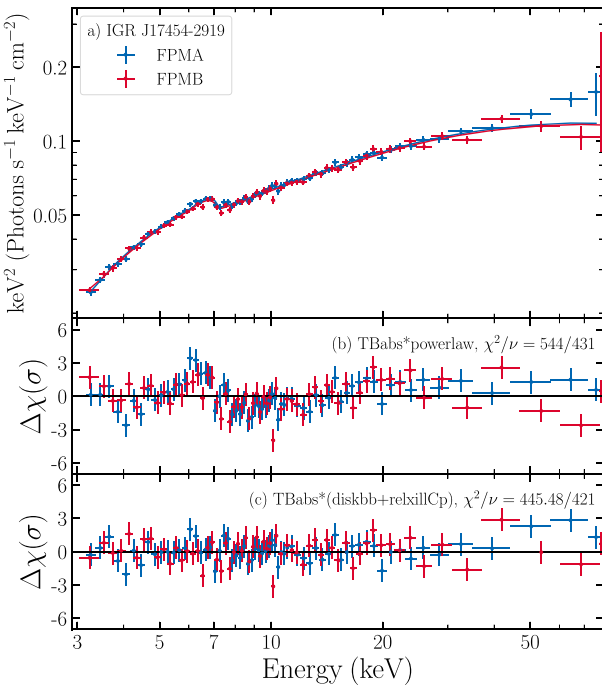


Figure 2. Top: unfolded spectrum of IGR J17454-2919, with the NuSTAR FPMA spectrum shown in blue and FPMB spectrum in red. The reported best-fit model is shown by the solid lines. The middle and bottom panels show the residuals in terms of σ produced when fitting the spectra with TBabs * powerlaw (middle) and TBabs * (diskbb+relxillCp) (bottom), together with the statistic produced.

represents the integrated autocorrelation time (Sokal 1996 recommend running the chains with more steps than $\sim 1000 \times \tau_f$ in order to ensure convergence). Therefore, we ran the MCMC chains with 200 walkers for a total of 2.5×10^6 steps, and disregarded the first 5×10^5 steps of the chains as a “burn-in” phase.

When running the MCMC analysis on more than one model, we also computed the Deviance Information Criterion (DIC; Spiegelhalter et al. 2002) and reported the model that performs best in terms of DIC. We computed the DIC using:

$$\text{DIC} = \overline{D(\theta)} + p_D, \quad (3)$$

where θ represents the unknown parameters in the model, $D(\theta)$ represents the deviance, computed as $D(\theta) = -2 \log(p(y|\theta)) + C$ (where y represents the data, $p(y|\theta)$ is the likelihood function, and C is some constant which cancels out when comparing models), and p_D represents the effective number of parameters of the model, computed as $p_D = \frac{1}{2} \overline{\text{var}(D(\theta))}$ (Gelman et al. 2004). This information criterion has the advantage of probing not only the best-fit solution, but also the shape of the entire posterior distribution of the parameter space around the best solution.

The MCMC analysis was run for each individual observation. For sources with multiple observations, this produces a number of measurements for each parameter in the models equal to the number of observations. We report the modes of the posterior distributions and the 1σ highest posterior density credible intervals of our measurements in Tables 1–5. We chose to report the modes of the posterior distributions instead of the medians in order to highlight the value that occurs most

often in the MCMC analysis for each parameter, suggesting a higher preference for the specific value.

Additionally, throughout the paper, we chose to report the 1σ highest posterior density credible intervals (i.e., the shortest interval in the posterior distribution of a parameter that contains 68.3% of the posterior samples) instead of an equal-tailed confidence interval (i.e., having an equal number of samples below the interval as above it) as this is better suited for distributions that are clustered around the edge of a parameter space. As an example, this is often the case for extremely high spin measurements.

2.3. Combining Measurements

When there are multiple measurements of the same parameter (i.e., BH spin or inclination), it can be difficult to report a single value. While one could choose to report the parameter combination from a single observation, such as the one with the highest total number of counts in the observation, the one happening during the hardest spectral state, or the one where the reflection strength is the highest relative to the continuum, this inevitably leads to a loss of information from the other observations. An alternative that takes advantage of all available data is to fit all spectra simultaneously, and link parameters that are expected to remain constant throughout the observations, such as the BH spin and the inclination of the inner disk, ensuring that the values measured are constrained by all the spectra at the same time. While this method would be the ideal way forward to ensure that all data are fully used, jointly fitting multiple NuSTAR spectra with complicated models that include multiple components becomes a very slow, computationally intensive process. In practice, fitting more than 2–3 observations, each having two spectra, becomes nearly impossible, with each iteration in the χ^2 minimization algorithm in Xspec lasting on the order of tens of seconds to minutes. With the time required to run each iteration increasing significantly through the addition of extra spectra, fitting ~ 10 observations simultaneously (for sources such as 4U 1957+11, H 1743-322, or MAXI J1820+070) is currently impossible due to limited computing power. Additionally, even if one were to find the parameter combination for which the best fit is achieved, running the MCMC analysis described in Section 2.2 would be an even more computationally demanding process, by many orders of magnitude.

Therefore, due to these limitations, we ran our analysis by fitting the spectra produced by each observation individually. We did, however, simultaneously fit the two spectra produced by the two FPM NuSTAR detectors during the same observation, as described at the beginning of Section 2. We implemented a Bayesian method of combining measurements from multiple observations into a single value, which we report. While most parameters in the models are not expected to stay constant in time, the BH spin, the inclination of the inner accretion disk, and the Fe abundance are not likely to change in time. However, due to possible correlations between the assumed disk density in the model and the Fe abundance (see, e.g., Tomsick et al. 2018), we do not report a combined Fe abundance measurement, but we do report the individual Fe abundance obtained from each observation in the tables in Tables 1–5 for future exploration of the models. Therefore, throughout the paper, for sources that have been observed more than once, we report the spin and inclination obtained by combining the measurements from individual observations, and

Table 1
Results of the MCMC Analysis for IGR J17454-2919, GRS 1758-258, MAXI J1727-203, Swift J1753.5-0127, and MAXI J0637-430

ObsID	IGR J17454-2919	GRS 1758-258	MAXI J1727-203	Swift J1753.5-0127	MAXI J0637-430		
	80001046002	30401030002	90401329002	80001047002	80502324002	80502324004	80502324006
$N_{\text{H}} [\times 10^{22} \text{ cm}^{-2}]$	$8.7^{+0.8}_{-0.3}$	$3.7^{+1.2}_{-0.8}$	6^{+1}_{-2}	$0.2^{+1.0}_{-0.2}$	$0.006^{+0.069}_{-0.005}$	$0.019^{+0.092}_{-0.009}$	$0.03^{+0.17}_{-0.02}$
$kT_{\text{in}} [\text{keV}]$	$0.15^{+0.03}_{-0.11}$	$0.56^{+0.03}_{-0.05}$	$0.56^{+0.02}_{-0.03}$	$0.49^{+0.01}_{-0.01}$	$0.639^{+0.002}_{-0.003}$	$0.599^{+0.003}_{-0.003}$	$0.544^{+0.003}_{-0.004}$
norm _{d,A}	$8e + 06^{+8e+07}_{-8e+06}$	168^{+80}_{-74}	239^{+70}_{-80}	585^{+172}_{-140}	$2e + 03^{+6e+01}_{-6e+01}$	$2e + 03^{+6e+01}_{-8e+01}$	$2e + 03^{+1e+02}_{-9e+01}$
q_1	$9.8^{+0.2}_{-3.6}$	$8.2^{+0.8}_{-3.0}$	$9.8^{+0.2}_{-2.7}$	$9.5^{+0.5}_{-1.3}$	$9.9^{+0.1}_{-1.0}$	$9.9^{+0.1}_{-1.3}$	$9.9^{+0.1}_{-2.1}$
q_2	$0.9^{+0.9}_{-0.9}$	$0.1^{+1.8}_{-0.1}$	$1e - 07^{+1e-07}_{-1e-07}$	4^{+4}_{-1}	$1e - 10^{+2e-03}_{-1e-10}$	$2.5^{+0.5}_{-1.5}$	$2.5^{+0.5}_{-1.3}$
$R_{\text{br}} [r_g]$	8^{+30}_{-3}	23^{+40}_{-18}	25^{+6}_{-18}	$2.9^{+29.8}_{-0.9}$	95^{+5}_{-41}	84^{+16}_{-44}	95^{+5}_{-55}
a	$0.97^{+0.03}_{-0.17}$	$0.991^{+0.007}_{-0.019}$	$0.99^{+0.01}_{-0.16}$	$0.997^{+0.001}_{-0.003}$	$0.989^{+0.004}_{-0.005}$	$0.977^{+0.008}_{-0.013}$	$0.987^{+0.006}_{-0.013}$
$\theta [{}^{\circ}]$	60^{+8}_{-14}	66^{+8}_{-5}	64^{+10}_{-7}	74^{+3}_{-3}	67^{+2}_{-3}	61^{+2}_{-4}	67^{+2}_{-10}
Γ	$1.73^{+0.03}_{-0.02}$	$1.63^{+0.01}_{-0.01}$	$1.68^{+0.03}_{-0.03}$	$2.00^{+0.04}_{-0.03}$	$2.26^{+0.03}_{-0.03}$	$2.22^{+0.02}_{-0.01}$	$2.44^{+0.26}_{-0.03}$
$\log(\xi)$	$2.7^{+0.3}_{-0.4}$	$3.7^{+0.2}_{-0.1}$	$4.0^{+0.1}_{-0.2}$	$1.7^{+0.6}_{-0.9}$	$3.7^{+0.1}_{-0.3}$	$3.67^{+0.05}_{-0.22}$	$3.9^{+0.5}_{-2.5}$
A_{Fe}	3^{+1}_{-1}	$2.5^{+0.7}_{-0.6}$	$1.0^{+1.3}_{-0.5}$	5^{+2}_{-1}	$9.9^{+0.1}_{-1.3}$	$9.95^{+0.05}_{-0.5}$	$9.8^{+0.2}_{-1.9}$
$kT_e [\text{keV}]$	29^{+317}_{-28}	159^{+126}_{-78}	409^{+249}_{-194}	218^{+119}_{-120}	...	$1e + 03^{+2e+01}_{-2e+02}$	$1e + 03^{+2e+01}_{-4e+02}$
R	$0.28^{+0.17}_{-0.07}$	$0.6^{+0.3}_{-0.3}$	$0.7^{+0.3}_{-0.3}$	$2.3^{+0.8}_{-0.6}$	$1.1^{+0.2}_{-0.3}$	$0.7^{+0.1}_{-0.1}$	$0.8^{+1.8}_{-0.3}$
norm _{r,A}	$1e - 03^{+4e-05}_{-7e-05}$	$4e - 03^{+3e-04}_{-2e-04}$	$2e - 03^{+2e-04}_{-3e-04}$	$4e - 04^{+1e-05}_{-1e-05}$	$7e - 04^{+9e-05}_{-8e-05}$	$1e - 03^{+6e-05}_{-5e-05}$	$5e - 04^{+7e-04}_{-7e-05}$
norm _{d,B}	$2e + 07^{+2e+08}_{-2e+07}$	202^{+71}_{-89}	223^{+79}_{-64}	550^{+156}_{-137}	$2e + 03^{+6e+01}_{-5e+01}$	$2e + 03^{+6e+01}_{-7e+01}$	$2e + 03^{+1e+02}_{-8e+01}$
norm _{r,B}	$9e - 04^{+6e-05}_{-5e-05}$	$4e - 03^{+3e-04}_{-2e-04}$	$2e - 03^{+2e-04}_{-3e-04}$	$4e - 04^{+1e-05}_{-1e-05}$	$7e - 04^{+8e-05}_{-8e-05}$	$1e - 03^{+6e-05}_{-4e-05}$	$5e - 04^{+7e-04}_{-7e-05}$
χ^2/ν	$457^{+8}_{-5}(445.48)/421$	$452^{+6}_{-3}(442.56)/474$	$453^{+6}_{-5}(440.59)/442$	$398^{+5}_{-4}(385.18)/385$	$401^{+6}_{-4}(387.88)/296$	$392^{+7}_{-4}(382.78)/364$	$286^{+8}_{-5}(271.90)/237$

Note. In this table, we report the modes of the posterior distributions in the MCMC analysis, along with the 1σ credible intervals. For χ^2 , the number in parentheses indicates the best-fit χ^2 value. For the normalization of the components, the subscripts d (from `diskbb`) and r (from `relxill`) represent the model that the values correspond to, while the subscripts A and B represent which NuSTAR FMP detector from which the spectrum originated.

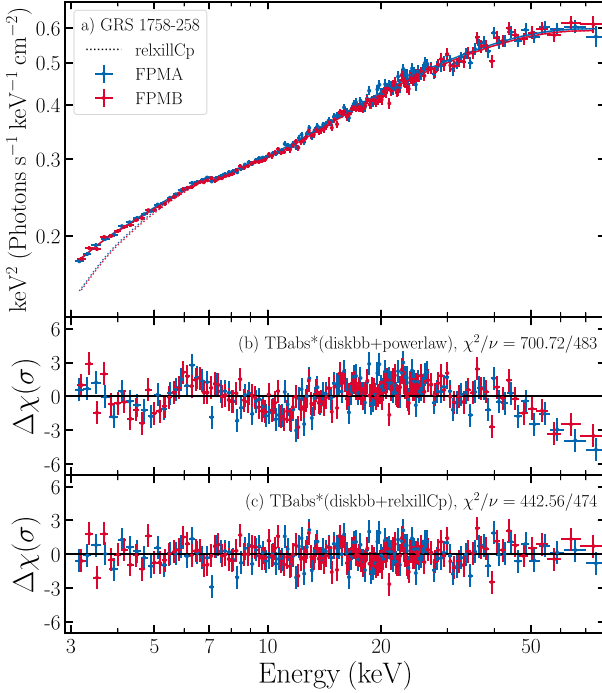


Figure 3. Top: unfolded spectrum of GRS 1758-258, with the NuSTAR FPMA spectrum shown in blue and FPMB spectrum in red. The reported best-fit model is shown by the solid lines, while the contribution of the `relxillCp` component is shown by the dotted lines. The middle and bottom panels show the residuals in terms of σ produced when fitting the spectra with $\text{TBabs}^* (\text{diskbb+powerlaw})$ (middle) and $\text{TBabs}^* (\text{diskbb+relxillCp})$ (bottom), respectively, together with the statistic produced.

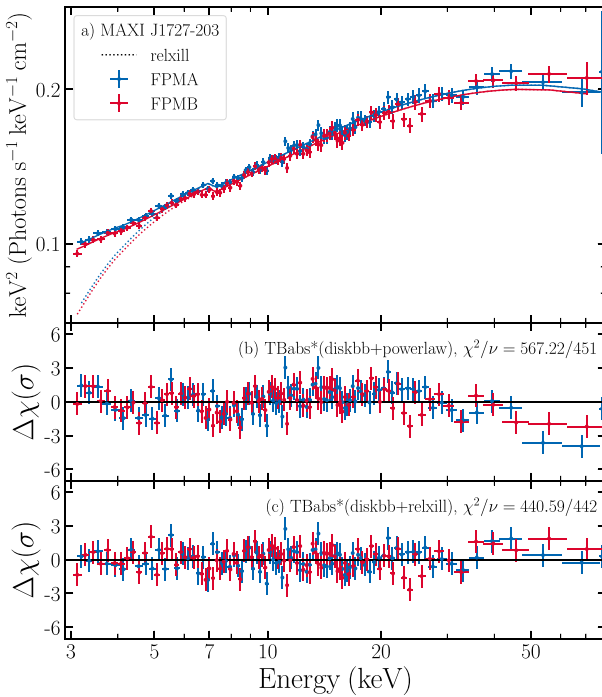


Figure 4. Top: unfolded spectrum of MAXI J1727-203, with the NuSTAR FPMA spectrum shown in blue and FPMB spectrum in red. The reported best-fit model is shown by the solid lines, while the contribution of the `relxill` component is shown by the dotted lines. The middle and bottom panels show the residuals in terms of σ produced when fitting the spectra with $\text{TBabs}^* (\text{diskbb+powerlaw})$ (middle) and $\text{TBabs}^* (\text{diskbb+relxill})$ (bottom), respectively, together with the statistic produced.

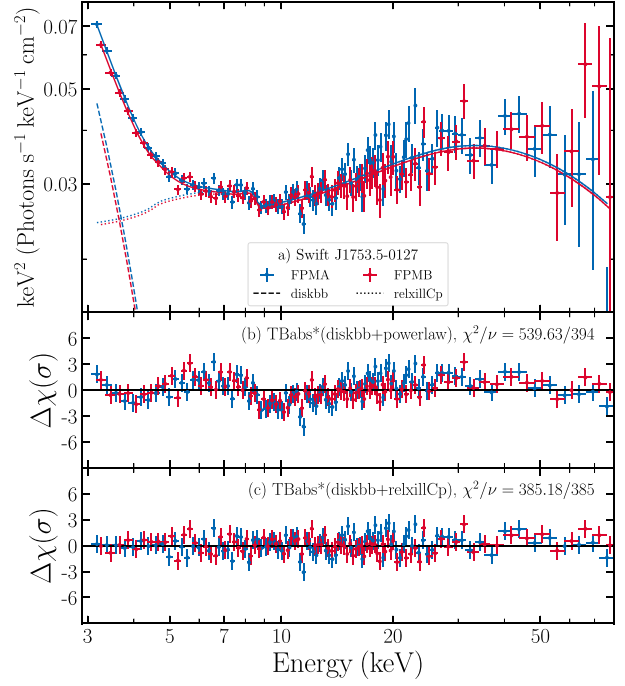


Figure 5. Top: unfolded spectrum of Swift J1753.5-0127, with the NuSTAR FPMA spectrum shown in blue and FPMB spectrum in red. The reported best-fit model is shown by the solid lines, while the contribution of the `relxillCp` component is shown by the dotted lines and the contribution of the `diskbb` component is shown through the dashed lines. The middle and bottom panels show the residuals in terms of σ produced when fitting the spectra with $\text{TBabs}^* (\text{diskbb+powerlaw})$ (middle) and $\text{TBabs}^* (\text{diskbb+relxillCp})$ (bottom), respectively, together with the statistic produced.

weight the contribution of each observation to the final measurement through the ratio of the reflected to total flux in the 3–79 keV band. For a detailed explanation of the method used to combine the results from multiple measurements and a comparison between this method and a joint, simultaneous fit of multiple observations, see Appendix B.

3. New Spins

3.1. IGR J17454-2919

At the time of the analysis, one NuSTAR observation of IGR J17454-2919 (ObsID 80001046002) was available in the archive. For this observation, we fit the entire 3–79 keV spectrum. Fitting with $\text{TBabs}^* \text{powerlaw}$ gives $\chi^2/\nu = 544/433$. Reflection features and soft emission consistent with an accretion disk are present. The spectra and residuals of the fits in terms of σ (i.e., $\frac{\text{data} - \text{model}}{\text{error}}$) are shown in Figure 2.

The best-performing model, both in terms of χ^2 and DIC, is $\text{TBabs}^* (\text{diskbb+relxillCp})$, with $\chi^2/\nu = 445.48/421$. Based on the MCMC analysis performed on this model, the measured spin is $a = 0.97^{+0.03}_{-0.17}$ and the inclination is $\theta = 60^{+8}_{-14}$ degrees. The full set of parameters determined through the MCMC analysis is presented in Table 1.

3.2. GRS 1758-258

Fitting the entire 3–79 keV NuSTAR spectrum of GRS 1758-258 from ObsID 30401030002 using $\text{TBabs}^* (\text{diskbb+powerlaw})$ gives $\chi^2/\nu = 700.72/483$, with the residuals clearly indicating reflection features (see Figure 3).

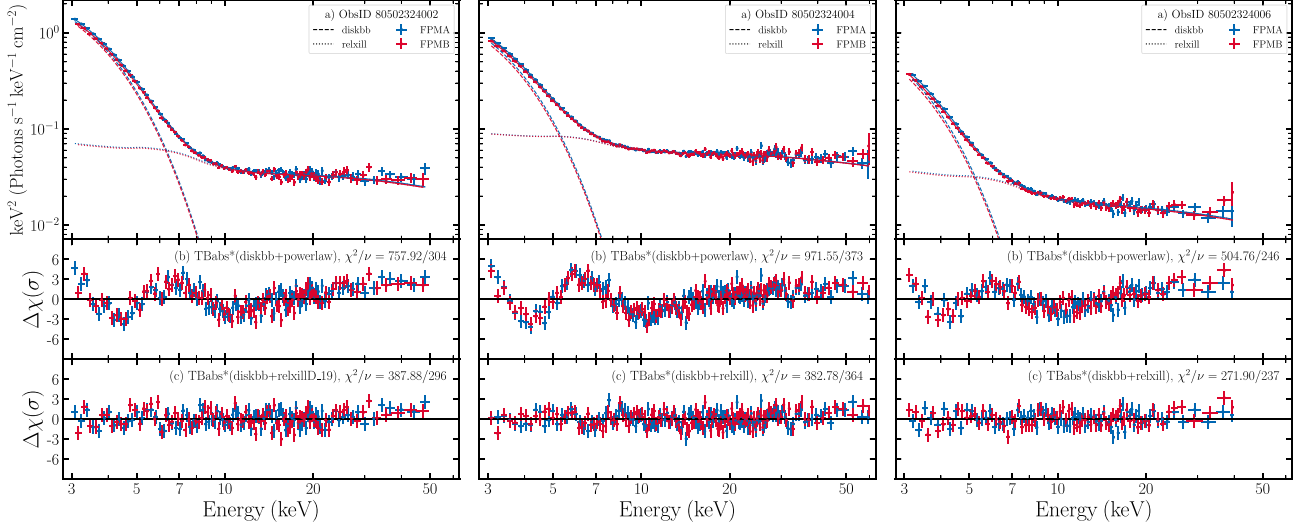


Figure 6. The three panels represent the three observations of MAXI J0637-430 analysed. The top subpanels show the unfolded spectra, with the NuSTAR FPMA spectra shown in blue and FPMB spectra in red. The reported best-fit models are shown by the solid lines, while the contributions of the `relxill` component are shown by the dotted lines and the contributions of the `diskbb` component are shown through the dashed lines. The middle and bottom subpanels show the residuals in terms of σ produced when fitting the spectra with $\text{TBabs} * (\text{diskbb+powerlaw})$ (middle) and $\text{TBabs} * (\text{diskbb+relxill})$ (bottom), respectively, together with the statistic produced.

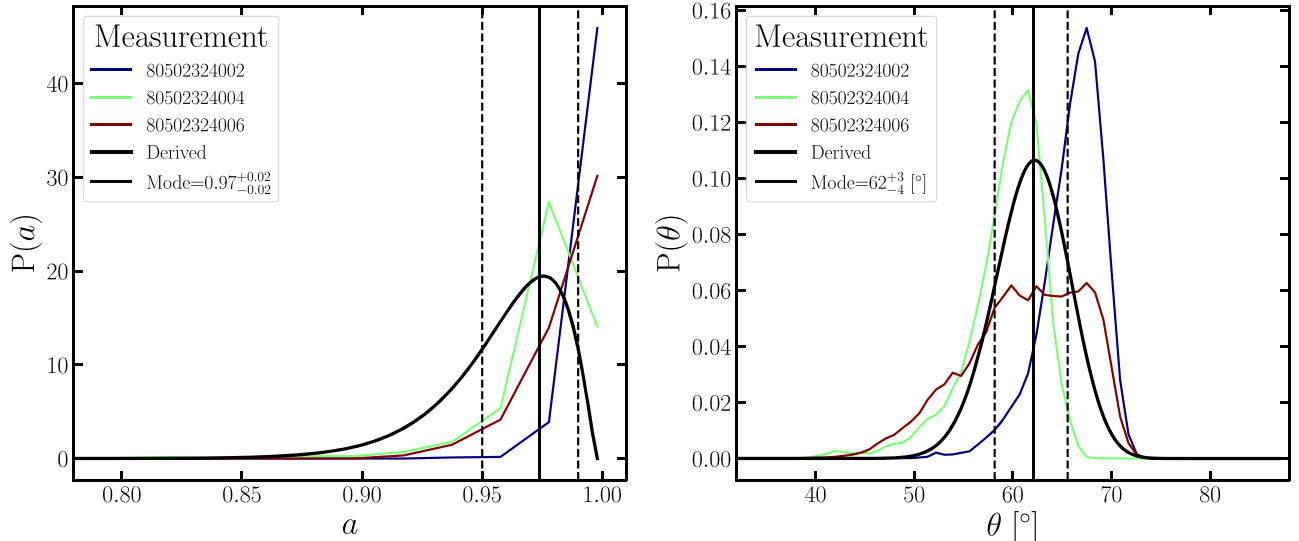


Figure 7. The left panel shows the posterior distributions resulting from the MCMC analysis of MAXI J0637-430 for spin, while the right panel shows the posterior distributions for the inclination of the inner accretion disk in the model. The different colored lines represent the three observations analysed, and the black curves represent the combined inferred distribution, with the transparency of the lines being proportional to the ratio of the reflected flux to the total flux in the 3–79 keV band, which were used as weighting when combining the posterior distributions. The solid vertical black lines represent the modes of the combined distribution, and the dashed vertical black lines represent the 1σ credible intervals of the measurements.

The three best-performing reflection models in terms of χ^2 and DIC are $\text{TBabs} * (\text{diskbb+relxillCp})$ ($\chi^2/\nu = 442.56/474$, DIC = 467.31), $\text{TBabs} * (\text{diskbb+relxillD})$ with log(n) = 19 ($\chi^2/\nu = 445.95/475$, DIC = 478.26), and $\text{TBabs} * (\text{diskbb+relxill})$ ($\chi^2/\nu = 449.65/474$, DIC = 475.2). Of the three models, $\text{TBabs} * (\text{diskbb+relxillCp})$ performs best both in terms of χ^2 and DIC. Therefore, we report the measurements of this model, but note that all measurements are consistent throughout the three models. Through the MCMC analysis we find $a = 0.991^{+0.007}_{-0.019}$ and $\theta = 66^{+8}_{-5}$ degrees. The entire set of parameters produced by the MCMC analysis is presented in Table 1.

We note that Jana et al. (2022) published a spin measurement for GRS 1758-258 shortly before the submission of this paper.

They measure $a > 0.92$, and our measurement is within good agreement. Additionally, we find a similar ionization parameter, Fe abundance, and reflection fraction. However, the inclination measurements and emissivity profiles are different, likely owing to the fact that their analysis did not include a `diskbb` component, which they argue was not statistically required by the data. We find that for all three models presented above, the `diskbb` component is required, both in terms of reduced χ^2 , AIC, and BIC. Therefore we continue to include the `diskbb` component in our analysis. The consistent spin measurements regardless of choice of continuum are encouraging when considering the systematic effects that act on these spin measurements. Since relativistic reflection works by disentangling the reflection features from the underlying

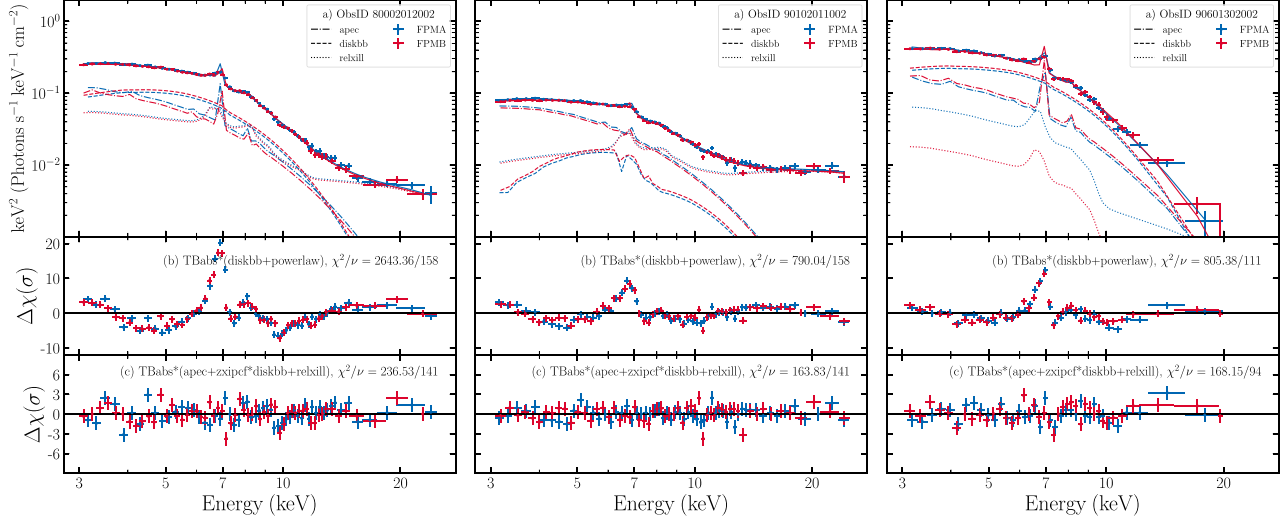


Figure 8. The three panels represent the three observations of V4641 Sgr analysed. The top subpanels show the unfolded spectra, with the NuSTAR FPMA spectra shown in blue and FPMB spectra in red. The reported best-fit models are shown by the solid lines, while the contributions of the `relxill` component are shown by the dotted lines, the contributions of the `diskbb` component are shown through the dashed lines, and the contributions of the `apec` component are shown in dotted-dashed lines. The middle and bottom subpanels show the residuals in terms of σ produced when fitting the spectra with $\text{TBabs}^* (\text{diskbb+powerlaw})$ (middle) and $\text{TBabs}^* (\text{apec}+\text{zxipcf}^*\text{diskbb+relxill})$ (bottom), respectively, together with the statistic produced.

continuum, it is encouraging that the models are able to isolate and characterize the shape of reflection even when slightly different continua are chosen. Nevertheless, due to the temporal proximity of the result of Jana et al. (2022) to the submission of our manuscript, we chose not to exclude this source from this sample.

3.3. MAXI J1727-203

MAXI J1727-203 was observed by NuSTAR once, in 2018 (ObsID 90401329002). We fit the entire 3–79 keV spectra from the observation. Fitting with $\text{TBabs}^* (\text{diskbb+powerlaw})$ produces $\chi^2/\nu = 567.22/451$, with the residuals indicating clear reflection features. The spectra and residuals of the fits are shown in Figure 4.

The two best-performing models are $\text{TBabs}^* (\text{diskbb+relxillCp})$ ($\chi^2/\nu = 438.87/442$, DIC = 688.31) and $\text{TBabs}^* (\text{diskbb+relxill})$ ($\chi^2/\nu = 440.59/442$, DIC = 473.09). As it performs much better in terms of DIC, we report the values measured from the MCMC run of the $\text{TBabs}^* (\text{diskbb+relxill})$ model. Through the MCMC analysis we find $a = 0.986_{-0.159}^{+0.012}$ and $\theta = 64_{-7}^{+10}$ degrees, and the full set of parameters is reported in Table 1.

3.4. Swift J1753.5-0127

There are five NuSTAR observations of Swift J1753.5-0127. Of those, only one shows clear signs of reflection: ObsID 80001047002. Therefore, we use the spectra extracted from the observation 80001047002 in the entire 3–79 keV band. Fitting the spectra with $\text{TBabs}^* (\text{diskbb+powerlaw})$ returns $\chi^2/\nu = 539.63/394$, with clear indications of relativistic reflection. All reflection models with no coronal geometric assumption perform similarly, while the “lamp-post” model appears to converge to a different, statistically disfavored solution. The best-performing reflection model, both in terms of χ^2 and DIC, is $\text{TBabs}^* (\text{diskbb+relxillCp})$, with $\chi^2/\nu = 385.18/385$. The posterior MCMC samples are nearly entirely concentrated at high spin values, measuring

$a = 0.997_{-0.003}^{+0.001}$ and $\theta = 74_{-3}^{+3}$ degrees. These measurements are consistent with the MCMC run of other models without assumptions about the coronal geometry. We show the spectra and residuals of the fits in Figure 5, and the modes of the posterior distribution for each parameter in the MCMC analysis together with their 1σ credible intervals are presented in Table 1.

The MCMC run of the “lamp-post” model provides similar inclination constraints, but a much worse spin constraint of $a = 0.4_{-0.8}^{+0.5}$. This model produces a fit worse by $\Delta\chi^2 = 18.7$ for two fewer free parameters. The `relxillCp` flavor is preferred over the `relxilllp` both in terms of AIC (15.86 vs. 30.76) and BIC (79.76 vs. 86.67). An F-test returns a probability of 10^{-4} , indicating that the non-“lamp-post” models are indeed a statistically significant improvement. Additionally, the `relxilllp` model performs worse than the `relxillCp` model by $\Delta\text{DIC} = 13.57$. Lastly, visually inspecting the residuals of the fit clearly shows that the Fe K line is not fit as well by the `relxilllp` when compared to the `relxillCp` model. Therefore, we report the results of our best-performing model ($\text{TBabs}^* (\text{diskbb+relxillCp})$): $a = 0.997_{-0.003}^{+0.001}$ and $\theta = 74_{-3}^{+3}$ degrees.

3.5. MAXI J0637-430

At the time of the analysis, there were eight NuSTAR observations of MAXI J0637-430, (ObsID 80502324002, 80502324004, 80502324006, 80502324008, 805023240010, 80502324012, 80502324014, and 80502324016). The first three (80502324002, 80502324004, and 80502324006) were taken during the soft state of the late 2019 outburst of the source and are the only ones that show clear reflection features. We fit the spectra from ObsID 80502324002 in the 3–50 keV energy band, from ObsID 80502324004 in the 3–60 keV energy band, and from ObsID 80502324006 in the 3–40 keV energy band, as the spectra are background-dominated at energies higher than the intervals mentioned. The unfolded spectra of the three observations are shown in the top panels of Figure 6, and the residuals of the fit to the $\text{TBabs}^* (\text{diskbb+relxillCp})$

Table 2
Results of the MCMC Analysis for V4641 Sgr and 4U 1543-47

ObsID	V4641 Sgr			4U 1543-47			
	80002012002	90102011002	90601302002	90702326006	90702326008	90702326010	90702326012
N_{H} [$\times 10^{22} \text{ cm}^{-2}$]	$3.3_{-2.1}^{+0.2}$	$4.9_{-1.1}^{+0.9}$	$3.8_{-0.9}^{+0.9}$	$1.8_{-0.3}^{+0.1}$	$0.07_{-0.07}^{+0.18}$	$1.3_{-0.3}^{+0.2}$	0_{-0}^{+0}
kT [keV]	$1.98_{-0.05}^{+0.10}$	$2.0_{-0.4}^{+0.1}$	$1.8_{-0.2}^{+0.1}$
A	$0.30_{-0.06}^{+0.09}$	$0.04_{-0.03}^{+0.02}$	$0.6_{-0.2}^{+0.2}$
z	$-4e - 02_{-9e-04}^{+2e-03}$	$-0.03_{-0.01}^{+0.01}$	$-0.033_{-0.002}^{+0.002}$
norm a, A	$0.74_{-0.24}^{+0.08}$	$0.5_{-0.1}^{+0.1}$	$0.9_{-0.2}^{+0.4}$
N_{H} [$\times 10^{22} \text{ cm}^{-2}$]	16_{-3}^{+7}	52_{-17}^{+20}	23_{-5}^{+6}	52_{-2}^{+12}	46_{-5}^{+4}	65_{-8}^{+9}	37_{-2}^{+2}
log(ξ)	$0.3_{-0.1}^{+0.6}$	$2.6_{-0.3}^{+0.2}$	$0.3_{-0.3}^{+0.3}$	$2.09_{-0.03}^{+0.12}$	$1.92_{-0.30}^{+0.06}$	$2.3_{-0.1}^{+0.1}$	$1.89_{-0.19}^{+0.08}$
f	$0.58_{-0.06}^{+0.12}$	$0.94_{-0.17}^{+0.06}$	$0.62_{-0.07}^{+0.05}$	$0.511_{-0.055}^{+0.007}$	$0.33_{-0.02}^{+0.02}$	$0.39_{-0.02}^{+0.02}$	$0.47_{-0.02}^{+0.01}$
kT _{in} [keV]	$1.16_{-0.02}^{+0.04}$	$1.39_{-0.13}^{+0.03}$	$1.19_{-0.04}^{+0.02}$	$0.807_{-0.004}^{+0.008}$	$0.864_{-0.004}^{+0.004}$	$0.817_{-0.006}^{+0.006}$	$0.813_{-0.004}^{+0.004}$
norm _{d,A}	22_{-3}^{+4}	$2.8_{-0.8}^{+1.0}$	55_{-10}^{+17}	$2e + 04_{-2e+03}^{+2e+03}$	$1e + 04_{-5e+02}^{+7e+02}$	$2e + 04_{-2e+03}^{+2e+03}$	$2e + 04_{-1e+03}^{+7e+02}$
q_1	$3.6_{-0.5}^{+0.7}$	$4.2_{-0.6}^{+1.1}$	$3.2_{-0.2}^{+2.2}$	$7.0_{-0.4}^{+0.9}$	$9.8_{-2.1}^{+0.2}$	$8.0_{-1.0}^{+0.4}$	8_{-1}^{+2}
q_2	$0.09_{-0.09}^{+0.37}$	$3e - 08_{-3e-08}^{+2e-07}$	$2e - 08_{-2e-08}^{+1e-07}$	$2e - 07_{-2e-07}^{+1e-06}$	$4e - 07_{-4e-07}^{+2e-06}$	$1e - 07_{-1e-07}^{+8e-07}$	$2e - 07_{-2e-07}^{+1e-06}$
R_{br} [r_g]	50_{-11}^{+16}	26_{-6}^{+21}	13_{-3}^{+9}	14_{-2}^{+3}	$29.3_{-7.5}^{+0.7}$	$10.3_{-0.3}^{+3.3}$	$29.5_{-6.2}^{+0.5}$
a	$0.66_{-0.09}^{+0.24}$	$0.98_{-0.32}^{+0.02}$	$0.7_{-0.8}^{+0.3}$	$0.97_{-0.02}^{+0.01}$	$0.90_{-0.48}^{+0.09}$	$0.978_{-0.034}^{+0.007}$	$0.95_{-0.32}^{+0.04}$
θ [$^{\circ}$]	$67.3_{-3.8}^{+0.3}$	65_{-2}^{+3}	54_{-27}^{+16}	$68.3_{-1.0}^{+0.6}$	65_{-2}^{+3}	69_{-1}^{+1}	61_{-1}^{+2}
R_{in} [r_{ISCO}]	$1.01_{-0.01}^{+0.13}$	$1.06_{-0.06}^{+0.70}$	$1.01_{-0.01}^{+0.17}$	$1.06_{-0.06}^{+0.59}$
Γ	$3.27_{-1.88}^{+0.04}$	$2.13_{-0.09}^{+0.17}$	$2.9_{-0.3}^{+0.2}$	$2.67_{-0.06}^{+0.03}$	$2.42_{-0.05}^{+0.05}$	$2.77_{-0.03}^{+0.03}$	$2.40_{-0.05}^{+0.07}$
log(ξ)	$4.66_{-1.37}^{+0.04}$	$3.4_{-0.3}^{+0.2}$	$4.62_{-0.37}^{+0.08}$	$2.3_{-0.1}^{+0.2}$	$2.3_{-0.4}^{+0.4}$	$2.3_{-0.2}^{+0.2}$	$1e - 06_{-1e-06}^{+7e-06}$
A_{Fe}	9_{-2}^{+1}	$3.6_{-0.6}^{+0.7}$	$9.8_{-2.5}^{+0.2}$	$9.93_{-0.75}^{+0.07}$	7_{-1}^{+3}	$9.9_{-1.3}^{+0.1}$	$9.1_{-1.6}^{+0.9}$
kT _e [keV]	$5.8_{-0.8}^{+59.8}$	35_{-12}^{+8}	$5.2_{-0.2}^{+1.5}$	87_{-13}^{+16}	114_{-21}^{+24}	$1e + 03_{-3e+02}^{+5e+01}$	109_{-22}^{+35}
R	$9.8_{-4.0}^{+0.2}$	9_{-2}^{+3}	8_{-3}^{+2}	$5.4_{-0.5}^{+0.5}$	$0.47_{-0.07}^{+0.17}$	$3.1_{-0.4}^{+0.4}$	$1.5_{-0.2}^{+0.2}$
norm _{r,A}	$6e - 05_{-3e-05}^{+3e-03}$	$5e - 05_{-6e-06}^{+2e-05}$	$1e - 03_{-6e-04}^{+1e-03}$	$0.013_{-0.001}^{+0.002}$	$0.029_{-0.003}^{+0.005}$	$0.032_{-0.003}^{+0.004}$	$0.010_{-0.002}^{+0.002}$
norm _{a,B}	$0.6_{-0.1}^{+0.2}$	$0.51_{-0.13}^{+0.08}$	$1.0_{-0.4}^{+0.3}$
norm _{d,B}	25_{-4}^{+3}	$2.8_{-0.6}^{+1.3}$	59_{-9}^{+19}	$2e + 04_{-2e+03}^{+2e+03}$	$1e + 04_{-5e+02}^{+7e+02}$	$2e + 04_{-2e+03}^{+2e+03}$	$2e + 04_{-1e+03}^{+7e+02}$
norm _{r,B}	$6e - 05_{-3e-05}^{+3e-03}$	$5e - 05_{-1e-05}^{+1e-05}$	$4e - 05_{-4e-05}^{+4e-04}$	$0.012_{-0.001}^{+0.002}$	$0.028_{-0.003}^{+0.005}$	$0.031_{-0.003}^{+0.004}$	$0.010_{-0.001}^{+0.002}$
χ^2/ν	$264_{-14}^{+19}(236.53)/141$	$180_{-6}^{+8}(163.83)/141$	$181_{-5}^{+9}(168.15)/94$	$503_{-7}^{+9}(505.76)/393$	$523_{-6}^{+6}(508.28)/418$	$502_{-9}^{+12}(520.25)/403$	$497_{-5}^{+6}(482.70)/399$

Note. In this table, we report the modes of the posterior distributions in the MCMC analysis, along with the 1σ credible intervals. For χ^2 , the number in parentheses indicates the best-fit χ^2 value. For the normalization of the components, the subscripts d (from diskbb), r (from relxill), and a (from apec) represent the model that the values correspond to, while the subscripts A and B represent which NuSTAR FMP detector from which the spectrum originated.

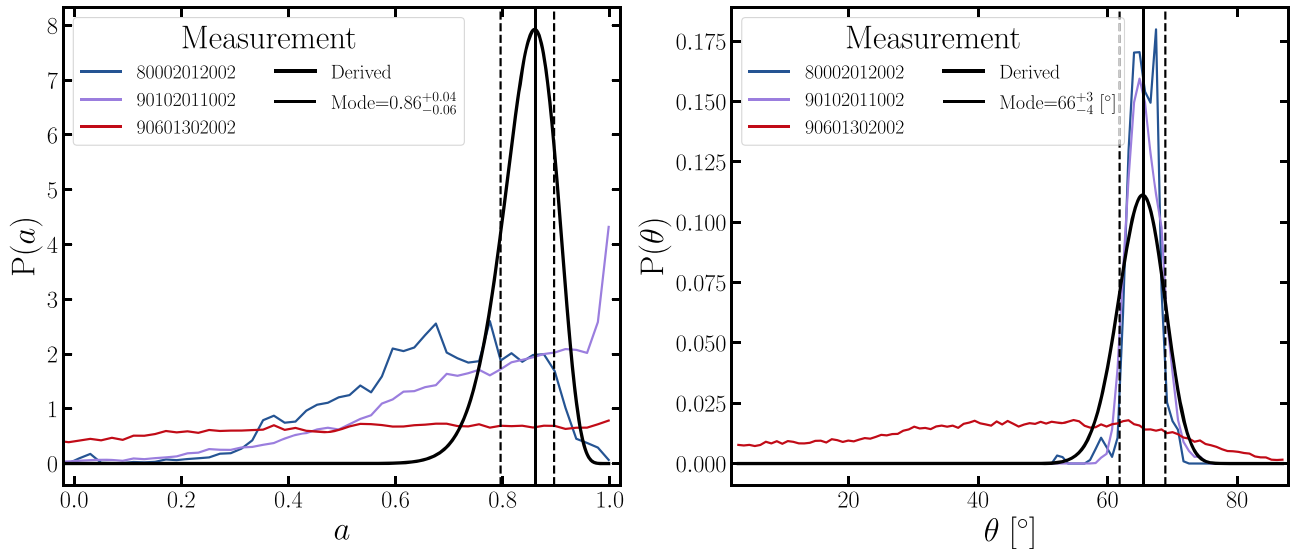


Figure 9. The left panel shows the posterior distributions resulting from the MCMC analysis of V4641 Sgr for spin, while the right panel shows the posterior distributions for the inclination of the inner accretion disk in the model. The different colored lines represent the three observations analysed, and the black curves represent the combined inferred distribution, with the transparency of the lines being proportional to the ratio of the reflected flux to the total flux in the 3–79 keV band, which were used as weighting when combining the posterior distributions. The solid vertical black lines represent the modes of the combined distribution, and the dashed vertical black lines represent the 1σ credible intervals of the measurements.

+powerlaw) model are shown in the middle panels of Figure 6, indicating signs of relativistic reflection.

When fitting the spectra with the models discussed in Section 2.1, the `relxill` and `relxillD` with $\log(n) = 19$ variants perform best in terms of χ^2 for all three observations. After running the MCMC analysis on the two mentioned models for all three observations, the `relxill` variant performs best in terms of DIC for ObsID 80502324004 and 80502324006, while the `relxillD` variant with $\log(n) = 19$ produces the better DIC for ObsID 80502324002. The residuals of the fits using these models are shown in the bottom panels of Figure 6, together with the fit statistic.

The modes of the posterior distributions for each parameter in the MCMC analysis, together with their 1σ credible intervals are shown in Table 1. Histograms of the posterior distributions of the spin and inner disk inclination from the MCMC analysis on the three observations are shown in Figure 7. Running the combining algorithm described in Section 2.3, we obtain the distributions shown through the black curves in Figure 7, with medians and credible intervals of $a = 0.97 \pm 0.02$ and $\theta = 62^{+3}_{-4}$ degrees.

3.6. V4641 Sgr

At the time of the analysis, four NuSTAR observations were public (ObsID 80002012002, 80002012004, 90102011002, and 90601302002). Using a mass of the BH of $M = 6.4 \pm 0.6 M_\odot$ and a distance to the system of $d = 6.2 \pm 0.7$ kpc (MacDonald et al. 2014), we calculate that only three of the four observations happened while the source had a luminosity within the Eddington range for which we expect the accretion disk to extend to the ISCO, with ObsID 80002012004 falling outside of that range. Therefore, we continue our analysis on the remaining three observations. We fit ObsID 80002012002 and 90102011002 in the 3–25 keV range and ObsID 90601302002 in the 3–20 keV range. The top panels in Figure 8 show the unfolded spectra from the three observations, and the middle panels show the residuals of the fit to the spectra

when using `TBabs * (diskbb+powerlaw)`. The fits are poor, and the models clearly require additional components.

Simply replacing the `powerlaw` component with the six variations of the `relxill` model that we test throughout our analysis improves the quality of the fit, but not significantly. The quality of the fit is drastically improved through the addition of an `apec` (Smith et al. 2001) component describing the emission from a collisionally ionized, diffuse gas in the vicinity of the source, which is characterized by the plasma temperature, metal abundance, redshift, and normalization. Additionally, we allow for the presence of ionized partial covering of the `diskbb` component through a `zxipcf` (Reeves et al. 2008) multiplicative component, which describes the effects of partially covering a fraction f of a source by a photoionized absorber. For all three observations, the addition of the two new components improves the quality of the fit significantly. The choice for the `relxill` component does not influence the quality of the fit, so we continue using the default `relxill` variant, making the complete model `TBabs * (apec+zxipcf*diskbb+relxill)`. The residuals of the fits are shown in the bottom panels of Figure 8, together with the fit statistic.

We ran the MCMC analysis starting from the best-fit solutions for each of the three observations. The modes of the posterior distributions for all the parameters in the MCMC runs, together with their 1σ credible intervals are presented in Table 2. Interestingly, in all three fits, the `apec` component requires a blueshift of $z \sim -0.03$, far above the terminal velocity of the companion wind. This could indicate the presence of a disk wind, which has been previously hinted at by Shaw et al. (2022). The quality of the fit becomes significantly worse when attempting to fix the redshift of the component to zero. While the Fe abundance A_{Fe} in the `relxill` component is generally high, the abundance of metals in the `apec` component is low, below unity.

Most importantly for this work, the spin of the compact object is generally high and the inclination is broadly consistent between the three observations. We combined the spin and

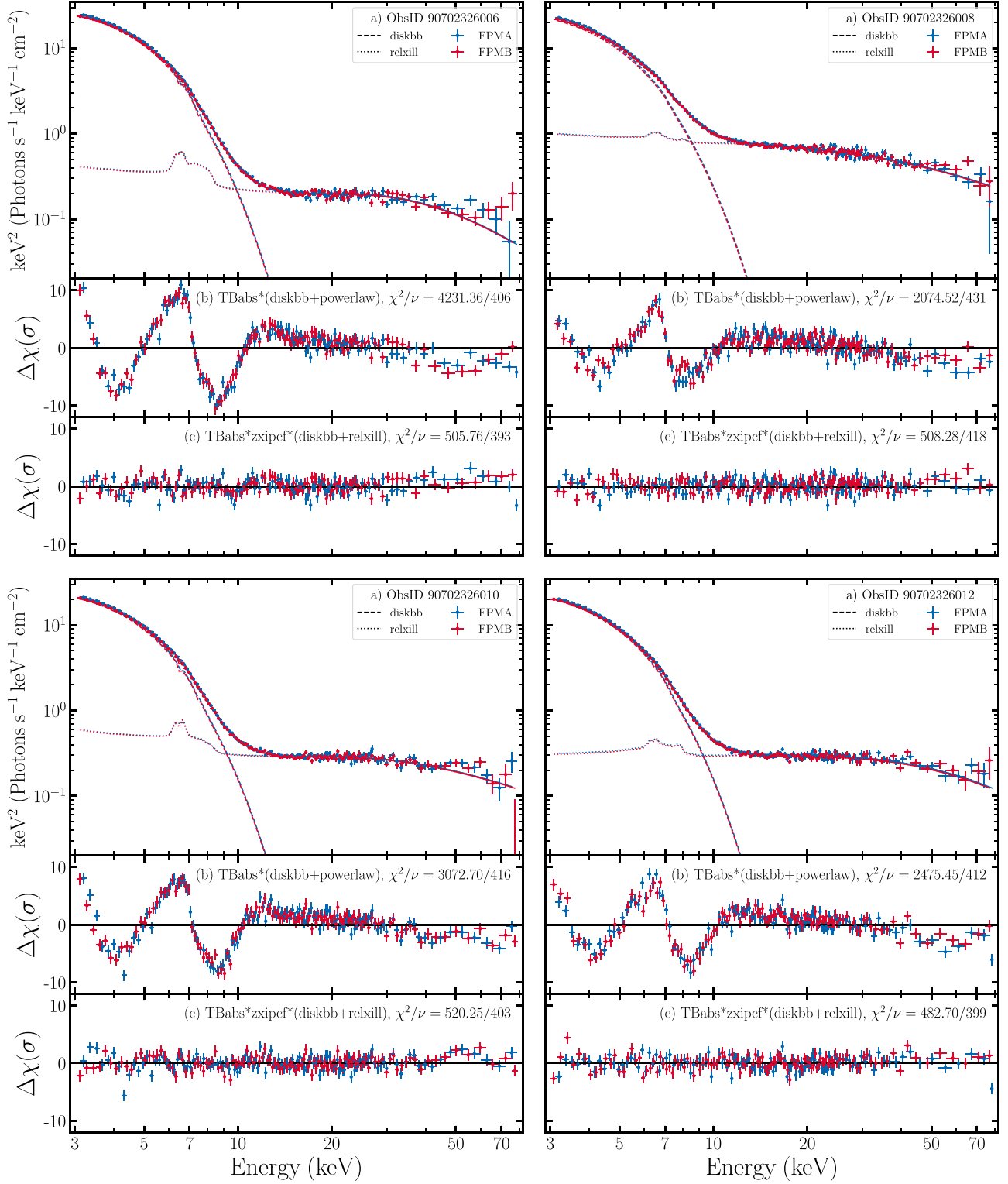


Figure 10. The four panels represent the four observations of 4U 1543-47 analysed. The top subpanels show the unfolded spectra, with the NuSTAR FPMA spectra shown in blue and FPMB spectra in red. The reported best-fit models are shown by the solid lines, while the contributions of the *relxill* component are shown by the dotted lines and the contributions of the *diskbb* component are shown through the dashed lines. The middle and bottom subpanels show the residuals in terms of σ produced when fitting the spectra with $\text{TBabs}^*(\text{diskbb+powerlaw})$ (middle) and $\text{TBabs}^*\text{zxipcf}^*(\text{diskbb+relxill})$ (bottom), respectively, together with the statistic produced.

inclination measurements from the three observations as described in Section 2.3. The results are shown in Figure 9. We measure $a = 0.86^{+0.04}_{-0.06}$ and $\theta = 66^{+3}_{-4}$ degrees.

Interestingly, in Figure 9, we can see that ObsID 90601302002 does not contribute strongly to the spin or inclination measurements, with both the spin and inclination

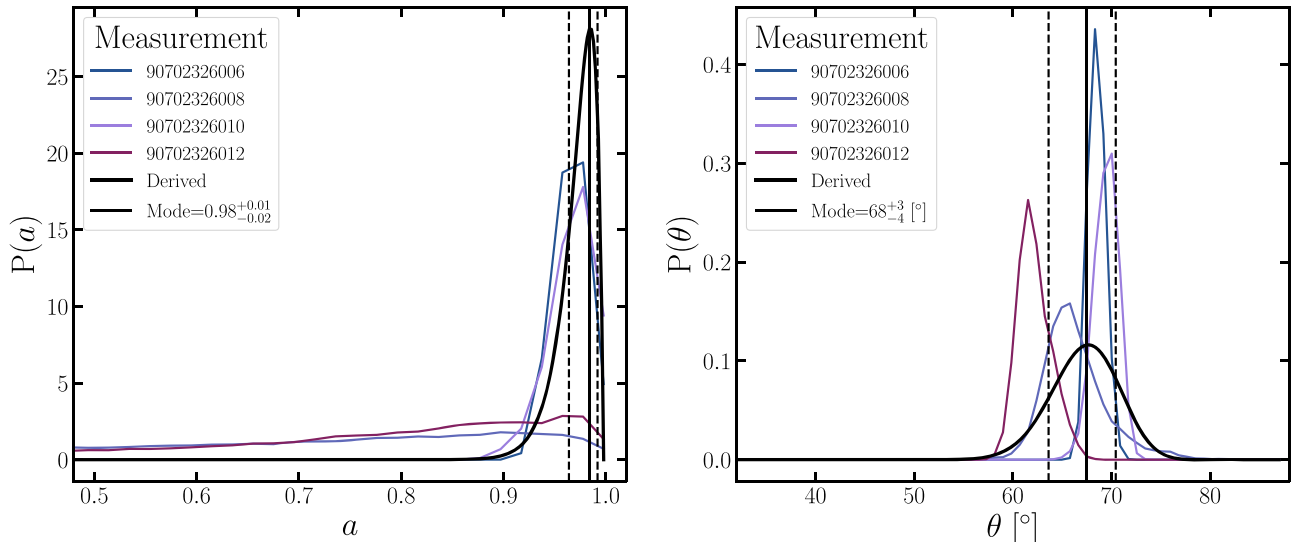


Figure 11. The left panel shows the posterior distributions resulting from the MCMC analysis of 4U 1543-47 for spin, while the right panel shows the posterior distributions for the inclination of the inner accretion disk in the model, with the transparency of the lines being proportional to the ratio of the reflected flux to the total flux in the 3–79 keV band, which were used as weighting when combining the posterior distributions. The different colored lines represent the four observations analysed, and the black curves represent the combined inferred distributions. The solid vertical black lines represent the modes of the combined distribution, and the dashed vertical black lines represent the 1σ credible intervals of the measurements.

being determined by the other two observations analysed. While for inclination, the two observations produce agreeing results, the spin measurement is the average of the two independent measurements. The uncertainty reported on the parameters is simply statistical, but the difference between the two posterior distributions that lead to the spin measurement of V4641 Sgr highlights the importance of understanding the magnitude of the systematic errors of spin measurements. A uniform treatment of the XB BH sample is crucial for this goal.

The inclination of the inner accretion disk in V4641 Sgr is well determined by our measurement, $\theta = 66^{+3}_{-4}$ degrees, in good agreement with the orbital inclination of the system (Orosz et al. 2001). Our measurement is incompatible with a low inclination, suggesting that V4641 Sgr cannot be a microblazar. However, Orosz et al. (2001) suggested that the jet angle must be $\lesssim 10^\circ$. Such a discrepancy between the inclination determined based on the jet angle and the inclination of the inner accretion disk was found by Draghis et al. (2021b) for XTE J1908+094, where it was suggested that the complexity of the local environment of the source together with an inability to correctly “phase” different approaching/receding ejections can alter our view of the inclinations determined based on the radio jet.

3.7. 4U 1543-47

At the time of the analysis, there were 10 public NuSTAR observations of 4U 1543-47 (ObsID 80702317002, 80702317004, 80702317006, 80702317008, 90702326002, 90702326004, 90702326006, 90702326008, 90702326010, and 90702326012), all taken during the 2021 outburst, with the source flux decreasing in each new observation. However, assuming a BH mass of $M = 9.4 \pm 2 M_\odot$ and a distance to the system of $d = 7.5 \pm 1$ kpc (Park et al. 2004), all 10 observations occur while the source is at an Eddington fraction larger than 0.3. Still, we analyse the last four observations taken (ObsID 90702326006, 90702326008, 90702326010, and 90702326012), as they happen while the source was at the lowest Eddington fraction of the 10 observations, and also had

the highest hardness of the 10 available observations. Within the allowed ranges of BH mass and distance to the system, the Eddington fraction during the last four observations varies between ~ 0.32 for the most favorable parameter combination for the last observation (ObsID 90702326012) and ~ 0.8 for the worst parameter combination for the first of the four observations analysed (ObsID 90702326006). It is important to note that the first of the 10 observations (ObsID 80702317002) gives an estimate between 2 and 5 for the Eddington fraction during the observation, suggesting that perhaps our mass and distance estimates are not accurate. As the source was outside of the Eddington ratio range for which we expect that the accretion disk extends to the ISCO, we allowed the inner disk radius r_{in} to vary during our spectral fitting. For all four observations we fit the spectra over the entire NuSTAR bandpass of 3–79 keV.

Figure 10 shows the unfolded spectra of the four observations in the top subpanels of each panel. The middle subpanels show the residuals and statistics produced when fitting the spectra with the simple TBabs * (diskbb+powerlaw) model, clearly indicating the presence of relativistic reflection. Similar to the case of V4641 Sgr presented in Section 3.6, simply replacing the powerlaw component with any of the six variations of the relxill family that we discussed in Section 2.1 does not lead to a good fit.

We started fitting the observation with the hardest spectrum (ObsID 90702326008). The initial fit using TBabs * (diskbb+powerlaw) returns $\chi^2/\nu = 2074.52/431$, while replacing the powerlaw component with relxill returns $\chi^2/\nu = 623.42/422$, showing additional broad residuals. To fit additional features, models are often expanded to include an additional xillver component that has the role of accounting for distant, unblurred reflection (see, e.g., Miller et al. 2018). In this case, the addition of a xillver component does not improve the quality of the fit, with the solution simply converging to the same parameter combination as before by fitting the reflection fraction of the xillver component to $R = 0$.

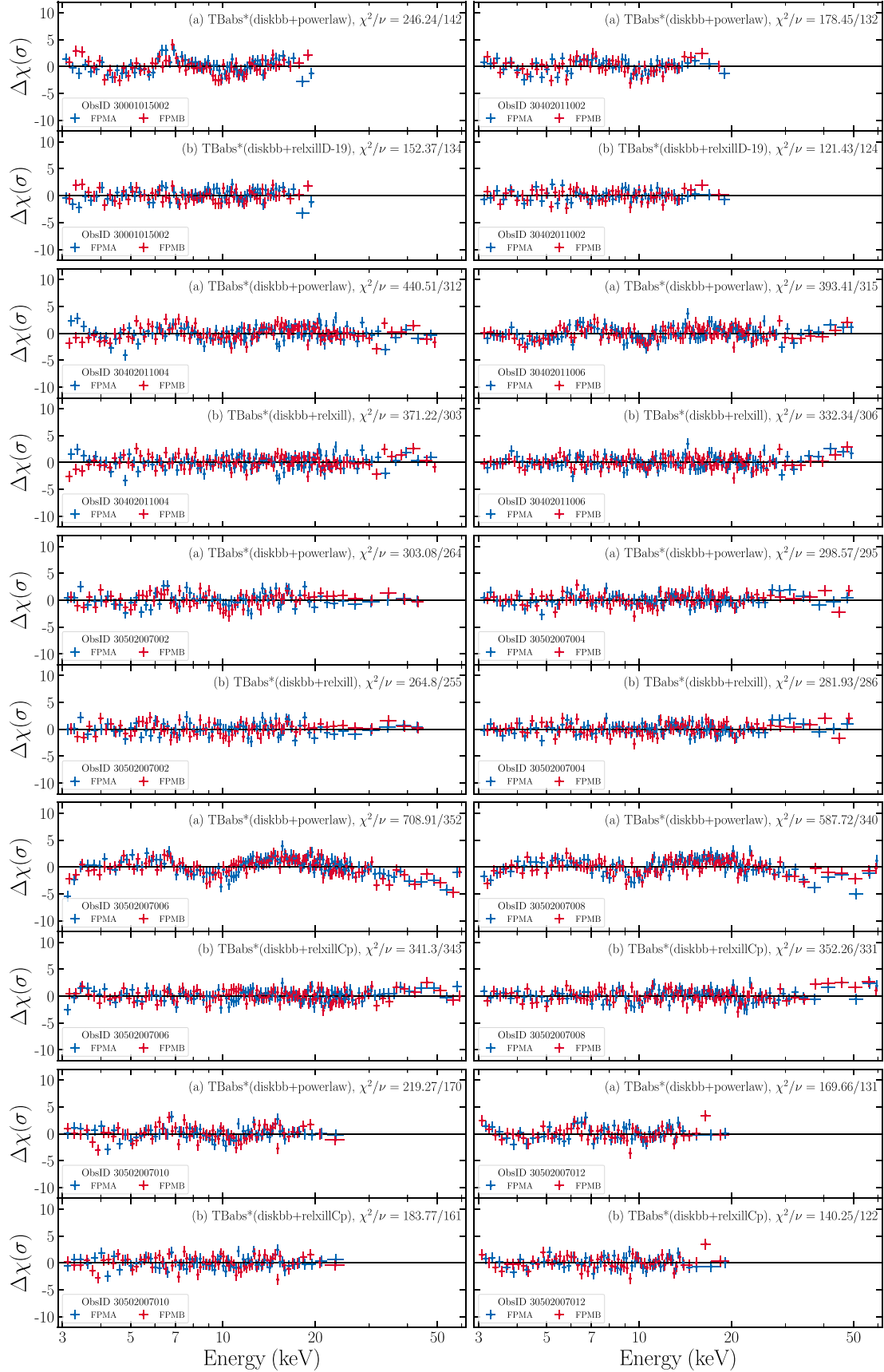


Figure 12. The 10 panels represent the 10 NuSTAR observations of 4U 1957+11 analysed. The top subpanels show the residuals in terms of σ produced when fitting the spectra with $\text{TBabs} * (\text{diskbb+powerlaw})$, and the bottom subpanels show the residuals when fitting with the best-performing reflection model. The blue and red points represent the FMPA and FPMB spectra from each observation, respectively. The subpanel titles show the model used to fit and the statistic produced, and the subpanel legends mention the ObsID number of the observation shown.

Table 3
Results of the MCMC Analysis for 4U 1957+11

ObsID	30001015002	30402011002	30402011004	30402011006	30502007002
Model	relxillD_19	relxillD_19	relxill	relxill	relxill
$N_{\text{H}} [\times 10^{22} \text{ cm}^{-2}]$	$0.96^{+0.02}_{-0.63}$	$0.97^{+0.03}_{-0.38}$	$0.5^{+0.2}_{-0.2}$	$0.8^{+0.1}_{-0.2}$	$0.9^{+0.1}_{-0.2}$
$kT_{\text{in}} [\text{keV}]$	$1.460^{+0.010}_{-0.007}$	$1.353^{+0.008}_{-0.017}$	$1.58^{+0.01}_{-0.01}$	$1.664^{+0.006}_{-0.009}$	$1.401^{+0.010}_{-0.008}$
norm _{d,A}	$10.0^{+0.4}_{-0.4}$	$10.6^{+0.6}_{-0.6}$	$7.2^{+0.3}_{-0.3}$	$9.4^{+0.3}_{-0.4}$	$12.1^{+0.2}_{-0.4}$
q_1	9^{+1}_{-3}	7^{+1}_{-2}	$9.6^{+0.4}_{-3.9}$	$3.3^{+4.0}_{-0.3}$	5^{+2}_{-1}
q_2	$0.4^{+1.2}_{-0.4}$	$0.09^{+0.58}_{-0.09}$	$5e - 07^{+3e-06}_{-5e-07}$	$2.4^{+0.6}_{-1.4}$	$6e - 06^{+3e-05}_{-6e-06}$
$R_{\text{br}} [r_g]$	12^{+16}_{-2}	$10.8^{+7.2}_{-0.8}$	97^{+3}_{-47}	9^{+51}_{-3}	22^{+22}_{-6}
a	$0.8^{+0.2}_{-0.5}$	$0.989^{+0.009}_{-0.060}$	$0.93^{+0.04}_{-0.17}$	$-0.8^{+1.0}_{-0.2}$	$0.2^{+0.4}_{-0.4}$
$\theta [^{\circ}]$	34^{+14}_{-6}	55^{+12}_{-12}	54^{+4}_{-6}	43^{+5}_{-5}	85^{+1}_{-7}
Γ	$3.10^{+0.05}_{-0.13}$	$3.27^{+0.07}_{-0.10}$	$2.49^{+0.05}_{-0.04}$	$2.56^{+0.07}_{-0.05}$	$2.6^{+0.1}_{-0.1}$
$\log(\xi)$	$4.67^{+0.03}_{-0.29}$	$4.67^{+0.03}_{-0.34}$	$4.5^{+0.2}_{-0.1}$	$4.6^{+0.1}_{-0.3}$	$0.6^{+0.9}_{-0.6}$
A_{Fe}	$3.1^{+2.2}_{-0.7}$	4^{+2}_{-2}	$0.54^{+0.35}_{-0.04}$	$0.7^{+0.5}_{-0.2}$	$3.7^{+5.1}_{-0.6}$
$kT_e [\text{keV}]$	106^{+49}_{-6}	163^{+206}_{-63}	119^{+368}_{-19}
R	$1.9^{+0.9}_{-0.9}$	3^{+1}_{-2}	$1.4^{+0.4}_{-0.4}$	$0.5^{+0.2}_{-0.2}$	3^{+2}_{-2}
norm _{r,A}	$4e - 04^{+2e-04}_{-1e-04}$	$6e - 04^{+2e-04}_{-2e-04}$	$2e - 03^{+4e-04}_{-3e-04}$	$3e - 03^{+6e-04}_{-6e-04}$	$2e - 03^{+12e-04}_{-6e-04}$
norm _{d,B}	$10.4^{+0.4}_{-0.6}$	$10.3^{+0.6}_{-0.6}$	$6.9^{+0.4}_{-0.2}$	$9.3^{+0.2}_{-0.4}$	$11.7^{+0.3}_{-0.4}$
norm _{r,B}	$5e - 04^{+2e-04}_{-2e-04}$	$5e - 04^{+2e-04}_{-2e-04}$	$2e - 03^{+4e-04}_{-3e-04}$	$3e - 03^{+6e-04}_{-5e-04}$	$1e - 03^{+3e-04}_{-5e-04}$
χ^2/ν	$161^{+6}_{-4}(152.37)/134$	$135^{+6}_{-6}(131.43)/124$	$379^{+5}_{-4}(371.22)/303$	$338^{+4}_{-5}(332.34)/306$	$274^{+6}_{-5}(264.80)/255$
ObsID	30502007004	30502007006	30502007008	30502007010	30502007012
Model	relxill	relxillCp	relxillCp	relxillCp	relxillCp
$N_{\text{H}} [\times 10^{22} \text{ cm}^{-2}]$	$0.8^{+0.1}_{-0.2}$	$1.9^{+0.1}_{-0.4}$	$0.99^{+0.01}_{-0.15}$	$0.5^{+0.2}_{-0.2}$	$0.03^{+0.26}_{-0.02}$
$kT_{\text{in}} [\text{keV}]$	$1.640^{+0.010}_{-0.006}$	$1.77^{+0.03}_{-0.02}$	$1.82^{+0.02}_{-0.01}$	$1.607^{+0.014}_{-0.007}$	$1.48^{+0.02}_{-0.04}$
norm _{d,A}	$10.7^{+0.3}_{-0.2}$	$4.4^{+0.4}_{-0.4}$	$5.6^{+0.3}_{-0.4}$	$11.1^{+0.2}_{-0.3}$	$9.8^{+0.5}_{-1.4}$
q_1	$3.3^{+3.0}_{-0.3}$	$6.2^{+2.9}_{-0.4}$	$3.3^{+4.0}_{-0.3}$	$3.2^{+2.7}_{-0.2}$	$3.2^{+1.3}_{-0.2}$
q_2	$0.2^{+1.3}_{-0.2}$	$3e - 07^{+2e-06}_{-3e-07}$	$1.9^{+1.1}_{-0.8}$	$2.1^{+0.3}_{-0.7}$	$0.3^{+0.6}_{-0.3}$
$R_{\text{br}} [r_g]$	10^{+32}_{-4}	18^{+18}_{-9}	9^{+37}_{-3}	8^{+15}_{-2}	20^{+29}_{-14}
a	$-0.4^{+0.6}_{-0.6}$	$0.97^{+0.02}_{-0.17}$	$-0.1^{+0.4}_{-0.9}$	$-0.8^{+0.8}_{-0.1}$	$0.3^{+0.3}_{-1.0}$
$\theta [^{\circ}]$	79^{+8}_{-28}	48^{+9}_{-8}	85^{+2}_{-47}	80^{+4}_{-13}	77^{+7}_{-12}
Γ	$2.67^{+0.06}_{-0.08}$	$2.38^{+0.05}_{-0.04}$	$2.28^{+0.03}_{-0.03}$	$2.6^{+0.2}_{-0.2}$	$1.9^{+0.4}_{-0.2}$
$\log(\xi)$	$4e - 06^{+3e-05}_{-4e-06}$	$4.68^{+0.02}_{-0.24}$	$0.2^{+2.5}_{-0.2}$	$3e - 06^{+2e-05}_{-3e-06}$	$0.3^{+1.5}_{-0.2}$
A_{Fe}	2^{+5}_{-2}	$0.52^{+0.18}_{-0.02}$	$0.8^{+5.5}_{-0.3}$	2^{+4}_{-1}	8^{+1}_{-3}
$kT_e [\text{keV}]$	123^{+230}_{-23}	18^{+6}_{-1}	$11.1^{+1.0}_{-0.8}$	$3.9^{+1.9}_{-0.9}$	$1.49^{+0.15}_{-0.09}$
R	$0.4^{+0.4}_{-0.2}$	$1.0^{+0.5}_{-0.3}$	$0.04^{+0.13}_{-0.04}$	7^{+4}_{-4}	3^{+5}_{-2}
norm _{r,A}	$4e - 03^{+8e-04}_{-8e-04}$	$4e - 03^{+1e-03}_{-8e-04}$	$6e - 03^{+2e-04}_{-6e-04}$	$1e - 03^{+8e-04}_{-4e-04}$	$7e - 04^{+3e-04}_{-3e-04}$
norm _{d,B}	$10.3^{+0.2}_{-0.3}$	$4.3^{+0.3}_{-0.5}$	$5.5^{+0.3}_{-0.4}$	$10.8^{+0.3}_{-0.2}$	$9.8^{+0.5}_{-1.4}$
norm _{r,B}	$4e - 03^{+8e-04}_{-7e-04}$	$4e - 03^{+9e-04}_{-1e-03}$	$5e - 03^{+3e-04}_{-6e-04}$	$9e - 04^{+8e-04}_{-3e-04}$	$7e - 04^{+3e-04}_{-3e-04}$
χ^2/ν	$293^{+5}_{-4}(281.93)/286$	$351^{+4}_{-5}(341.30)/343$	$360^{+5}_{-4}(352.26)/331$	$195^{+5}_{-4}(183.77)/161$	$149^{+5}_{-4}(140.25)/122$

Note. In this table, we report the modes of the posterior distributions in the MCMC analysis, along with the 1σ credible intervals. For χ^2 , the number in parentheses indicates the best-fit χ^2 value. For the normalization of the components, the subscripts d (from `diskbb`) and r (from `relxill`) represent the model that the values correspond to, while the subscripts A and B represent which NuSTAR FMP detector from which the spectrum originated.

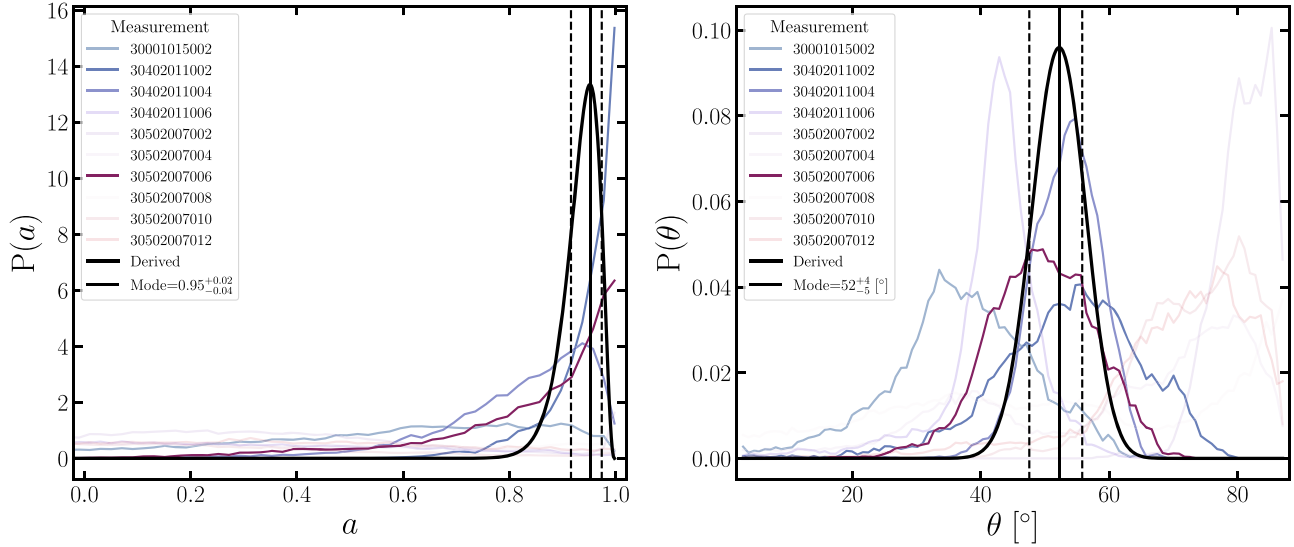


Figure 13. The left panel shows the posterior distributions resulting from the MCMC analysis of 4U 1957+11 for spin, while the right panel shows the posterior distributions for the inclination of the inner accretion disk in the model, with the transparency of the lines being proportional to the ratio of the reflected flux to the total flux in the 3–79 keV band, which were used as weighting when combining the posterior distributions. The different colored lines represent the different observations analysed, and the black curves represent the combined inferred distributions. The solid vertical black lines represent the modes of the combined distributions, and the dashed vertical black lines represent the 1σ credible intervals of the measurements.

Since the residuals indicate the presence of broad spectral features, we replaced the `xilliver` component with a second `relxill` component in the model, with the role of mimicking a torn accretion disk. To do that, we linked the BH spin between the two components, the Fe abundance, the power law indices Γ , the high-energy cutoff of the underlying power law continuum, and the normalization of the two components. The reflection fractions of the two components were allowed to vary, with the “inner” `relxill` component taking positive values for R , while the “outer” component taking only negative reflection fractions. Positive values of the reflection fraction in `relxill` components ensure that the model includes direct coronal emission, while negative reflection fraction values force the components to include only reflected emission. This way, the underlying continuum is included by the “inner” `relxill` component. We allowed the inner disk radius of the “inner” `relxill` component to vary, we set the outer disk radius of the “outer” `relxill` component to $r_{\text{out}} = 1000 r_g$, and linked the outer radius of the first `relxill` component to the inner radius of the second `relxill` component. The disk inclination in the two `relxill` components was allowed to vary. This model improves the quality of the fit, producing $\chi^2/\nu = 540.68/416$. The residuals of the fit clearly indicate a narrow absorption feature around 7.5 keV, and the measured inclination of the two `relxill` components is different, but not well constrained: the inner component measures $\theta \sim 3^\circ$ while the outer component measures $\theta \sim 85^\circ$. When accounting for the absorption feature using a gaussian additive component, and also linking the inclination in the two `relxill` components, the fit improves much further, producing $\chi^2/\nu = 501.13/416$. With the inclination of the two reflection components linked, the main difference between them is ionization, with the inner component taking large values $\log(\xi) \sim 4.6$, while the outer one measures $\log(\xi) \sim 0$.

An alternative treatment that can be used to test for variable ionization throughout the accretion disk is the `relxilllpion` model. We replaced the two reflection components in

our model with this new model, making the model `TBabs * (diskbb+relxilllpion)`. This also produces an improved fit when compared to the the simple `relxill` or `relxilllp` variants, returning $\chi^2/\nu = 523.85/424$. Lastly, similar to the case of V4641 Sgr, we tested the addition of ionized partial covering (through `zxipcf`) and re-emission (through `apec`). While the `apec` component did not improve the quality of the fits in this case, the addition of the `zxipcf` component to the default model improves the quality of the fit significantly ($\chi^2/\nu = 508.48/418$) for the model `TBabs * zxipcf * (diskbb+relxill)`. The absorber requires moderate ionization ($\log \xi \sim 2$) and covering fraction $f \sim 0.4$, consistent with a disk wind. The inner disk radius was allowed to vary, however the fit converges to a value of r_{in} consistent with the size of the ISCO.

We tested the three mentioned models on all four observations. In all four cases, the last model (including `zxipcf`) was preferred in terms of AIC and BIC, likely due to it producing a better statistic than the variable ionization model and having a smaller number of free parameters than the model with two reflection components. We mention that modifying the `relxill` variant in these models does not strongly affect the quality of the fit or the measured spin. Therefore we continue our analysis using the model `TBabs * zxipcf * (diskbb+relxill)`. The residuals produced by this model are shown in the bottom panels of Figure 10. We ran the MCMC analysis on these four observations with the given model. The modes and 1σ credible intervals for all parameters in the model are presented in Table 2 for each observation. The 1D posterior distributions of the spin and inclination parameters are shown in Figure 11. By combining the posterior distributions as explained in Section 2.3, we measure $a = 0.98^{+0.01}_{-0.02}$ and $\theta = 68^{+3}_{-4}$ degrees. Interestingly, this spin measurement disagrees with previous measurements, namely $a = 0.67^{+0.15}_{-0.08}$, measured through relativistic reflection on RXTE data (Dong et al. 2020) and $a = 0.80 \pm 0.05$, measured through continuum fitting (Shafee et al. 2006).

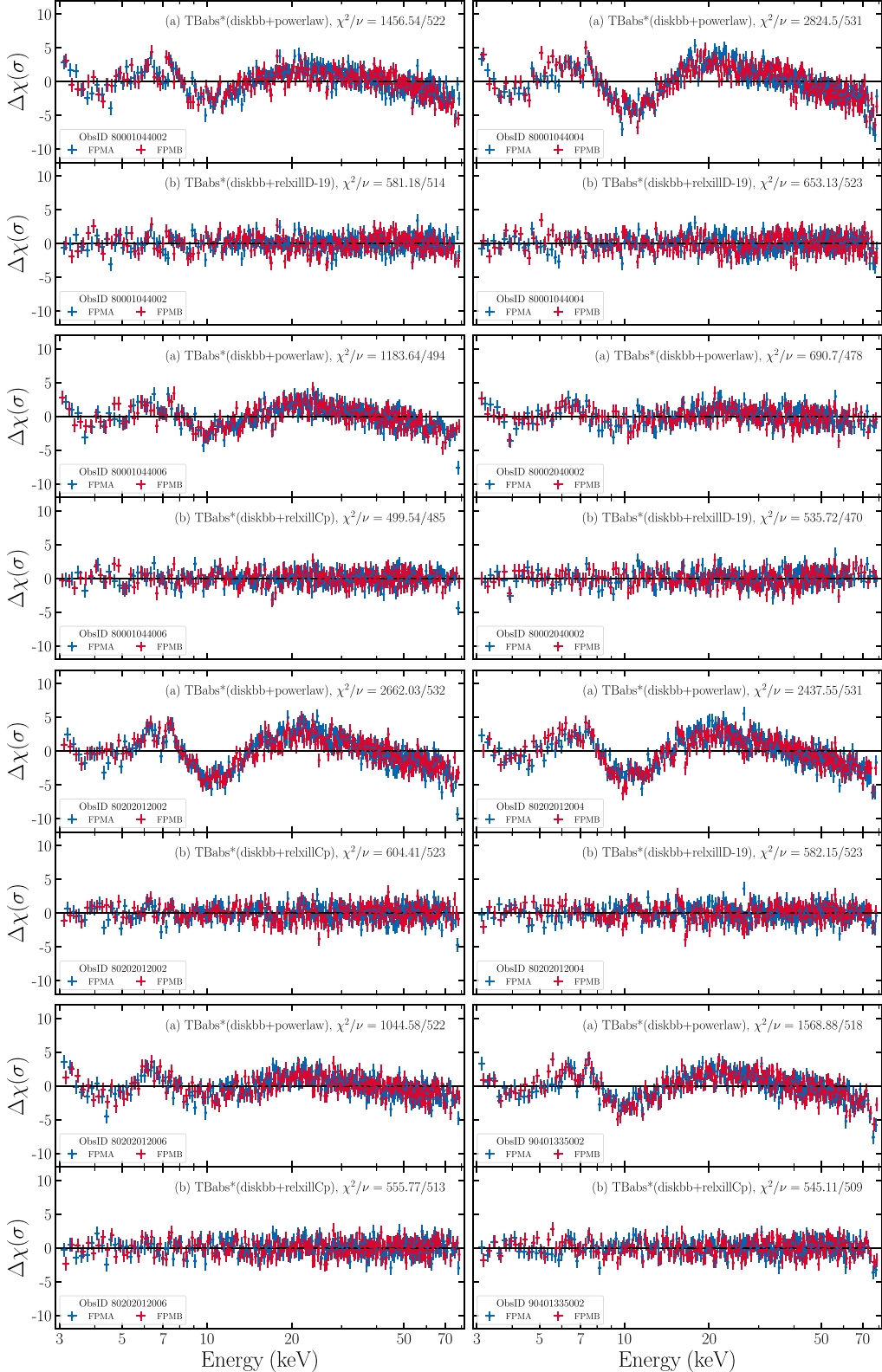


Figure 14. The eight panels represent the eight NuSTAR observations of H 1743-322 analysed. The top subpanels show the residuals in terms of σ produced when fitting the spectra with $\text{TBabs}^* \text{(diskbb+powerlaw)}$, and the bottom subpanels show the residuals when fitting with the best-performing reflection model. The blue and red points represent the FMPA and FPMB spectra from each observation, respectively. The subpanel titles show the model used to fit and the statistic produced, and the subpanel legends mention the ObsID number of the observation shown.

3.8. 4U 1957+11

Using NuSTAR data, Sharma et al. (2021) estimated the BH mass and distance to 4U 1957+11 to be $M = 5 \pm 1 M_{\odot}$ and

$d \sim 7$ kpc, respectively, and measured a spin of $a \sim 0.85$. Using Suzaku data, Nowak et al. (2012) estimated a BH spin of $a > 0.90$ for $M = 3 M_{\odot}$ and $d \sim 10$ kpc, and Maitra et al. (2014) measured a spin of $a > 0.98$. All measurements were performed

Table 4
Results of the MCMC Analysis for H 1732-322

ObsID	80001044002	80001044004	80001044006	80002040002	80202012002	80202012004	80202012006	90401335002
Model	relxillD_19	relxillD_19	relxillCp	relxillD_19	relxillCp	relxillD_19	relxillCp	relxillCp
N_{H} [$\times 10^{22}$ cm $^{-2}$]	$5.1^{+0.4}_{-0.9}$	$6.8^{+0.4}_{-0.5}$	$5.9^{+0.6}_{-1.0}$	$6.2^{+0.6}_{-2.0}$	$6.1^{+0.5}_{-0.3}$	$5.3^{+0.5}_{-0.5}$	$5.2^{+0.4}_{-0.6}$	$5.5^{+0.7}_{-0.6}$
kT_{in} [keV]	$0.55^{+0.02}_{-0.04}$	$0.504^{+0.009}_{-0.012}$	$0.50^{+0.02}_{-0.03}$	$0.47^{+0.09}_{-0.04}$	$0.527^{+0.010}_{-0.007}$	$0.525^{+0.008}_{-0.016}$	$0.53^{+0.01}_{-0.04}$	$0.53^{+0.02}_{-0.02}$
norm _{d,A}	327^{+212}_{-43}	$2e + 03^{+2e+02}_{-2e+02}$	915^{+264}_{-318}	247^{+629}_{-87}	$1e + 03^{+1e+02}_{-2e+02}$	$1e + 03^{+1e+02}_{-2e+02}$	355^{+119}_{-86}	634^{+112}_{-166}
q_1	$9.9^{+0.1}_{-2.0}$	$9.1^{+0.9}_{-2.3}$	$5.7^{+3.6}_{-0.3}$	$9.8^{+0.2}_{-2.9}$	5^{+2}_{-2}	$8.3^{+1.4}_{-0.9}$	9^{+1}_{-4}	$7.3^{+2.7}_{-0.6}$
q_2	$0.4^{+1.6}_{-0.4}$	$0.1^{+1.6}_{-0.1}$	$2.0^{+1.0}_{-0.9}$	$0.6^{+1.5}_{-0.3}$	$2.5^{+0.5}_{-1.2}$	$0.1^{+1.6}_{-0.1}$	$2.9^{+0.1}_{-1.6}$	$0.6^{+1.4}_{-0.5}$
R_{br} [r_g]	29^{+36}_{-19}	17^{+27}_{-11}	21^{+54}_{-4}	82^{+8}_{-48}	9^{+35}_{-3}	21^{+23}_{-14}	96^{+4}_{-53}	33^{+34}_{-23}
a	$0.992^{+0.006}_{-0.064}$	$0.984^{+0.008}_{-0.048}$	$0.9^{+0.1}_{-0.3}$	$0.996^{+0.002}_{-0.016}$	$0.8^{+0.1}_{-0.3}$	$0.987^{+0.005}_{-0.050}$	$0.992^{+0.006}_{-0.069}$	$0.99^{+0.01}_{-0.22}$
θ [°]	70^{+2}_{-20}	$54.8^{+12.8}_{-0.9}$	41^{+8}_{-4}	62^{+10}_{-7}	47^{+5}_{-3}	61^{+2}_{-8}	55^{+17}_{-6}	47^{+7}_{-6}
Γ	$1.36^{+0.02}_{-0.03}$	$1.45^{+0.01}_{-0.01}$	$1.49^{+0.02}_{-0.04}$	$1.43^{+0.03}_{-0.08}$	$1.65^{+0.02}_{-0.02}$	$1.59^{+0.03}_{-0.02}$	$1.54^{+0.03}_{-0.04}$	$1.53^{+0.03}_{-0.03}$
log(ξ)	$3.75^{+0.12}_{-0.05}$	$3.69^{+0.04}_{-0.06}$	$3.93^{+0.06}_{-0.07}$	$3.99^{+0.04}_{-0.67}$	$4.21^{+0.13}_{-0.03}$	$3.91^{+0.05}_{-0.12}$	$4.2^{+0.1}_{-0.4}$	$3.95^{+0.09}_{-0.13}$
A_{Fe}	$3.2^{+0.7}_{-0.5}$	$2.0^{+0.3}_{-0.2}$	$1.8^{+0.3}_{-0.3}$	$9.8^{+0.2}_{-3.7}$	$3.9^{+0.6}_{-0.8}$	$3.2^{+0.3}_{-0.8}$	$2.7^{+2.5}_{-0.5}$	$2.1^{+0.3}_{-0.4}$
kT_e [keV]	378^{+22}_{-146}	...	82^{+60}_{-16}	...	83^{+39}_{-35}	183^{+133}_{-58}
R	$0.5^{+0.5}_{-0.1}$	$1.0^{+0.5}_{-0.2}$	$1.2^{+0.2}_{-0.2}$	$0.20^{+0.18}_{-0.09}$	$1.2^{+0.4}_{-0.2}$	$1.3^{+0.4}_{-0.3}$	$0.27^{+0.39}_{-0.08}$	$1.3^{+0.4}_{-0.3}$
norm _{r,A}	$8e - 03^{+5e-04}_{-4e-04}$	$8e - 03^{+3e-04}_{-8e-04}$	$5e - 03^{+8e-04}_{-4e-04}$	$7e - 03^{+2e-04}_{-6e-04}$	$4e - 03^{+5e-04}_{-3e-04}$	$5e - 03^{+5e-04}_{-2e-04}$	$5e - 03^{+6e-04}_{-6e-04}$	$5e - 03^{+7e-04}_{-5e-04}$
norm _{d,B}	412^{+174}_{-98}	$2e + 03^{+2e+02}_{-2e+02}$	$1e + 03^{+2e+02}_{-4e+02}$	258^{+617}_{-107}	$1e + 03^{+1e+02}_{-2e+02}$	$1e + 03^{+2e+02}_{-2e+02}$	409^{+104}_{-115}	638^{+148}_{-133}
norm _{r,B}	$8e - 03^{+5e-04}_{-4e-04}$	$8e - 03^{+3e-04}_{-8e-04}$	$5e - 03^{+8e-04}_{-4e-04}$	$7e - 03^{+2e-04}_{-6e-04}$	$4e - 03^{+5e-04}_{-3e-04}$	$5e - 03^{+5e-04}_{-2e-04}$	$5e - 03^{+6e-04}_{-6e-04}$	$5e - 03^{+7e-04}_{-5e-04}$
χ^2/ν	$596^{+5}_{-6}(581.18)/514$	$668^{+6}_{-5}(653.13)/523$	$507^{+4}_{-5}(499.54)/485$	$542^{+10}_{-7}(535.72)/470$	$618^{+4}_{-4}(604.41)/523$	$595^{+6}_{-6}(582.15)/523$	$566^{+10}_{-5}(555.77)/513$	$557^{+5}_{-6}(545.11)/509$

In this table, we report the modes of the posterior distributions in the MCMC analysis, along with the 1σ credible intervals. For χ^2 , the number in parentheses indicates the best-fit χ^2 value. For the normalization of the components, the subscripts d (from `diskbb`) and r (from `relxill`) represent the model that the values correspond to, while the subscripts A and B represent which NuSTAR FMP detector from which the spectrum originated.

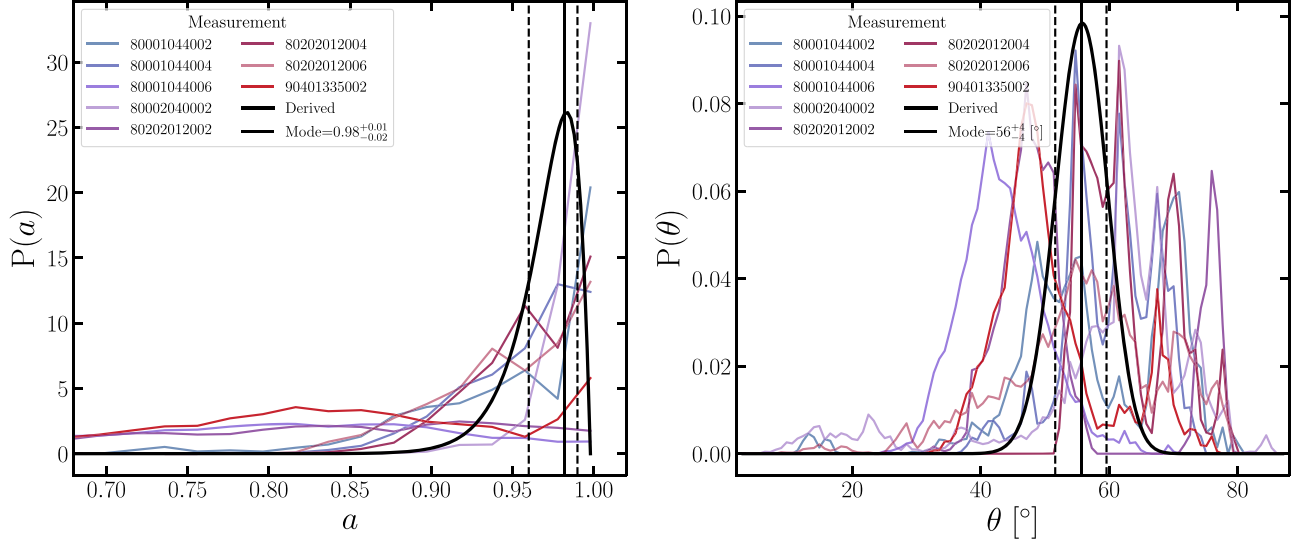


Figure 15. The left panel shows the posterior distributions resulting from the MCMC analysis of H 1743-322 for spin, while the right panel shows the posterior distributions for the inclination of the inner accretion disk in the model, with the transparency of the lines being proportional to the ratio of the reflected flux to the total flux in the 3–79 keV band, which were used as weighting when combining the posterior distributions. The different colored lines represent the different observations analysed, and the black curves represent the combined inferred distributions. The solid vertical black lines represent the modes of the combined distributions, and the dashed vertical black lines represent the 1σ credible intervals of the measurements.

using the continuum fitting method. 4U 1957+11 is a particularly interesting source, due to its relatively low mass estimates and large distance to the system, which makes this source consistently soft while at a relatively low Eddington fraction. Regardless of the choice of BH mass and distance to the system of the two combinations, all 10 existing NuSTAR observations were taken while the source was within the Eddington ratio limits for which we expect the accretion disk to extend to the ISCO. We fit all existing observations in the following energy bands: 30001015002 (3–20 keV), 30402011002 (3–20 keV), 30402011004 (3–50 keV), 30402011006 (3–50 keV), 30502007002 (3–45 keV), 30502007004 (3–50 keV), 30502007006 (3–60 keV), 30502007008 (3–60 keV), 30502007010 (3–25 keV), and 30502007012 (3–20 keV). The residuals when fitting the 10 spectra with TBabs * (diskbb+powerlaw) are shown in the top panels in Figure 12, along with the statistic. The spectra of 4U 1957+11 are generally dominated by disk emission and the reflection features are not always immediately obvious, but fitting with models that account for relativistic reflection always improves the quality of the fit.

Replacing the powerlaw component in our model with the six variants of `relxill` discussed in Section 2.1 produces better fits. We ran the MCMC analysis on the two best-performing models that account for reflection and selected the one that produced the best DIC. The residuals of the best-performing models in terms of DIC are shown in the bottom panels of Figure 12, and the modes and $\pm 1\sigma$ credible intervals of the posterior distributions for each parameter are presented in Table 3. The 1D posterior distributions for the spin and inclination are shown in Figure 13, with the transparency of the lines corresponding to each observation being proportional to the weights used when combining the measurements. We measure a spin of $a = 0.95^{+0.02}_{-0.04}$ and an inclination of $\theta = 52^{+4}_{-5}$ degrees. For this source in particular, it is extremely important to weight the posterior distributions from each individual measurement when combining them into a single measurement, and the combined spin and inclination values are dominated by the distributions inferred from the observations where reflection

was strongest. This spin measurement broadly agrees with the measurements made using continuum fitting, and it could be used to place better constraints on the mass of the BH and the distance to the system.

3.9. H 1743-322

There were 10 NuSTAR archival observations of H 1743-322 at the time of the analysis. However, the spectra from ObsID 80002040004 are well fit by TBabs * (diskbb+powerlaw) and the source is not detected in ObsID 80002040006. Using a BH mass of $M = 11.21^{+1.65}_{-1.96} M_{\odot}$ (Molla et al. 2017) and a distance to the system of $d = 8.5 \pm 0.8$ kpc (Steiner et al. 2012), all remaining eight observations (80001044002, 80001044004, 80001044006, 80002040002, 80202012002, 80202012004, 80202012006, and 90401335002) fall within the $10^{-3} \lesssim L_{\text{disk}}/L_{\text{Edd}} \lesssim 0.3$ Eddington fraction range. Therefore, we continue analysing the eight NuSTAR observations of H 1743-322, in the entire 3–79 keV NuSTAR band.

Using the TBabs * (diskbb+powerlaw) model to fit the spectra from the eight NuSTAR observations indicates the presence of relativistic reflection. The residuals of the fits are shown in the top panels of Figure 14, together with the fit statistic. We accounted for reflection through the six models discussed in Section 2.1, ran the MCMC analysis on the two best-performing models for each observation, and selected the best-performing model of the two (in terms of DIC) for each observation. The residuals of the fits using the best reflection model for each observation are shown in the bottom panels in Figure 14, together with the χ^2 statistic produced by the models. The modes and 1σ credible intervals of the posterior distributions for each parameter produced by the reflection models returning the best DIC for each observation are presented in Table 4, and the posterior distributions for the BH spin and inclination of the inner accretion disk are shown in Figure 15. Combining the spin and inclination measurements produced by each observation as described in Section 2.3 returns a spin of $a = 0.98^{+0.01}_{-0.02}$ and an inclination of $\theta = 56^\circ \pm 4^\circ$.

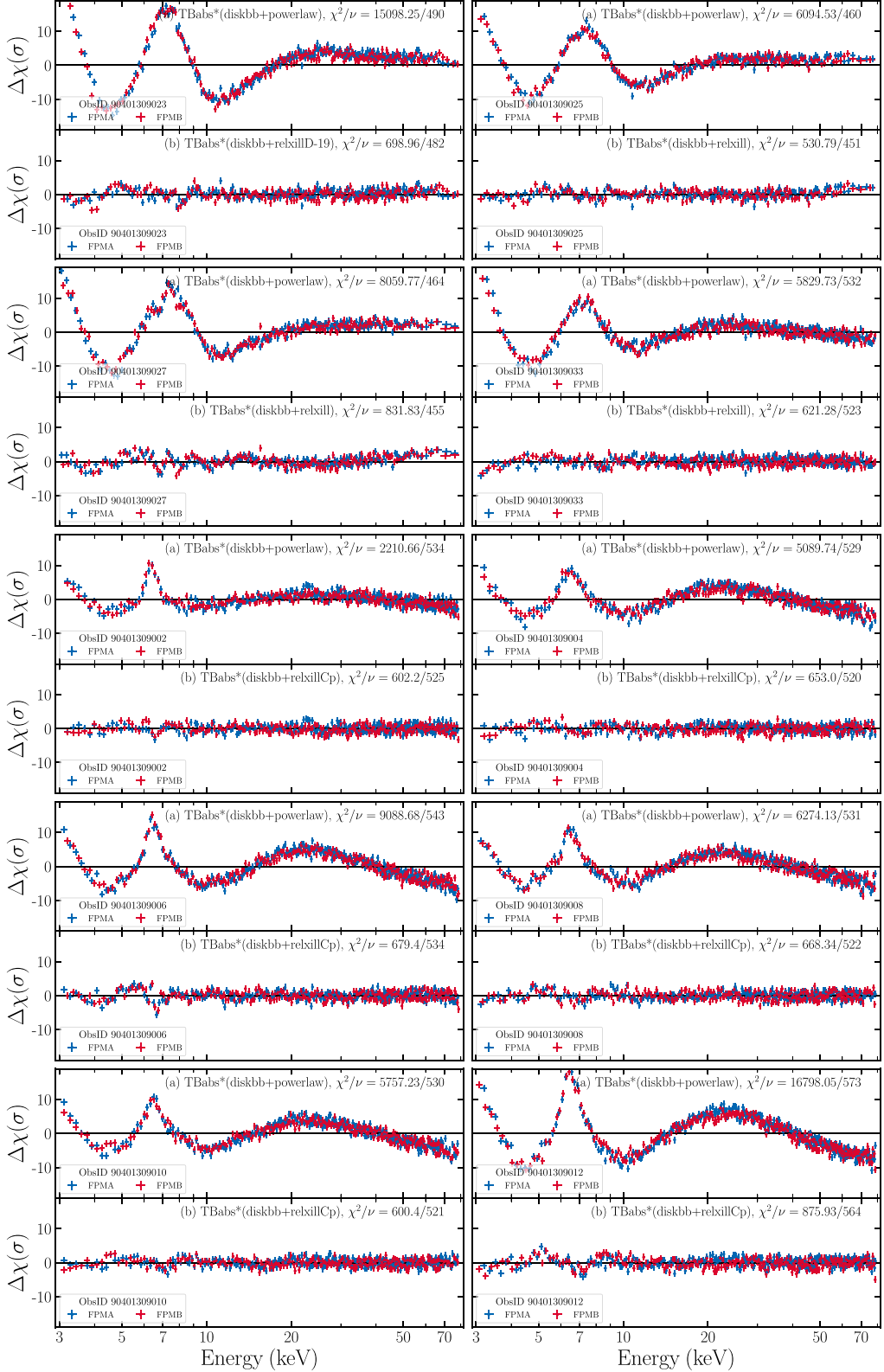


Figure 16. The 10 panels represent the first 10 NuSTAR observations of MAXI J1820+070 analysed. The top subpanels show the residuals in terms of σ produced when fitting the spectra with $\text{TBabs}^* (\text{diskbb+powerlaw})$, and the bottom subpanels show the residuals when fitting with the best-performing reflection model. The blue and red points represent the FPMA and FPMB spectra from each observation, respectively. The subpanel titles show the model used to fit and the statistic produced, and the subpanel legends mention the ObsID number of the observation shown.

Both the spin and inclination measurements of our analysis disagree with those determined by Steiner et al. (2012) through continuum fitting ($a = 0.2 \pm 0.3$) and from radio and X-ray jets

($\theta = 75 \pm 3$). While it is expected that the jet axis coincides with the BH spin axis and while that often is the case in observations (see, e.g., Cyg X-1; Krawczynski et al. 2022; or

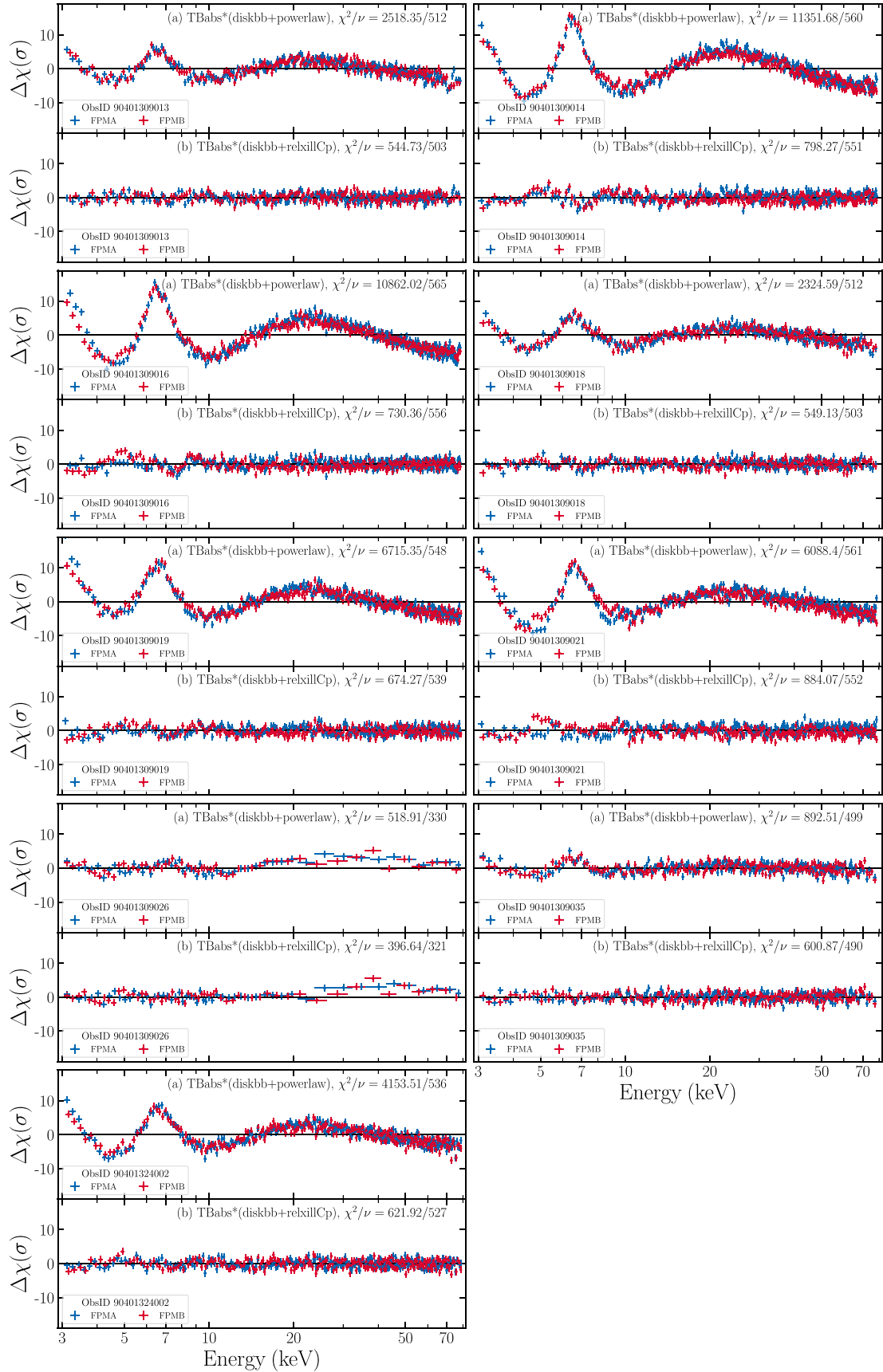


Figure 17. Continuation of Figure 16 for the remaining nine observations of MAXI J1820+070 analysed.

Table 5
Results of the MCMC Analysis for MAXI J1820+070

ObsID Model	90401309023 relxillD-19	90401309025 relxill	90401309027 relxill	90401309033 relxill	90401309002 relxillCp	90401309004 relxillCp	90401309006 relxillCp
$N_{\mathrm{H}} [\times 10^{22} \text{ cm}^{-2}]$	$0.058^{+0.085}_{-0.008}$	$0.053^{+0.029}_{-0.003}$	$5e - 02^{+7e-03}_{-7e-04}$	$0.07^{+0.31}_{-0.02}$	$0.07^{+0.15}_{-0.02}$	$0.07^{+0.20}_{-0.02}$	$0.053^{+0.025}_{-0.003}$
$kT_{\mathrm{in}} [\text{keV}]$	$0.760^{+0.004}_{-0.005}$	$0.762^{+0.001}_{-0.002}$	$7e - 01^{+7e-04}_{-8e-04}$	$0.56^{+0.01}_{-0.01}$	$0.73^{+0.11}_{-0.07}$	$0.88^{+0.05}_{-0.05}$	$1.47^{+0.06}_{-0.04}$
$\text{norm}_{\mathrm{d,A}}$	$1e + 04^{+4e+02}_{-4e+02}$	$1e + 04^{+2e+02}_{-2e+02}$	$1e + 04^{+8e+01}_{-9e+01}$	$2e + 03^{+3e+02}_{-3e+02}$	56^{+62}_{-33}	221^{+102}_{-67}	31^{+3}_{-6}
q_1	$8.7^{+0.5}_{-0.8}$	$9.98^{+0.02}_{-0.20}$	$9.99^{+0.01}_{-0.14}$	$9.6^{+0.3}_{-1.7}$	$9.9^{+0.1}_{-1.2}$	$9.8^{+0.2}_{-1.3}$	$3.09^{+0.82}_{-0.09}$
q_2	$0.08^{+0.64}_{-0.08}$	$0.1^{+1.1}_{-0.1}$	$2.6^{+0.4}_{-1.5}$	$2.1^{+0.9}_{-0.5}$	$1.0^{+0.4}_{-0.8}$	$2.9^{+0.1}_{-1.7}$	$1.77^{+0.03}_{-0.07}$
$R_{\mathrm{br}} [r_g]$	11^{+8}_{-1}	$10.8^{+0.1}_{-0.8}$	46^{+42}_{-8}	95^{+5}_{-34}	14^{+6}_{-2}	93^{+7}_{-41}	$10.3^{+2.4}_{-0.3}$
a	$0.993^{+0.001}_{-0.002}$	$0.990^{+0.001}_{-0.002}$	$0.989^{+0.001}_{-0.001}$	$0.978^{+0.007}_{-0.009}$	$0.4^{+0.1}_{-0.1}$	$0.88^{+0.03}_{-0.04}$	$0.5^{+0.1}_{-0.3}$
$\theta [\text{°}]$	72^{+1}_{-2}	$72.1^{+0.3}_{-0.8}$	$71.0^{+0.3}_{-0.5}$	69^{+2}_{-3}	39^{+2}_{-3}	55^{+2}_{-4}	$77.8^{+0.9}_{-6.3}$
Γ	$2.189^{+0.005}_{-0.009}$	$2.11^{+0.01}_{-0.01}$	$2.199^{+0.007}_{-0.009}$	$1.841^{+0.014}_{-0.008}$	$1.507^{+0.005}_{-0.003}$	$1.561^{+0.003}_{-0.003}$	$1.65^{+0.02}_{-0.01}$
$\log(\xi)$	$3.47^{+0.08}_{-0.07}$	$3.35^{+0.04}_{-0.03}$	$3.55^{+0.03}_{-0.03}$	$3.50^{+0.07}_{-0.08}$	$3.08^{+0.02}_{-0.02}$	$3.30^{+0.04}_{-0.04}$	$1.77^{+0.18}_{-0.08}$
A_{Fe}	$9.98^{+0.02}_{-0.19}$	$9.97^{+0.03}_{-0.18}$	$9.993^{+0.007}_{-0.062}$	$7.0^{+0.9}_{-1.1}$	7^{+1}_{-1}	$5.0^{+0.4}_{-0.2}$	$1.7^{+0.4}_{-0.2}$
$kT_e [\text{keV}]$...	$1e + 03^{+1e+01}_{-9e+01}$	$1e + 03^{+1e+01}_{-3e+01}$	$1e + 03^{+1e+01}_{-1e+02}$	45^{+5}_{-4}	$24.7^{+0.6}_{-0.6}$	37^{+4}_{-4}
R	$1.7^{+0.1}_{-0.2}$	$3.2^{+0.2}_{-0.2}$	$6.1^{+0.3}_{-0.3}$	$0.87^{+0.09}_{-0.14}$	$0.18^{+0.01}_{-0.02}$	$0.30^{+0.03}_{-0.03}$	$1.4^{+0.3}_{-0.5}$
$\text{norm}_{\mathrm{r,A}}$	$0.059^{+0.002}_{-0.003}$	$1e - 02^{+6e-04}_{-5e-04}$	$4e - 03^{+2e-04}_{-2e-04}$	$3e - 02^{+2e-04}_{-7e-04}$	$6e - 02^{+8e-04}_{-2e-03}$	$0.152^{+0.001}_{-0.001}$	$0.155^{+0.002}_{-0.001}$
$\text{norm}_{\mathrm{d,B}}$	$1e + 04^{+4e+02}_{-4e+02}$	$1e + 04^{+2e+02}_{-1e+02}$	$1e + 04^{+8e+01}_{-8e+01}$	$2e + 03^{+3e+02}_{-3e+02}$	57^{+68}_{-31}	247^{+108}_{-76}	29^{+5}_{-4}
$\text{norm}_{\mathrm{r,B}}$	$0.056^{+0.002}_{-0.003}$	$1e - 02^{+5e-04}_{-5e-04}$	$4e - 03^{+2e-04}_{-2e-04}$	$3e - 02^{+3e-04}_{-5e-04}$	$6e - 02^{+8e-04}_{-2e-03}$	$0.143^{+0.001}_{-0.001}$	$0.145^{+0.002}_{-0.001}$
χ^2/ν	$682^{+18}_{-4}(698.96)/482$	$547^{+6}_{-5}(530.79)/451$	$848^{+6}_{-5}(831.83)/455$	$633^{+4}_{-6}(621.28)/523$	$617^{+6}_{-5}(602.20)/525$	$661^{+6}_{-6}(653.00)/520$	$696^{+8}_{-6}(679.40)/534$
ObsID Model	90401309008 relxillCp	90401309010 relxillCp	90401309012 relxillCp	90401309013 relxillCp	90401309014 relxillCp	90401309016 relxillCp	
$N_{\mathrm{H}} [\times 10^{22} \text{ cm}^{-2}]$	$0.054^{+0.165}_{-0.004}$	$0.06^{+0.12}_{-0.01}$	$0.057^{+0.056}_{-0.007}$	$0.08^{+0.36}_{-0.03}$	$0.057^{+0.087}_{-0.007}$	$0.06^{+0.12}_{-0.01}$	
$kT_{\mathrm{in}} [\text{keV}]$	$0.84^{+0.01}_{-0.10}$	$0.83^{+0.04}_{-0.04}$	$0.86^{+0.02}_{-0.02}$	$0.77^{+0.06}_{-0.03}$	$0.80^{+0.03}_{-0.02}$	$0.83^{+0.02}_{-0.02}$	
$\text{norm}_{\mathrm{d,A}}$	381^{+342}_{-380}	391^{+136}_{-83}	327^{+41}_{-40}	551^{+278}_{-192}	510^{+115}_{-64}	382^{+82}_{-48}	
q_1	$9.9^{+0.1}_{-1.1}$	$9.93^{+0.07}_{-0.48}$	$9.98^{+0.02}_{-0.22}$	$8.6^{+0.9}_{-2.1}$	$9.96^{+0.04}_{-0.44}$	$9.97^{+0.03}_{-0.25}$	
q_2	$2.6^{+0.4}_{-1.5}$	$2.9^{+0.1}_{-1.6}$	$2.9^{+0.1}_{-1.6}$	$2.9^{+0.1}_{-1.8}$	$4e - 9^{+2e-03}_{-4e-09}$	$2.8^{+0.2}_{-1.6}$	
$R_{\mathrm{br}} [r_g]$	98^{+2}_{-46}	86^{+14}_{-29}	92^{+8}_{-31}	86^{+14}_{-43}	$10.6^{+6.6}_{-6}$	87^{+13}_{-28}	
a	$0.84^{+0.04}_{-0.06}$	$0.90^{+0.02}_{-0.02}$	$0.919^{+0.007}_{-0.010}$	$0.93^{+0.02}_{-0.06}$	$0.925^{+0.039}_{-0.009}$	$0.961^{+0.004}_{-0.004}$	
$\theta [\text{°}]$	52^{+3}_{-3}	57^{+1}_{-2}	$58.4^{+0.8}_{-1.0}$	57^{+4}_{-5}	59^{+4}_{-2}	$64.2^{+0.7}_{-0.8}$	
Γ	$1.574^{+0.002}_{-0.003}$	$1.571^{+0.002}_{-0.003}$	$1.578^{+0.002}_{-0.002}$	$1.597^{+0.005}_{-0.005}$	$1.596^{+0.005}_{-0.002}$	$1.630^{+0.003}_{-0.002}$	
$\log(\xi)$	$3.30^{+0.03}_{-0.03}$	$3.30^{+0.02}_{-0.04}$	$3.29^{+0.02}_{-0.03}$	$3.30^{+0.08}_{-0.05}$	$3.30^{+0.02}_{-0.07}$	$3.30^{+0.03}_{-0.02}$	
A_{Fe}	$5.0^{+0.5}_{-0.1}$	$5.7^{+0.7}_{-0.5}$	$6.5^{+0.4}_{-0.4}$	$5.8^{+1.4}_{-0.8}$	$6.4^{+0.9}_{-0.4}$	$7.4^{+0.6}_{-0.6}$	
$kT_e [\text{keV}]$	$24.0^{+0.4}_{-0.6}$	$23.1^{+0.5}_{-0.6}$	$25.9^{+0.4}_{-0.5}$	27^{+1}_{-1}	$27.0^{+0.9}_{-0.6}$	$30.8^{+0.9}_{-0.8}$	
R	$0.29^{+0.02}_{-0.03}$	$0.32^{+0.02}_{-0.03}$	$0.30^{+0.02}_{-0.01}$	$0.26^{+0.05}_{-0.02}$	$0.27^{+0.03}_{-0.02}$	$0.34^{+0.02}_{-0.01}$	
$\text{norm}_{\mathrm{r,A}}$	$2e - 01^{+1e-03}_{-7e-04}$	$2e - 01^{+9e-04}_{-1e-03}$	$1e - 01^{+6e-04}_{-5e-04}$	$0.142^{+0.002}_{-0.002}$	$1e - 01^{+1e-03}_{-5e-04}$	$1e - 01^{+7e-04}_{-6e-04}$	
$\text{norm}_{\mathrm{d,B}}$	348^{+311}_{-347}	384^{+125}_{-83}	307^{+38}_{-38}	538^{+238}_{-204}	454^{+108}_{-53}	342^{+70}_{-44}	
$\text{norm}_{\mathrm{r,B}}$	$1e - 01^{+1e-03}_{-5e-04}$	$1e - 01^{+1e-03}_{-8e-04}$	$1e - 01^{+6e-04}_{-4e-04}$	$0.133^{+0.001}_{-0.002}$	$1e - 01^{+8e-04}_{-6e-04}$	$1e - 01^{+6e-04}_{-6e-04}$	
χ^2/ν	$685^{+6}_{-8}(668.34)/522$	$615^{+6}_{-5}(600.40)/521$	$890^{+6}_{-5}(875.93)/564$	$546^{+7}_{-5}(544.73)/503$	$809^{+5}_{-7}(798.27)/551$	$737^{+6}_{-5}(730.36)/556$	
ObsID Model	90401309018 relxillCp	90401309019 relxillCp	90401309021 relxillCp	90401309026 relxillCp	90401309035 relxillCp	90401324002 relxillCp	
$N_{\mathrm{H}} [\times 10^{22} \text{ cm}^{-2}]$	$0.97^{+0.03}_{-0.34}$	$0.07^{+0.17}_{-0.02}$	$0.058^{+0.073}_{-0.008}$	$0.07^{+0.27}_{-0.02}$	$0.11^{+0.32}_{-0.06}$	$0.2^{+0.4}_{-0.2}$	
$kT_{\mathrm{in}} [\text{keV}]$	$0.74^{+0.03}_{-0.04}$	$0.79^{+0.03}_{-0.03}$	$0.83^{+0.03}_{-0.02}$	$0.750^{+0.006}_{-0.011}$	$0.65^{+0.07}_{-0.07}$	$0.73^{+0.04}_{-0.02}$	
$\text{norm}_{\mathrm{d,A}}$	910^{+326}_{-287}	533^{+91}_{-129}	224^{+34}_{-34}	$1e + 04^{+1e+03}_{-8e+02}$	68^{+63}_{-46}	649^{+377}_{-156}	
q_1	$9.92^{+0.08}_{-0.99}$	$8.3^{+0.9}_{-0.3}$	$9.4^{+0.6}_{-0.6}$	4^{+2}_{-1}	5^{+2}_{-1}	$9.94^{+0.06}_{-0.64}$	
q_2	$0.2^{+1.8}_{-0.2}$	$0.08^{+0.50}_{-0.08}$	$2.9^{+0.1}_{-1.5}$	$2.9^{+0.1}_{-1.7}$	$2.7^{+0.3}_{-1.4}$	$2.9^{+0.1}_{-1.6}$	
$R_{\mathrm{br}} [r_g]$	12^{+50}_{-2}	11^{+1}_{-1}	84^{+16}_{-26}	96^{+4}_{-52}	80^{+20}_{-33}	96^{+4}_{-38}	
a	$0.977^{+0.006}_{-0.005}$	$0.977^{+0.004}_{-0.009}$	$0.956^{+0.005}_{-0.012}$	$0.97^{+0.02}_{-0.14}$	$0.87^{+0.08}_{-0.14}$	$0.975^{+0.005}_{-0.005}$	
$\theta [\text{°}]$	67^{+1}_{-2}	$65.4^{+0.8}_{-1.6}$	63^{+1}_{-2}	54^{+7}_{-4}	49^{+8}_{-8}	67^{+1}_{-2}	
Γ	$1.652^{+0.006}_{-0.004}$	$1.647^{+0.003}_{-0.004}$	$1.616^{+0.004}_{-0.003}$	$1.94^{+0.08}_{-0.09}$	$1.649^{+0.006}_{-0.005}$	$1.653^{+0.006}_{-0.003}$	
$\log(\xi)$	$3.30^{+0.06}_{-0.06}$	$3.30^{+0.05}_{-0.03}$	$3.30^{+0.06}_{-0.03}$	$3.7^{+0.2}_{-0.4}$	$3.21^{+0.11}_{-0.08}$	$3.34^{+0.07}_{-0.05}$	

Table 5
(Continued)

ObsID Model	90401309018 relxillCp	90401309019 relxillCp	90401309021 relxillCp	90401309026 relxillCp	90401309035 relxillCp	90401324002 relxillCp
A_{Fe}	$9.8^{+0.2}_{-1.2}$	$8.2^{+0.9}_{-1.1}$	$9.0^{+0.9}_{-0.6}$	$9.2^{+0.7}_{-3.7}$	$9.6^{+0.3}_{-1.2}$	$8.8^{+0.8}_{-1.5}$
kT_e [keV]	32^{+3}_{-1}	33^{+2}_{-1}	40^{+2}_{-2}	9^{+2}_{-1}	131^{+57}_{-38}	37^{+3}_{-2}
R	$0.40^{+0.05}_{-0.05}$	$0.33^{+0.03}_{-0.02}$	$0.27^{+0.02}_{-0.02}$	3^{+1}_{-1}	$0.14^{+0.05}_{-0.02}$	$0.41^{+0.03}_{-0.04}$
norm _{r,A}	$0.105^{+0.001}_{-0.001}$	$1e - 01^{+8e-04}_{-1e-03}$	$7e - 02^{+7e-04}_{-5e-04}$	$0.003^{+0.001}_{-0.001}$	$2e - 02^{+4e-04}_{-8e-04}$	$0.102^{+0.001}_{-0.001}$
norm _{d,B}	874^{+314}_{-273}	473^{+69}_{-121}	232^{+28}_{-41}	$1e + 04^{+1e+03}_{-7e+02}$	55^{+55}_{-36}	604^{+300}_{-178}
norm _{r,B}	$0.100^{+0.001}_{-0.001}$	$1e - 01^{+7e-04}_{-1e-03}$	$7e - 02^{+6e-04}_{-6e-04}$	$3e - 03^{+1e-03}_{-9e-04}$	$2e - 02^{+3e-04}_{-9e-04}$	$1e - 01^{+1e-03}_{-9e-04}$
χ^2/ν	$558^{+7}_{-6}(549.13)/503$	$684^{+15}_{-5}(674.27)/539$	$893^{+6}_{-4}(884.07)/552$	$410^{+4}_{-7}(396.64)/321$	$613^{+6}_{-5}(600.87)/490$	$631^{+6}_{-4}(621.92)/527$

Note. In this table, we report the modes of the posterior distributions in the MCMC analysis, along with the 1σ credible intervals. For χ^2 , the number in parentheses indicates the best-fit χ^2 value. For the normalization of the components, the subscripts d (from `diskbb`) and r (from `relxill`) represent the model that the values correspond to, while the subscripts A and B represent which NuSTAR FMP detector from which the spectrum originated.

MAXI J1820+070 in Section 3.10), disparities between the inclination inferred through jet morphology and through relativistic reflection have previously been found (see, e.g., XTE J1908+094; Draghis et al. 2021b). Interestingly, Tursunov & Kološ (2018) estimated that the BH in H 1743-322 has a spin of $a = 0.4 \pm 0.2$ from quasiperiodic oscillations (QPOs). However, also from QPOs, Mondal (2010) find that the BH in H 1743-322 must have a spin of $a > 0.68$. It is important to note that there is no commonly accepted model to predict BH masses and spins based on QPOs, and models often disagree (Stefanov & Tasheva 2017). Furthermore, as QPO frequencies often shift, it is likely that they do not properly trace the BH ISCO.

3.10. MAXI J1820+070

NuSTAR observed MAXI J1820+070 27 times in 2018 and 2019. Using a BH mass of $M = 8.48 \pm 0.79 M_\odot$ (Torres et al. 2020) and a distance of $d = 2.96 \pm 0.33$ kpc (Atri et al. 2020), we find that 19 of the 27 observations happened while the source was at an Eddington fraction between $10^{-3} \lesssim L_{\text{disk}}/L_{\text{Edd}} \lesssim 0.3$: ObsID 90401309002, 90401309004, 90401309006, 90401309008, 90401309010, 90401309012, 90401309013, 90401309014, 90401309016, 90401309018, 90401309019, 90401309021, 90401309023, 90401309025, 90401309026, 90401309027, 90401309033, 90401309035, and 90401324002. We ran our analysis on these 19 observations, fitting in the entire 3–79 keV NuSTAR bandpass in each case. The residuals produced by fitting the spectra from each observation with the model `TBabs * (diskbb+power-law)`, and the fit statistic are shown in the top panels in Figures 16 and 17.

The residuals generally indicate the presence of relativistic reflection, so we fit the spectra from the 19 observations with the six models discussed in Section 2.1. Due to the large number of observations, we only ran the MCMC analysis on the best-performing model for each observation in terms of $\chi^2_r = \chi^2/\nu$, where ν represents the number of degrees of freedom in the model. The bottom panels in Figure 16 and continued in Figure 17 show the residuals of the best-performing reflection models. We ran the MCMC analysis on the fits to the spectra from the 19 observations. Table 5 shows the modes of the posterior distributions for each parameter in

the MCMC analysis for the 19 observations, along with the best-performing `relxill` variant that we used in our analysis. The posterior distributions for spin and inclination are shown in Figure 18. When combining the posterior distributions while weighting them by the ratio of the reflected to total flux in the 3–79 keV band, we obtain a spin of $a = 0.988^{+0.006}_{-0.028}$ and an inclination of $\theta = 64^{+3}_{-4}$ degrees.

Our inclination measurement is in good agreement with that determined by Atri et al. (2020) from the radio jet ($\theta = 63^\circ \pm 3^\circ$). However, our spin measurement disagrees with the values found using continuum fitting: $a = 0.14 \pm 0.09$ (Zhao et al. 2021) and $a = 0.2^{+0.2}_{-0.3}$ (Guan et al. 2021). The two continuum fitting measurements were obtained using Insight-HXMT spectra, which only extend to 2 keV at the low end of the bandpass. This could potentially inhibit properly distinguishing the disk emission from the high-energy component well enough for a spin measurement to be made using continuum fitting. In addition, the two papers do not model the effects of disk reflection in their analysis. At the same time, the spectral hardening factor parameter is often correlated with the spin parameter in models such as `kerrbb`, which are used for continuum fitting. Salvesen et al. (2013) showed that changes in the hardening factor used when modeling observations of GX 339-4 taken during multiple spectral states can explain features that mimic disk truncation. As the BH spin is linked to the size of the accretion disk ISCO, and in the assumption of an accretion disk extending all the way to the ISCO, using improperly high values of the spectral hardening factor could lead to continuum fitting spin measurements being biased toward low values. Moreover, Bhargava et al. (2021) used a relativistic precession model for QPO frequencies on NICER data to measure a spin of $a = 0.799^{+0.016}_{-0.015}$, and Prabhakar et al. (2022) analysed multiple Swift/XRT (Burrows et al. 2005), NICER (Gendreau et al. 2012), NuSTAR, and AstroSat (Agrawal 2006) observations and found that when fitting the reflection spectra, the spin was always high, so they fixed it at the maximum allowed value throughout their analysis. While Guan et al. (2021) argue that given their low spin measurement, the strong jet seen in MAXI J1820+070 must be powered by the accretion disk, our measurement allows for the jet to be powered by the high BH spin through the Blandford-Znajek mechanism (Blandford & Znajek 1977). This would be expected, especially given the good agreement

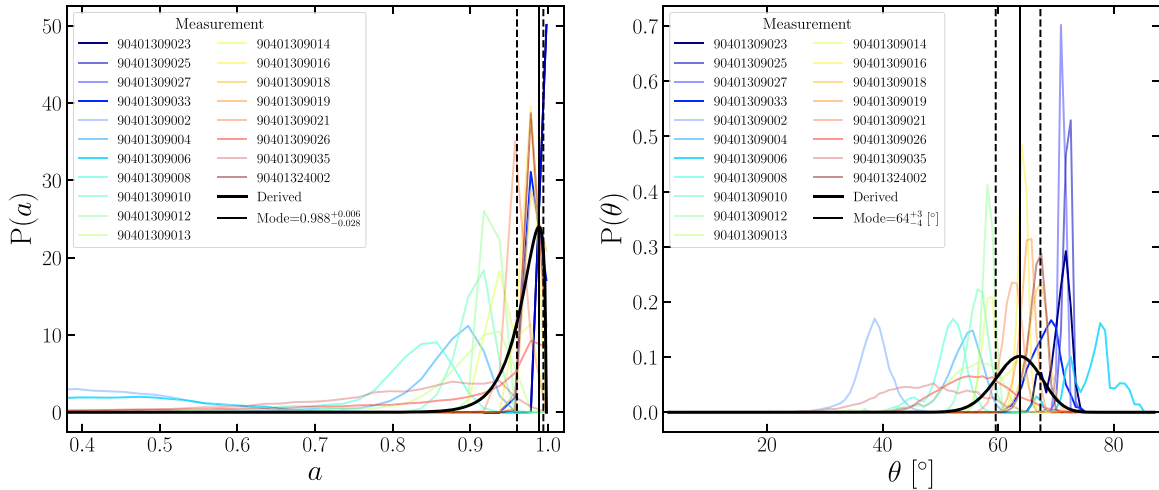


Figure 18. The left panel shows the posterior distributions resulting from the MCMC analysis of MAXI J1820+070 for spin, while the right panel shows the posterior distributions for the inclination of the inner accretion disk in the model, with the transparency of the lines being proportional to the ratio of the reflected flux to the total flux in the 3–79 keV band, which were used as weighting when combining the posterior distributions. The different colored lines represent the different observations analysed, and the black curves represent the combined inferred distributions. The solid vertical black lines represent the modes of the combined distributions, and the dashed vertical black lines represent the 1σ credible intervals of the measurements.

between the inclination of the BH spin axis measured from the relativistic reflection in this work and the inclination of the observed radio jet.

4. Spin Distribution

The new era of GW signals from BBH mergers holds tremendous promise. Currently, two challenges keep the full potential of BH mergers from being realized: (1) a degeneracy between the mass ratio in the binary and a combination of the spins of the BHs, and (2) a second degeneracy between the two spins themselves, which makes it difficult to measure individual spins (Pürrer et al. 2016). It was estimated that the degeneracies can be broken for S/Ns of 100, but only a few such observations are likely to occur every year (Pürrer et al. 2016). Moreover, even in this situation, the lowest-mass BH in the system can only be classified as having “high” or “low” spin, as opposed to an actual measurement. Given current event rates, the most pragmatic path forward is to obtain informative priors, based on a robust derivation of the spins of stellar-mass BHs in XB: the posterior distributions for GW spin measurements are correlated to the assumed prior distribution (Vitale et al. 2017; Abbott et al. 2019, 2021b), making it crucial to have educated predictions for the prior distributions.

We compiled all XB BH spin measurements in the literature obtained through continuum fitting and relativistic reflection in Table 6 and plotted them on the same scale in Figure 19, with the orange points showing measurements made through continuum fitting, yellow points representing relativistic reflection measurements made on data from instruments other than NuSTAR, blue points represent reflection measurements obtained using NuSTAR data, and the green points showing the 10 measurements of this paper.

A few interesting points can be made regarding the existing sample of BH spins in XB. First, it is worth noting that there are no precise negative BH spin measurements, only upper limit measurements suggesting $a \leq 0$. Of the seven measurements consistent with negative spins, five are made using continuum fitting and two are made using relativistic reflection, but not using NuSTAR data. Also, only four of the seven

measurements that allow negative spins exclusively require negative spins. A few of those constraints are particularly interesting. For GX 339–4, the continuum fitting method finds $a < 0.9$ (Kolehmainen & Done 2010), while relativistic reflection on NuSTAR data finds $a = 0.95^{+0.02}_{-0.08}$ (Parker et al. 2016). While the continuum fitting measurements nominally allow low and negative spins, simultaneously considering the two measurements made using the two methods indicates that the BH spin of GX339-4 is indeed high. Another particularly interesting source is IGR J17091-3624, for which continuum fitting measures $a < 0.2$ (Rao & Vadawale 2012), while relativistic reflection on NuSTAR data finds $a = 0.07 \pm 0.20$ (Wang et al. 2018). Again, while considering that only the continuum fitting measurement allows negative spins, treating the two measurements together indicates the BH is likely slowly rotating, with a spin consistent with zero.

Second, there appears to be a trend of decreasing measurement uncertainty with increasing BH spin. This trend applies both to spins obtained through the reflection method and through continuum fitting. As the size of the ISCO is set by the BH spin, a truncated disk around a rapidly spinning BH would produce similar spectral features as a disk that extends all the way to the ISCO around a slowly rotating BH (e.g., a maximally spinning BH with a disk truncated at $6r_g$ would produce similar features as a non-spinning BH with a disk that extends to the ISCO). However, since XB spin measurements assume inner disk radii consistent with the ISCO and since possible disk truncation would have the effect of biasing spin measurements to lower values, the high measured spins cannot be systematically mistaken and are likely accurate. The increased precision of high measured spins could be due to higher both direct and reflected emissivity with increased proximity to the BH, making the spectral features easier to observe and characterize, leading to smaller uncertainties on spin measurements. Works such as Bonson & Gallo (2016) and Kammoun et al. (2018) test the accuracy of spin measurements in active galactic nuclei (AGNs), finding that for values above 0.8, the spin is better constrained both in terms of accuracy and precision.

Table 6
All Current Spin Measurements in XBs Performed Through Relativistic Reflection or Continuum Fitting

Source	Spin reflection	Conf.	Telescope	Reference	Spin continuum	Conf.	Reference
IC 10 X-1	$0.85^{+0.04}_{-0.07}$	90	Steiner et al. (2016)
M31 ULX-1	$0.36^{+0.10}_{-0.11}$	90	Middleton et al. (2012)
M31 ULX-2	<-0.17	97	Middleton et al. (2014)
M33 X-7	$0.84^{+0.05}_{-0.05}$	68	Liu et al. (2008)
AT 2019wey	$0.97^{+0.02}_{-0.03}$	68	NuSTAR	Feng et al. (2022a)
LMC X-3	$0.24^{+0.05}_{-0.05}$	90	NuSTAR	Jana et al. (2021b)	$0.25^{+0.2}_{-0.29}$	90	Steiner et al. (2014)
LMC X-1	$0.9395^{+0.015}_{-0.015}$	90	NuSTAR	Jana et al. (2021b)	$0.92^{+0.05}_{-0.07}$	68	Gou et al. (2009)
1A 0620-00	$0.12^{+0.19}_{-0.19}$	68	Gou et al. (2010)
MAXI J0637-430	$0.97^{+0.02}_{-0.02}$	68	NuSTAR	this paper
GS 1124-683	$0.63^{+0.16}_{-0.19}$	68	Chen et al. (2016)
MAXI J1348-630	$0.78^{+0.04}_{-0.04}$	90	NuSTAR	Jia et al. (2022)
GS 1354-645	>0.98	68	NuSTAR	El-Batal et al. (2016)
MAXI J1535-571	$0.985^{+0.002}_{-0.004}$	90	NuSTAR	Dong et al. (2022)
4U 1543-47	$0.98^{+0.01}_{-0.02}$	68	NuSTAR	this paper	$0.8^{+0.05}_{-0.05}$	90	Shafee et al. (2006)
XTE J1550-564	$0.55^{+0.15}_{-0.22}$	90	ASCA & RXTE	Steiner et al. (2011)	$0.34^{+0.37}_{-0.45}$	90	Steiner et al. 2011
MAXI J1631-479	>0.94	90	NuSTAR	Xu et al. (2020b)
4U 1630-472	$0.985^{+0.005}_{-0.014}$	68	NuSTAR	King et al. (2014)	$0.92^{+0.04}_{-0.04}$	99.7	Pahari et al. (2018)
XTE J1650-500	$0.79^{+0.01}_{-0.01}$	68	XMM	Miller et al. (2009)
XTE J1652-453	$0.45^{+0.02}_{-0.02}$	90	XMM	Hiemstra et al. (2011)
GRO J1655-40	$0.98^{+0.01}_{-0.01}$	68	RXTE	Miller et al. (2009)	$0.7^{+0.05}_{-0.05}$	90	Shafee et al. (2006)
Swift J1658.2-4242	>0.96	90	NuSTAR	Xu et al. (2018)
MAXI J1659-152	<0	95	XMM & RXTE	Rout et al. (2020)	<0.44	90	Feng et al. (2022b)
GX 339-4	$0.95^{+0.02}_{-0.08}$	68	NuSTAR	Parker et al. (2016)	<0.9	90	Kolehmainen & Done (2010)
IGR J17091-3624	$0.07^{+0.2}_{-0.2}$	90	NuSTAR	Wang et al. (2018)	<0.2	90	Rao & Vadawale (2012)
SAX J1711.6-3808	$0.6^{+0.2}_{-0.2}$	68	BeppoSAX	Miller et al. (2009)
GRS 1716-249	>0.92	90	NuSTAR	Tao et al. (2019)
MAXI J1727-203	$0.986^{+0.012}_{-0.159}$	68	NuSTAR	this paper
Swift J1728.9-3613	$0.86^{+0.02}_{-0.02}$	68	NuSTAR	Draghis et al. (2023)
GRS 1739-278	$0.8^{+0.2}_{-0.2}$	90	NuSTAR	Miller et al. (2015)
1E 1740.7-2942	>0.5	68	NuSTAR	Stecchini et al. (2020)
IGR J17454-2919	$0.971^{+0.027}_{-0.171}$	68	NuSTAR	this paper
Swift J174540.2-290037	$0.92^{+0.05}_{-0.07}$	90	NuSTAR	Mori et al. (2019)
Swift J174540.7-290015	$0.94^{+0.03}_{-0.1}$	90	NuSTAR	Mori et al. (2019)
H 1743-322	$0.98^{+0.01}_{-0.02}$	68	NuSTAR	this paper	$0.2^{+0.3}_{-0.3}$	68	Steiner et al. (2012)
XTE J1752-223	$0.92^{+0.06}_{-0.06}$	68	RXTE	García et al. (2018)
Swift J1753.5-0127	$0.997^{+0.01}_{-0.002}$	68	NuSTAR	this paper
GRS 1758-258	$0.991^{+0.007}_{-0.019}$	68 (90)	NuSTAR	this paper (Jana et al. 2022)
($a > 0.92$)							
MAXI J1803-298	$0.991^{+0.001}_{-0.001}$	68	NuSTAR	Feng et al. (2022c)
MAXI J1813-095	>0.76	90	NuSTAR	Jana et al. (2021a)
V4641 Sgr	$0.86^{+0.02}_{-0.02}$	68	NuSTAR	this paper
MAXI J1820+070	$0.988^{+0.006}_{-0.028}$	68	NuSTAR	this paper	$0.14^{+0.09}_{-0.09}$	68	Zhao et al. (2021)
MAXI J1836-194	$0.88^{+0.03}_{-0.03}$	90	Suzaku	Reis et al. (2012)
MAXI J1848-015	$0.967^{+0.013}_{-0.013}$	90	NuSTAR	Pike et al. (2022)
EXO 1846-031	$0.997^{+0.001}_{-0.002}$	68	NuSTAR	Draghis et al. (2020b)
XTE J1908+094	$0.55^{+0.29}_{-0.45}$	68	NuSTAR	Draghis et al. (2021b)
Swift J1910.2-0546	<-0.32	90	XMM	Reis et al. (2013)
GRS 1915+105	$0.98^{+0.01}_{-0.01}$	68	NuSTAR	Miller et al. (2013)	$0.995^{+0.002}_{-0.005}$	90	Sreehari et al. (2020)
Cyg X-1	>0.97	68	NuSTAR	Parker et al. (2015)	>0.983	99.7	Gou et al. (2014)
4U 1957+11	$0.95^{+0.02}_{-0.04}$	68	NuSTAR	this paper	>0.9	90	Nowak et al. (2012)
V404 Cyg	>0.92	99	NuSTAR	Walton et al. (2017)

Note. Columns named “Conf.” show the confidence limit of the quoted measurement, in percentages.

Third, it seems like the overall distribution of spin measurements is concentrated around high values. Using the same method that we used to combine multiple measurements

into a single distribution, we combined the multiple independent spin measurements in Table 6 and Figure 19 in an attempt to understand the entire *observed* BH spin distribution in XBs.

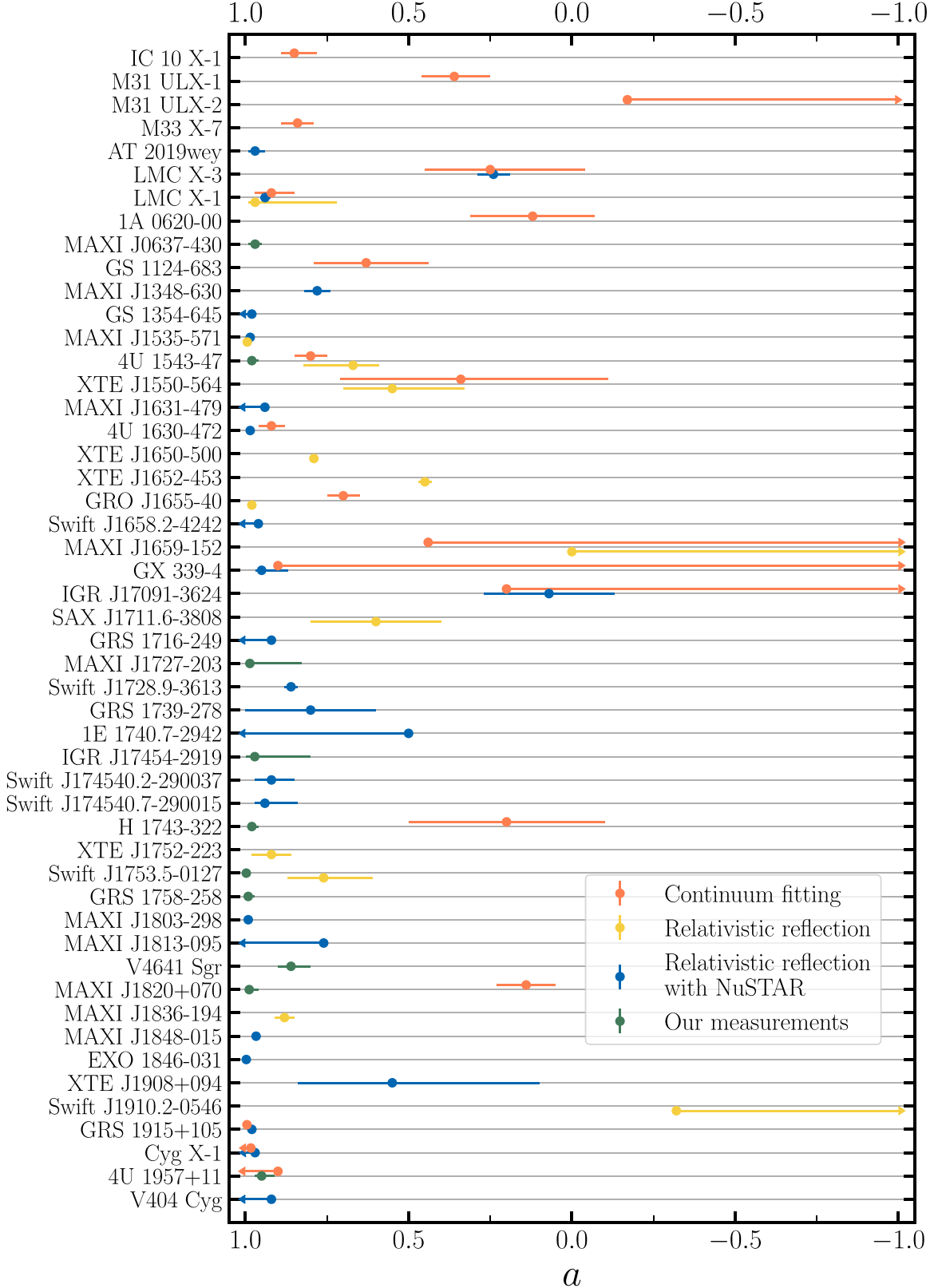


Figure 19. All current measurements of BH spins in XB, obtained through continuum fitting (orange) or relativistic reflection. Spin measurements obtained through relativistic reflection using measurements from NuSTAR are indicated in blue, while reflection measurements using data from other instruments are shown in yellow. The new measurements of this paper are shown in green. The sources are ordered in increasing R.A., and the values and references for all measurements are presented in Table 6. The arrows indicate upper or lower limits.

It is crucial to acknowledge that this distribution is likely influenced by observational and selection biases, which can be better understood through a uniform treatment of the entire spin

sample. Additionally, it is important to note that the measurements in the literature vary widely in terms of the energy range and resolution of the instrument used and of

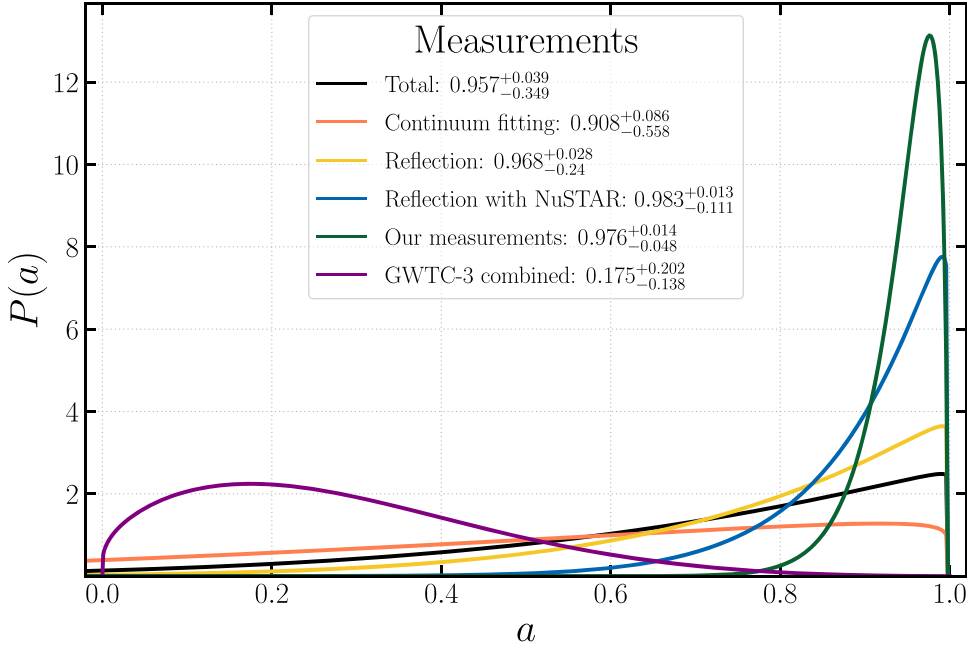


Figure 20. The spin distribution in XBs inferred based on all the measurements presented in Figure 19 and in Table 6. The black curve shows the combined distribution of all spins obtained through continuum fitting and relativistic reflection. The orange curve shows the distribution of continuum fitting measurements, and the yellow curve shows the distribution of all measurements obtained through the relativistic reflection method. The blue curve shows the subset of all reflection measurements (yellow curve) that were obtained using NuSTAR data. The green curve represents the distribution inferred using only the 10 measurements in this paper and is a subset of the blue curve. For comparison, we indicate the spin distribution measured in BBH mergers, presented in GWTC-3 in purple. The values quoted in the figure legend represent the modes and 1σ credible intervals of the distributions.

theoretical assumptions and numerical resolution of the models used, which can likely lead to biases in the measurements.

We plot the combined distributions in Figure 20. The orange curve shows the distribution of XB BH spin measurements obtained through continuum fitting. The green curve shows the distribution inferred based on the 10 measurements presented in this paper, which is a subset of the blue curve, showing the distribution inferred based on all measurements made using relativistic reflection on NuSTAR data. The blue curve is a subset of the yellow curve, which shows the distribution of all XB spin measurements obtained through relativistic reflection. The black curve shows the combined distribution of all XB spin measurements, obtained through both relativistic reflection (yellow) and continuum fitting (orange). For reference, we compare this with the spin distribution inferred by The LIGO Scientific Collaboration et al. (2021b) based on all the GW signals from BBH mergers presented in GWTC-3, shown in purple.

The spin distributions in BBHs and in XBs are clearly in disagreement. Fishbach & Kalogera (2022) compared the distribution of spins in the previous version of the GWTC (GWTC-2, Abbott et al. 2021a) to the distribution of BH spins in high-mass X-ray binaries (HMXBs), inferred from three sources (LMC X-1, Cyg X-1, and M33 X-7). Despite the very limited sample size and despite only using the values measured through continuum fitting, Fishbach & Kalogera (2022) conclude that the HMXB and BBH spin distributions disagree at the $\geq 99.9\%$ level. However, they conclude that the spin distribution of BHs in low-mass X-ray binaries (LMXBs) agrees with that of HMXBs. There is value in attempting to compare the BBH sample to HMXBs only, since HMXBs are candidates for evolving to produce BBH systems. However, it is worth mentioning that studies have shown that neither Cyg X-1 (Belczynski et al. 2011) nor M33 X-7 (Ramachandran et al.

2022) are likely to evolve to produce a BBH system, but Neijssel et al. (2021) concluded that Cyg X-1 could potentially form a BBH system, but one that is unlikely to merge within 14 Gyr. Additionally, works such as Gallegos-Garcia et al. (2022) find that at most 20% of BBHs originate from HMXB systems formed through Case-A mass transfer and at most 11% of Case-A HMXBs evolve into BBH systems. Furthermore, Liotine et al. (2022) find that the probability that a detectable HMXB will form a BBH system that can merge within a Hubble time is $\sim 0.6\%$.

Here, we highlight a comparison of all BH spins in XBs obtained through continuum fitting and relativistic reflection to the spins in BBHs. We performed a two-sample Kolmogorov–Smirnov test (K-S test; Smirnov 1939) in order to quantify the probability that the two observed distributions of spins in BBHs and XB are drawn from the same unknown underlying distribution. Using the distributions shown in Figure 20, we generated 10^5 samples of 50 “measurements” randomly drawn from the XB population and 200 “measurements” drawn from the BBH population, simulating the existing sample sizes. Then, we performed the two-sample K-S test and analysed the distribution of probabilities produced. When comparing the BBH distribution with all spin measurements in XB, we find that the highest probability across the 10^5 tests is $p \sim 2 \times 10^{-6}$, while when comparing it with the distribution of spins obtained using relativistic reflection, the highest probability was $p \sim 8 \times 10^{-9}$. The median probability across the 10^5 samples in the two cases agrees, $p \sim 9 \times 10^{-16}$. These results clearly state that the distribution of spins in BBHs is different from the observed distribution of BH spins in XB. Since the formation channels that lead to the different spin distributions are likely different, it is important to consider the need to explain both distributions when attempting to provide a unified formation mechanism for all BHs.

5. Discussion

In this work, we analysed the archival NuSTAR observations of a sample of 24 XB sources containing BHs that do not have previous spin constraints using relativistic reflection on NuSTAR data. We measured 10 new BH spins. In 14 cases, we were unable to obtain a BH spin measurement. The 10 new measurements represent an increase in the sample size of BH spin measurements obtained through the relativistic reflection method using NuSTAR data of nearly 40%, and an increase of nearly 25% in the sample size of all relativistic reflection measurements. Four of the 10 sources wherein we measure the spin using reflection have previous spin constraints from continuum fitting. Interestingly, in three of the four sources, our relativistic reflection measurements disagree with the spins obtained through continuum fitting (MAXI J1820+070, H 1743-322, and 4U 1543-47), while for 4U 1957+11 our measurement is consistent within the uncertainties with that obtained through continuum fitting.

With the exception of V4641 Sgr, the new spin measurements have very high values, $a > 0.95$, with all values being larger than 0.8 within 1σ . This is consistent with the spin distribution in XBs (Fishbach & Kalogera 2022). It is unlikely that the relativistic reflection method is biased to measure high BH spins, as low spins produce spectral shapes that are less blurred, and therefore easier to distinguish from the underlying continuum. Additionally, low and moderate spins are still detected by works such as Wang et al. (2018), Draghis et al. (2021b), Jana et al. (2021b), and Jia et al. (2022). However, one cannot exclude the possibility that there is an observational bias, making highly spinning BHs easier to detect. Vasudevan et al. (2016) explain that due to selection effects of flux-limited observations, the BH spin distribution measured in AGNs is biased toward high values, but they also argue that this effect should not be directly applicable to stellar-mass galactic BHs. Hirai & Mandel (2021) explain that HMXBs should only become observable if the companion star has a Roche lobe filling factor above 0.8–0.9. A BH rotating in the retrograde direction or slowly in the prograde direction will have a large ISCO radius; when paired with a high Roche lobe filling factor of the companion, this might not allow enough room for the formation of an accretion disk around the BH, with matter plunging directly toward the compact object. If an accretion disk cannot be formed, the XB will not be observed, biasing our observations toward high spin values.

At the same time, one cannot exclude the possibility that the intrinsic spin distribution of BHs in XBs strongly favors high spins. Due to the short lifetimes of HMXBs (van den Heuvel 1976; Iben et al. 1995), we know that the observed high spins (see, e.g., Parker et al. 2015; Jana et al. 2021b) must be natal. Works such as Fragos & McClintock (2015) argue that the high spins in galactic LMXBs can be explained through long episodes of highly efficient accretion. However, it is important to acknowledge that a BH must accrete 80% of its initial mass to increase its spin from $a = 0$ to $a = 0.9$ and 122% of its initial mass to increase its spin from $a = 0$ to $a = 0.99$ (Bardeen 1970; Belczynski et al. 2008), so a limited reservoir of matter might prevent significant spin changes even in LMXBs. Additionally, works such as Draghis et al. (2023) find that even the BHs in intermediate-mass XBs or LMXBs can be born with high spins, not requiring significant accretion.

We measured 10 high BH spins, with nine of them approaching the maximal possible value. However, only three

of the 10 sources show resolved radio jets or “cannonball” ejections: MAXI J1820+070 (Homan et al. 2020), H 1743-322 (Hao & Zhang 2009), and GRS 1758-258 (Martí et al. 2002). This suggests that a high BH spin is not sufficient for the production of resolvable radio jets, and that the observability of the ejecta is likely more strongly influenced by the system’s properties such as the mass accretion rate in the system, the orbital period of the binary, the surrounding interstellar medium (ISM), and even the distance to the system.

The reported uncertainties of our measurements are purely statistical, and the systematic uncertainties are likely to be smaller, yet not negligible. As the BH spin and inclination of the inner disk influence spectral features similarly, we show all the individual spin and inclination measurements for all observations treated in this work in Figure 21, aiming to highlight any possible correlation between the two parameters in the models. While there appears to be a positive trend, it is largely due to the measurements of MAXI J1820+070.

In Figure 22, we show the spin and inclination measurements obtained from the 19 observations of MAXI J1820+070, with the transparency of the points being proportional to the ratio of the reflected to total flux in the observation, which were used to weight the measurements when computing the combined measurement. The combined measurements for spin and inclination are shown through solid lines, while their uncertainties are presented through the shaded regions. Previously, any of those measurements could have been reported in the literature, but by looking at all the observations we obtain a value that is not biased by observation-specific peculiarities and which more clearly reflects the true value of the parameters. MAXI J1820+070 was one of the brightest XBs ever observed, and with it being extensively observed in a comprehensive manner across the electromagnetic spectrum, the existing data set makes this source an anchor in our understanding of the electromagnetic emission coming from stellar-mass BHs.

Figure 21 also shows that few spin measurements take low or negative values, most originating from observations of 4U 1957+11. In Figure 23, we show the inclination versus spin parameter space for the 10 observations of 4U 1957+11, with the transparency of the points being proportional to the ratio of the reflected to total flux. Similar to Figure 22, the solid lines and shaded regions represent the values and uncertainties obtained while combining the individual measurements, respectively. While there are some low and negative spin measurements, those come from observations in which reflection is not as strong, with the combined measurements being dominated by the observations in which reflection is more strongly present. Figures 22 and 23 highlight the importance of analysing all available observations with the aim of reducing any possible systematic uncertainties of our measurements.

Having such a large data set produced through consistent models and assumptions and with uniform systematic uncertainties also allows us to look into the systematic effects of the parameters in the models on the spin measurements. In Figures 24 and 25, we show all the individual spin measurements presented in this paper, in relation with the Fe abundance (A_{Fe}) and reflection fraction (R) predicted by the models, respectively. While it appears that the models prefer high Fe abundances and low reflection fractions, there is no apparent direct correlation between these values and the spin

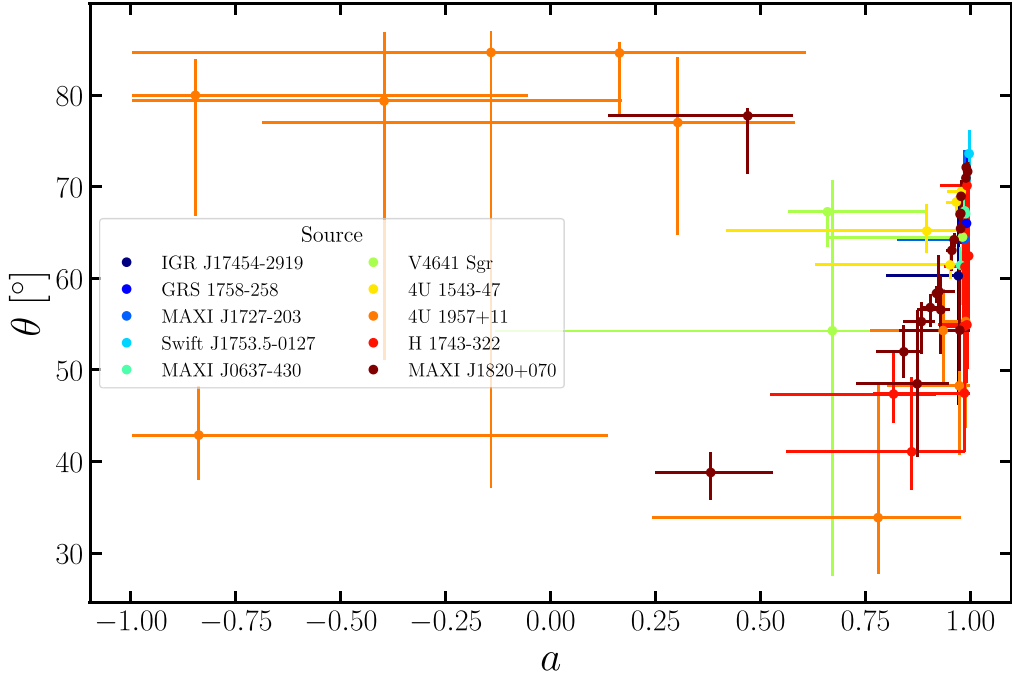


Figure 21. Inclination of the inner accretion disk θ vs. spin a measurements resulting from all observations analysed in this paper. The different colors represent measurements of the spin and inclination of different sources.

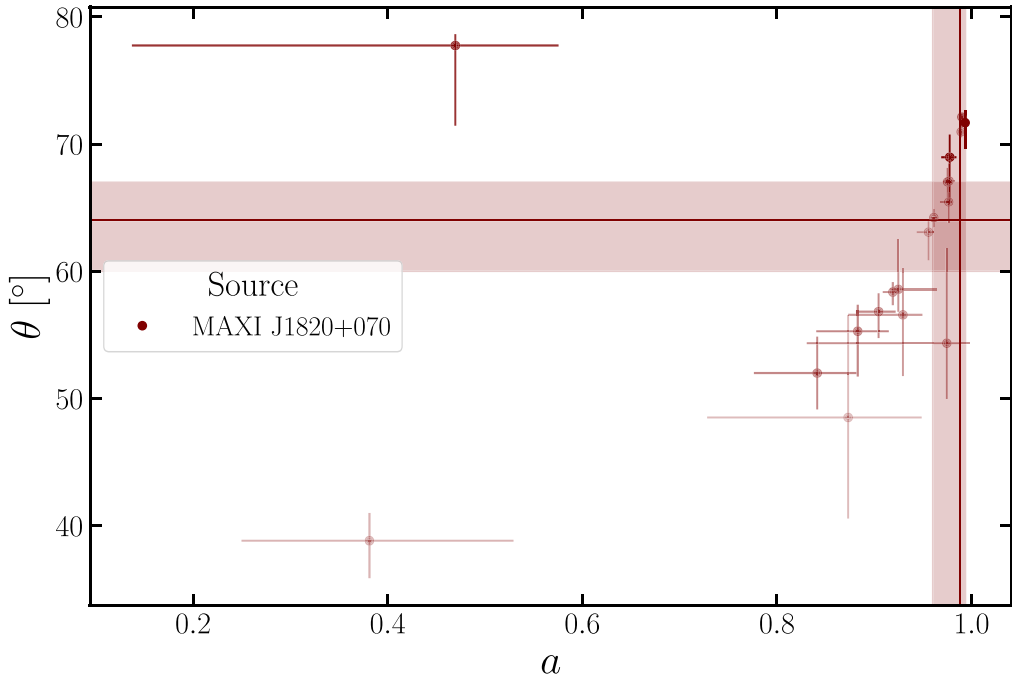


Figure 22. Inclination of the inner accretion disk θ vs. spin a measurements resulting from all observations of MAXI J1820+070. The transparency of the points is proportional to the ratio of the reflected flux to the total flux in the 3–79 keV band, which were used as weighting when combining the posterior distributions. The solid horizontal and vertical lines represent the modes of the combined distributions for the two parameters, with the shaded regions indicating the 1σ credible intervals of the combined measurements.

measurements. Additionally, we can begin to look into the general behavior of the models by highlighting correlations between other parameters. For example, in Figure 26 we show the Fe abundances in all measurements in comparison with the reflection fractions. In this case, no direct correlation is present. However, such parameter correlations can also be treated at the level of each individual fit through the posterior distributions obtained through the MCMC runs. While inspecting the corner

plots showing trends in the posterior distributions of the parameters, no obvious correlations affecting the spin were found. Still, on occasion, degeneracies between parameters were present. Such examples include the correlation between the outer emissivity index q_2 and the breaking radius R_{br} parameterizing the coronal emissivity, which often lead to unphysically low values of q_2 and high values of R_{br} due to the inability of the data to constrain the parameters. Due to the

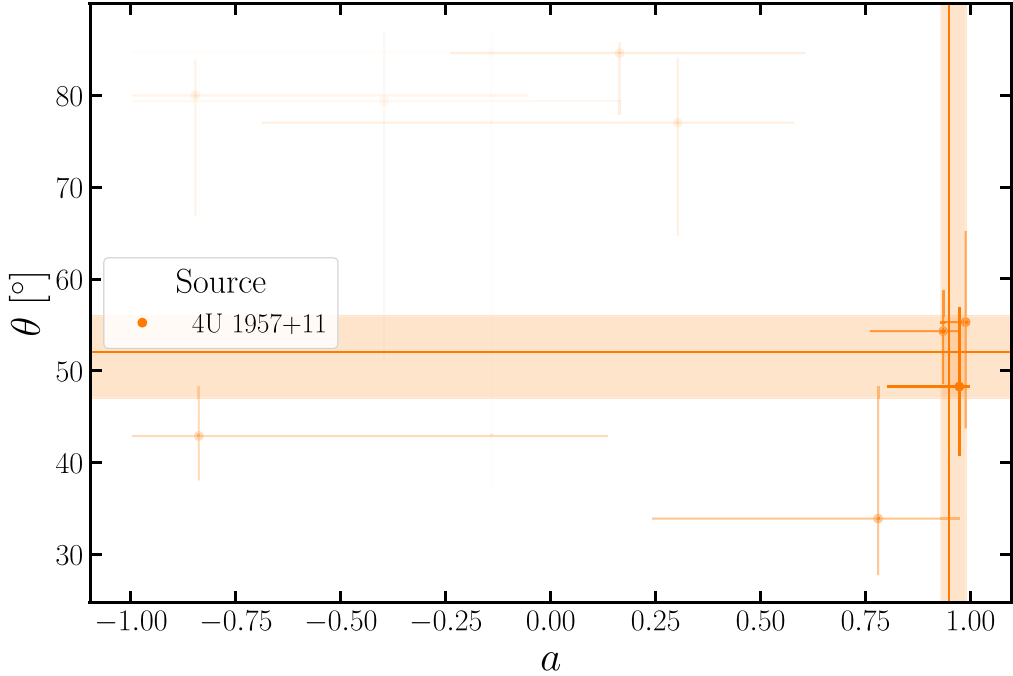


Figure 23. Inclination of the inner accretion disk θ vs. spin a measurements resulting from all observations of 4U 1957+11. The transparency of the points is proportional to the ratio of the reflected flux to the total flux in the 3–79 keV band, which were used as weighting when combining the posterior distributions. The solid horizontal and vertical lines represent the modes of the combined distributions for the two parameters, with the shaded regions indicating the 1σ credible intervals of the combined measurements.

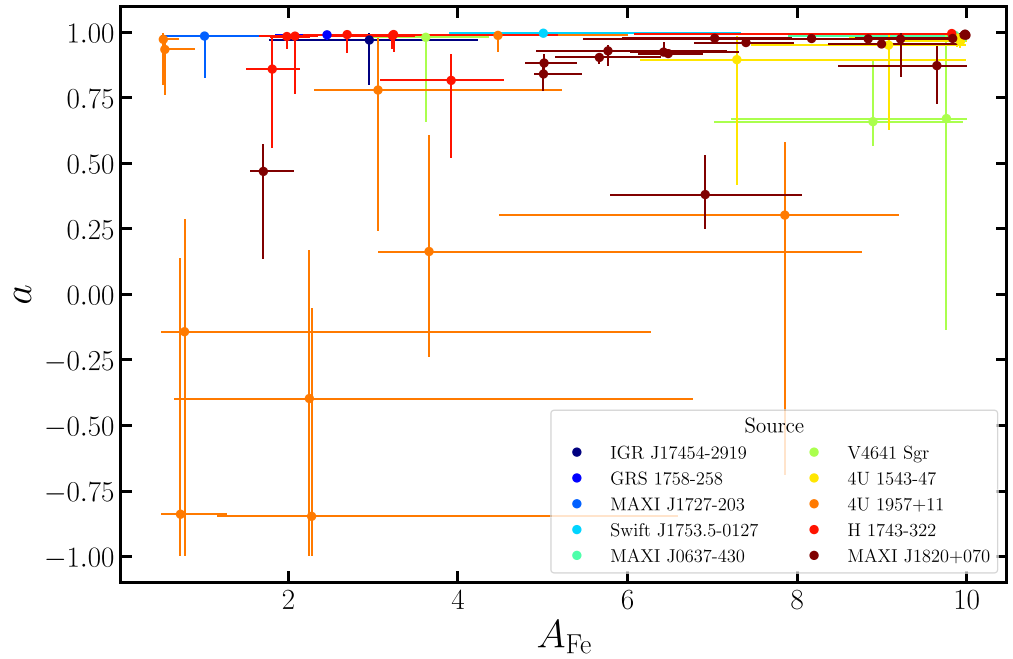


Figure 24. Spin a vs. iron abundance A_{Fe} measurements resulting from all observations analysed in this paper. The different colors represent measurements of the spin and Fe abundance for different sources.

large number of parameters, the scale of a complete treatment of the parameter space is substantial and beyond the scope of this work and will be treated in a future paper, in which we also plan to expand the sample size of spin measurements with existing measurements reanalyzed using the same assumptions of this paper.

Based on the entire GWTC-3 sample, The LIGO Scientific Collaboration et al. (2021b) concluded that most BHs in BBH

systems are slowly rotating. However, a few rapidly rotating BHs were identified in this sample, such as GW190412 (either the spin of the more massive component is $a_1 = 0.44^{+0.16}_{-0.22}$; Abbott et al. 2020b; or the spin of the less massive component is $a_2 = 0.88^{+0.11}_{-0.24}$; Mandel & Fragos 2020; but see the discussion of Zevin et al. 2020), GW190517_055101 ($a_1 = 0.86^{+0.13}_{-0.15}$; Abbott et al. 2021a), GW190403_051519 ($a_1 = 0.92^{+0.07}_{-0.22}$; The LIGO Scientific Collaboration et al. 2021c), or

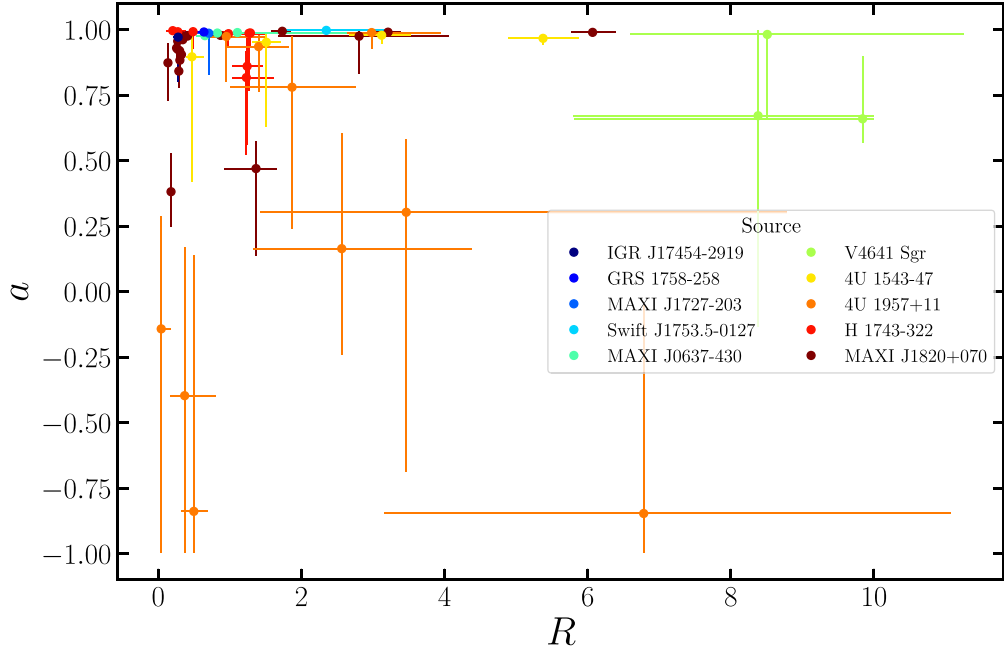


Figure 25. Spin a vs. reflection fraction R measurements resulting from all observations analysed in this paper. The different colors represent measurements of the spin and reflection fraction for different sources.

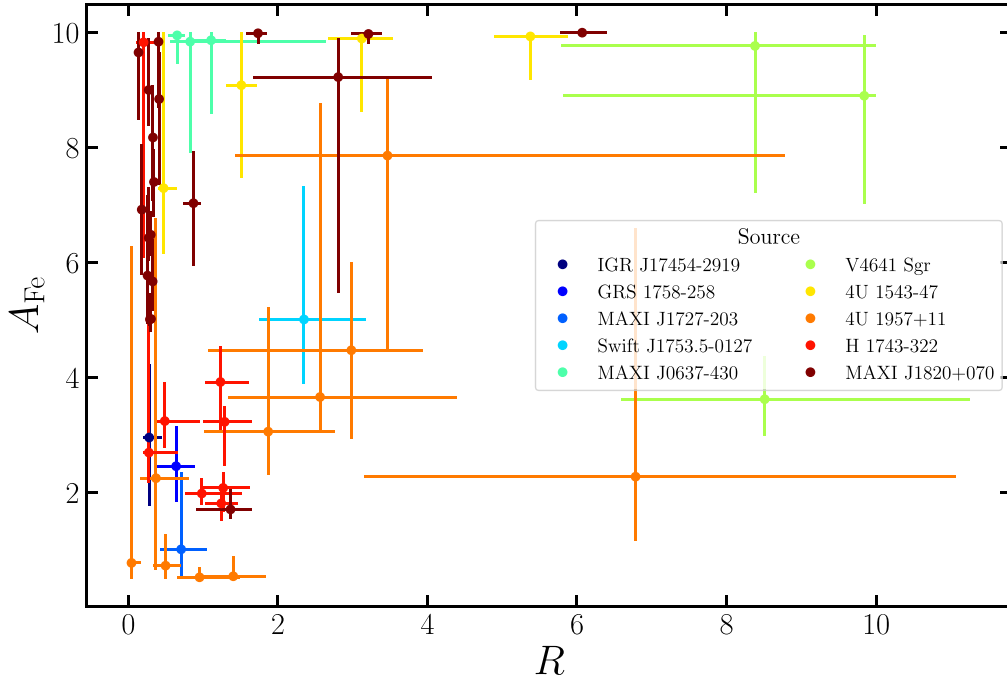


Figure 26. Iron abundance A_{Fe} vs. reflection fraction R measurements resulting from all observations analysed in this paper. The different colors represent measurements of the reflection fraction and Fe abundance for different sources.

GW191109_010717 ($a_l = 0.83^{+0.15}_{-0.58}$; The LIGO Scientific Collaboration et al. 2021a). The formation of BBH systems is a topic of debate, and the current preferred view is that the entire observed distribution cannot be explained through a single formation channel (see, e.g., Zevin et al. 2021 for a detailed view on BBH formation channels). Fishbach et al. (2022) find that based on the existing sample of GW measurements, at most 26% of the underlying BBH population originates from ‘‘hierarchical

mergers’’ (repeated mergers of smaller BHs). While works such as Olejak & Belczynski (2021) argue that the observed distribution of BBHs is consistent with formation from isolated binaries, Gallegos-Garcia et al. (2022) find that at most 20% of BBHs originate from HMXB systems formed through Case-A mass transfer and that at most 11% of Case-A HMXB systems evolve into BBHs and XBs are not only observed to be different (Fishbach & Kalogera 2022), but are intrinsically different. In the

future, expanding and comparing the two spin samples will allow placing better constraints on BH formation and evolution mechanisms.

The authors wish to thank the anonymous reviewer, whose comments helped clarify and enhance this manuscript. P.D. would also like to thank Jiachen Jiang, Camille Liotine, and Monica Gallegos-Garcia for useful discussions that helped improve the paper. A.Z. is supported by NASA under award number 80GSFC21M0002. J.A.T. acknowledges partial support from NASA through NuSTAR Guest Observer grants 80NSSC20K0644 and 80NSSC22K0059.

Software: Astropy (Astropy Collaboration et al. 2013, 2018), emcee (Foreman-Mackey et al. 2013), numpy (Harris et al. 2020), matplotlib (Hunter 2007), scipy (Virtanen et al. 2020), pandas (Reback et al. 2022; McKinney 2010), corner (Foreman-Mackey 2016), iPython (Pérez & Granger 2007), Xspec (Arnaud 1996), relxill (Dauser et al. 2014; García et al. 2014).

Appendix A Choice of Source and Background Regions

The choice of background region adopted in this work is somewhat uncommon when handling NuSTAR data. The common practice in the community is to adopt a circular source region of a certain radius ($\sim 100''$) and a circular background region of the same size, placed in an area of the detector that is not contaminated by the source flux or any stray light that is being detected (for a discussion on stray light in NuSTAR data, see Madsen et al. 2017; Grefenstette et al. 2021). This process requires the user to manually identify the position of the source and background regions in relation to the image coordinates on the detector.

In order to simplify, automate, and increase the reproducibility of the spectral extraction process, we adopted circular regions of radius equal to $120''$ for extraction of the source spectrum, centered at the position of the source in the header of events file of the observation, for each of the detectors. This choice for the position of the source region was made in order to avoid the possibility that the coordinates available in the literature for some sources are uncertain and therefore bias the spectral extraction process. For the background region, we used annular regions centered at the position of the source, with an inner radius of $200''$ and an outer radius of $300''$. First, this reduces the arbitrariness of the choice of position of the background region. Second, this method samples a much larger detector area when constructing the background spectrum. However, for bright sources, the $200''$ inner radius of the annulus might be too small, leading to source photons being included in the background. This is potentially important for sources that have a low flux at high energies, as an increase in flux in the background spectrum would lead to the source spectra becoming background-dominated at lower energies.

We tested this effect by extracting source and background spectra from the observation 80502324004 of MAXI J0637-430, using five combinations of source and background regions. The spectra obtained are shown in Figure 27, together with the residuals of the fit to the best-performing reflection model for this observation (see Section 3.5). The error bars on the background points were omitted for visual clarity. Additionally, we binned the spectra using three different methods: the “optimal” binning scheme (Kaastra & Bleeker 2016), or by

requiring a minimum S/N of 5 and of 10 in each spectral bin. The five combinations of source and background regions are as follows: Case 1– $120''$ radius circular source region and annular background region with $200''$ inner radius and $300''$ outer radius, centered at the position of the source; Case 2– $120''$ radius circular source region and $120''$ radius circular background region, placed as far as possible on the detector; Case 3– $90''$ radius circular source region and $90''$ radius circular background region, placed as far as possible on the detector; Case 4– $150''$ radius circular source region and $150''$ radius circular background region, placed as far as possible on the detector; and Case 5– $120''$ radius circular region and annular background region with $300''$ inner radius and $600''$ outer radius, centered at the position of the source.

The source spectrum is practically unchanged regardless of the size of the source region, with no significant differences even at high energies. The background spectra show changes between the five different cases, mainly at low energies. The background spectra extracted using the region in Case 1 (used throughout the analysis in this paper) produces a background rate at 3 keV an order of magnitude larger than, e.g., Case 2 and 3 (i.e., a $120''$ or $90''$ circular background region placed far on the detector from the source region). However, when comparing to Cases 4 and 5, the background rate is only ~ 5 times higher in Case 1. Given that the sources treated in this paper have high fluxes at low energies, the difference in background spectra should not influence the quality of the data and the obtained results. Given the goal of automatizing the spectral extraction process, Case 5 would produce the ideal combination of source and background spectra. However, in Case 5, with the significantly increased size of the annular extraction region, the risk of the region overlapping with regions on the detector dominated by stray light during observations is increased, likely influencing the background spectra more than the difference between Case 1 and 5 would.

At high energies, the background spectra are consistent regardless of the choice of extraction region. However, different binning schemes can lead to the appearance of the source spectra becoming background-dominated at lower energies, the clearest being Case 3 when requiring all bins to have a minimum S/N of 10. For the same case, different binning techniques clearly indicate that the background spectra dominate over the source spectra above ~ 60 keV. Interestingly, the binning techniques requiring a minimum S/N often have difficulties in treating the background spectra, creating apparent streaks. However, the error bars on the fluxes in the background bins are larger than the variation trend seen in Cases 1–4. Nevertheless, it appears that optimal binning better handles background spectra.

With the different cases of source and background regions and different binning schemes producing visually no difference at high energies and changes of little importance at low energies, it is important to quantify the difference produced when fitting the data with a model. We fit all spectra shown in Figure 27 with the best-performing `relxill` model for this particular observation in our analysis. The best-fit values for the temperature of the accretion disk, BH spin, inner accretion disk inclination, power law index, and disk ionization are shown in Figure 28. The different colors of the points represent the five cases presented in Figure 27, and the different markers represent the binning scheme used, with the circles, squares, and diamonds representing the optimal binning scheme, and the

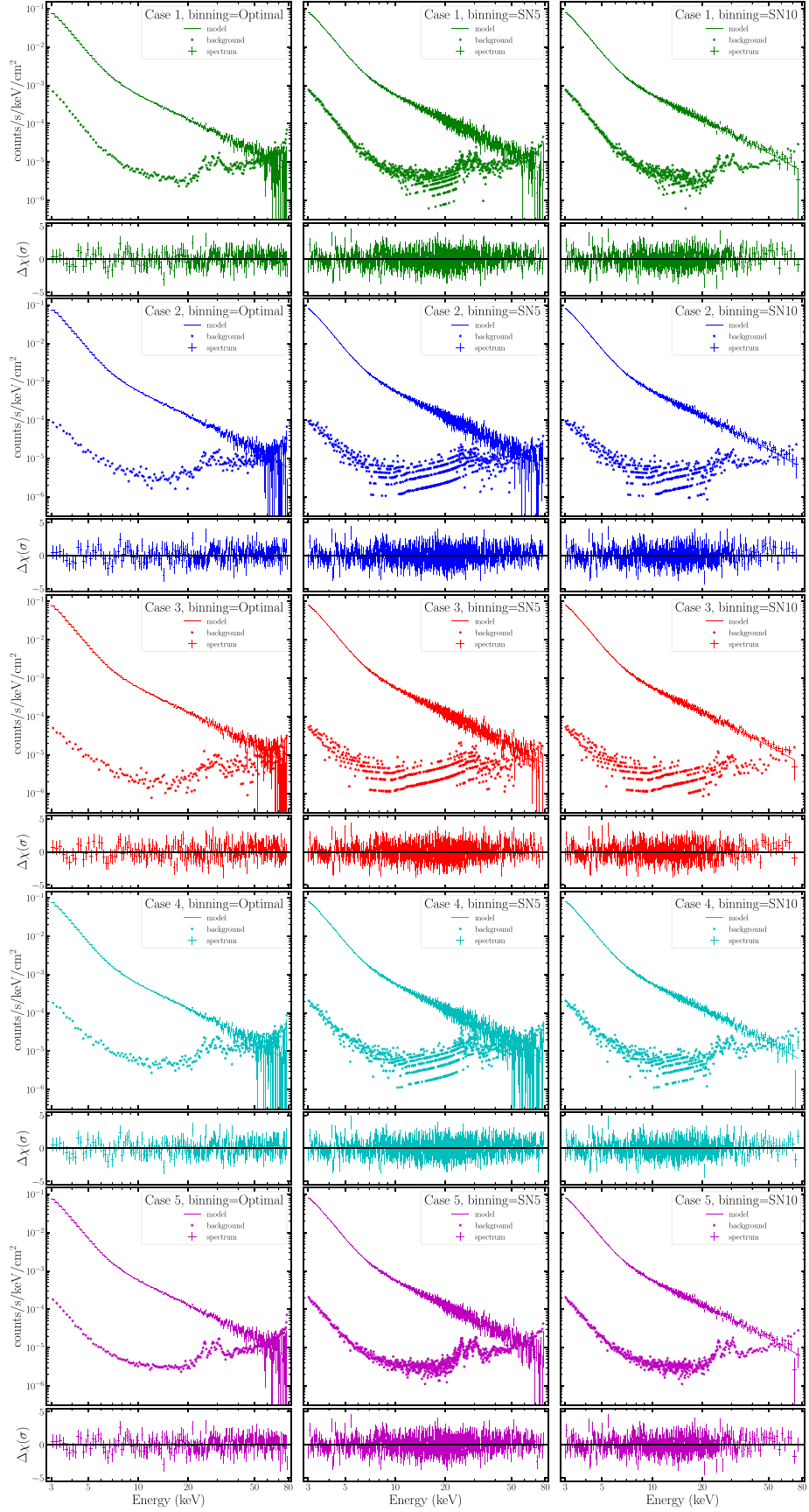


Figure 27. Source and background FPMA spectra from observation 80502324004 of MAXI J0637-430, together with the residuals produced when fitting with the best-performing reflection model, obtained using five different cases of source and background spectra extraction regions (indicated by different colors, in different rows), and three different binning techniques (shown in the three different columns). See the text in Appendix A for additional explanations.

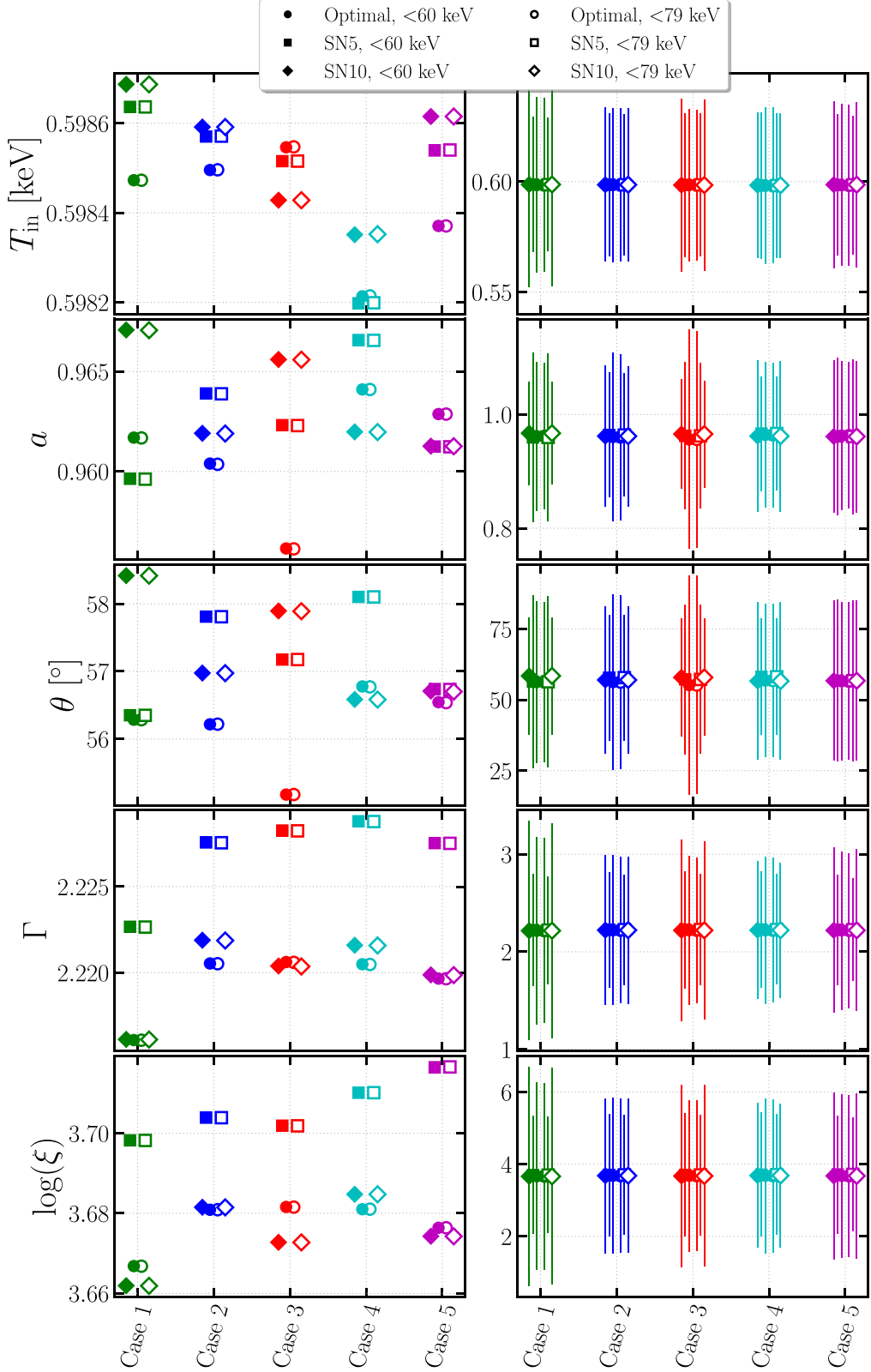


Figure 28. Comparison of parameter values that produce the best fit to the spectra obtained in the five source and background region extraction cases highlighted in Figure 27 and discussed in Appendix A, for different spectral binning schemes and high-energy truncation of the fitted spectrum. The left panels show only the best-fit values, while the right panels also show the uncertainties on the measurements obtained directly from the covariance matrix of the fit. See the text in Appendix A for additional explanations.

S/Ns of 5 and of 10, respectively. The filled markers indicate the results of fitting the spectra in the 3–60 keV band, while the empty markers indicate the results of fitting the spectra in the

entire 3–79 keV NuSTAR band. The left panels show only the value of the parameters for which the best-fit solution was achieved, while the right panels also show the uncertainty of

the parameters, computed as the square root of the diagonal element in the covariance matrix of the fit. This uncertainty is used to produce the proposal distribution for the walkers in the MCMC analysis.

It is important to mention that these measurements are made only by fitting one of the two NuSTAR spectra obtained during one observation (FPMA in this case), and fitting both spectra jointly is likely to reduce the variation between the parameters and to decrease the size of the uncertainties shown in the right panels. Truncating the spectra at 60 keV as opposed to 79 keV has no obvious impact on the best-fit parameters, with the only noticeable difference being that fitting the spectra up to 79 keV produces slightly smaller uncertainties on some parameters. The difference between the best-fit parameters found when fitting spectra extracted using the five different cases for the region size, shape, and location is comparable with the difference produced when using different binning techniques. However, the variability in the best-fit parameters is negligible when compared to the size of the errors. As these fit parameters are only used for the proposal distribution in the MCMC analysis, the results will not be significantly influenced by this variability induced by the different choices of the source and background regions and of the binning scheme used.

Therefore, throughout the analysis, we continue using Case 1 for the extraction of source and background spectra, as it increases the ability to automate our spectra extraction pipeline when compared to Cases 2–4, and it reduces the risk of producing biased background spectra due to stray light when compared to Case 5, at the cost of producing increased background spectra at low energies, which appear to have no significant impact on the result. We continue using the optimal binning scheme, as it leads to similar results with the other binning techniques, while producing spectra with fewer spectral bins compared to the other techniques, which helps reduce the time required to fit the spectra. We mention that the optimal binning scheme still produces bins with enough counts that using χ^2 statistics is still appropriate.

Appendix B Algorithm to Combine Measurements

The script used to combine measurements takes the posterior distributions of the individual parameters obtained through the MCMC runs and maps them to the $[0, 1]$ interval. Then, it then generates a beta distribution with the probability density function (PDF) described by:

$$\text{PDF}(x) = \frac{x^{\alpha-1}(1-x)^{\beta-1}}{B(\alpha, \beta)}, \quad (\text{B1})$$

where $B(\alpha, \beta) = \frac{\Gamma(\alpha)\Gamma(\beta)}{\Gamma(\alpha+\beta)}$ and Γ is the Gamma function, $\Gamma(a) = \int_0^\infty t^{a-1}e^{-at}dt$. This distribution has two parameters, α and β , which we determine through a Bayesian analysis in order to describe the combined measurement. We assume uniform priors for α and β , but we require that $\alpha > 1$, $\beta > 1$, and $(\alpha + \beta) < 171.5$. The first two requirements come from the definition of the beta distribution, and the third is dictated by numerical limitations of the used programming language: $\Gamma(171.5) \sim 9.5 \times 10^{307}$. This number is so large that when computing the value of $B(\alpha, \beta)$, any combination of α, β for which $\alpha + \beta \geq 171.5$ returns $B(\alpha, \beta) = 0$ due to division by a

very large number. This then leads to division by zero when computing the value of the PDF at a given location.

The total likelihood of a parameter combination is evaluated by summing the (logarithm of the) likelihood of the parameter combination describing each individual measurement. As the posterior distributions for the parameter are normalized in the same way as the beta distribution, we quantify how well the beta distribution together with a parameter combination describes the spin measurement by taking the ratio of the area under the minimum of the two curves to the area under the maximum of the two curves, evaluated over the $[0, 1]$ interval. When computing the total likelihood by summing the (logarithm of the) individual likelihoods for each measurement, we weight each measurement in the sum by the ratio of the reflected flux to the total flux in the 3–79 keV band during the observation. This way, we weight observations with stronger reflection more than those with weaker reflection, as they are more likely to allow us to separate the reflection component from the underlying continuum and better constrain the parameters.

As an example of how our likelihood function behaves, Figure 29 illustrates our attempt to fit a Gaussian function defined on the $[0, 1]$ interval, with a mean of $\mu = 0.8$ and a standard deviation of $\sigma = 0.1$. The left panels show the Gaussian function (in black) and three attempted models shown in green: a beta distribution (top panel), delta distribution (middle panel), and a uniform distribution (bottom panel). All curves are normalized in the same way. On the right, we show the minimum of the two curves in blue and the maximum of the two in red. In order to maximize the likelihood, our function attempts to maximize the minimum of the two curves and to minimize the maximum of the two. The method becomes more intuitive upon inspection of the top right panel in Figure 29: our code aims to increase the blue curve (minimum of the two) and to decrease the red one (maximum of the two). This way, the minimum and maximum are most similar, translating to a better fit of our beta distribution to the initial assumed distribution (in this example) and to the data (in real usage).

To test the ability of our script to combine measurements and recover the underlying distribution, we adopted a Gaussian distribution of some given mean and standard deviation and generated a number of Gaussian measurements with position probabilities given by the initial assumed PDF. We then used our script to combine all “measurements” in order to infer the underlying distribution, with the main goal of recovering its mode and credible interval.

Four examples are shown in the four panels of Figure 30. The black curves represent the assumed underlying Gaussian distributions, and the dashed green curves show the beta distributions representing the best fit of our algorithm to the distribution underlying all “measurements.” The top left panel simulates an attempt to combine 10 measurements around a mean of $\mu = 0.7$, with a standard deviation $\sigma = 0.1$. Both the mode and the credible interval of our inferred distribution matches the true values very closely. We note that due to numerical artifacts caused by the limited number of computation iterations, the truth mode and credible intervals of the assumed distribution (black curve) differ very slightly from the values assumed when generating the distributions. This example is very applicable to combining multiple inclination measurements. While the example shows distributions defined

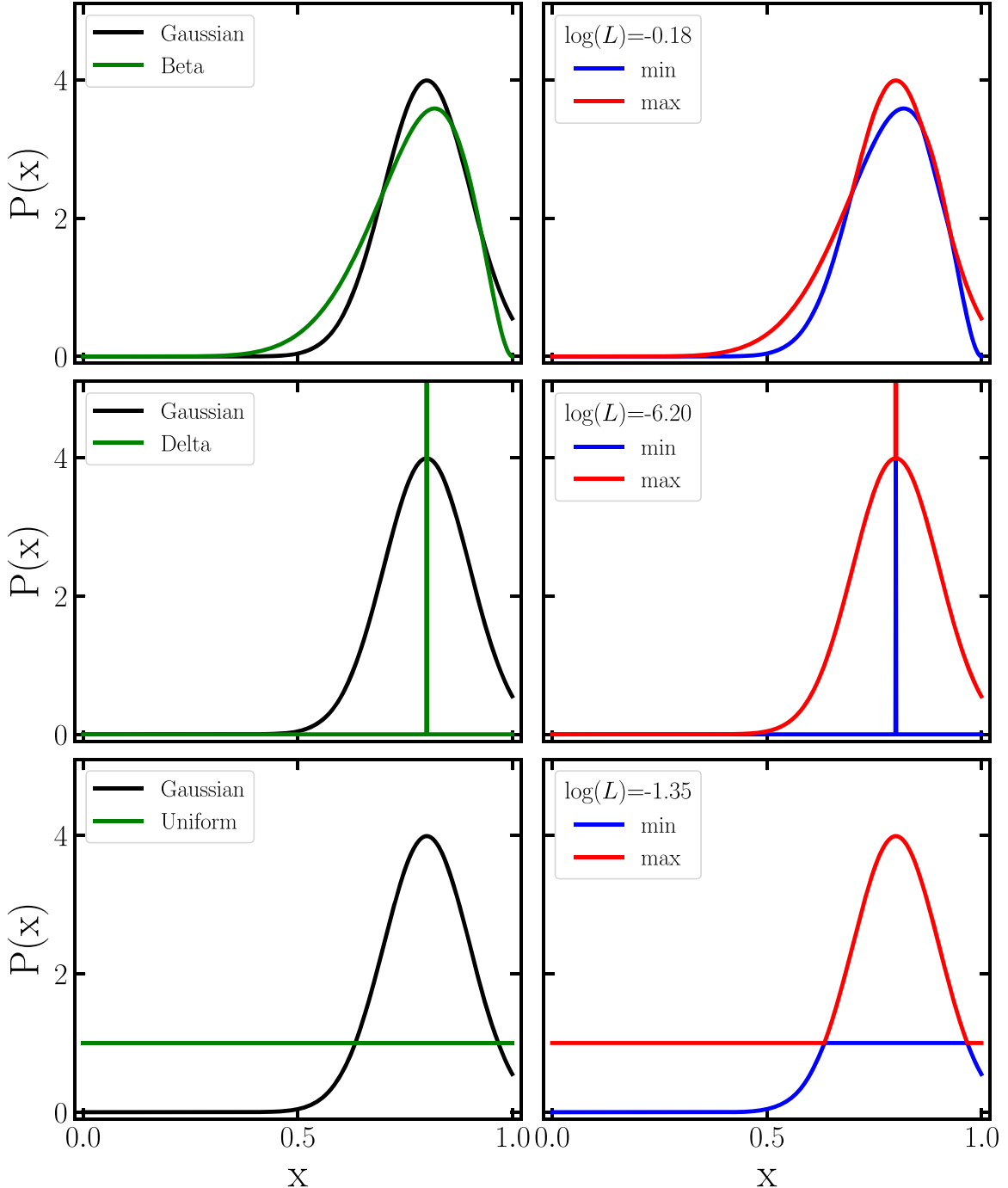


Figure 29. Illustration of the behavior of the likelihood function used when combining measurements. The left panels show a Gaussian distribution with a mean of 0.8 and a standard deviation of 0.1 (in black), for which we compute the likelihood of overlap using three distribution, shown in green: beta (top), delta (middle) and uniform (bottom). The right panels show the minimum overlap of the two distributions presented in the right panels in blue and the maximum of the two in red. The legends in the right panels contain the logarithm of the computed likelihood, which our analysis aims to maximize.

on the $[0, 1]$ interval, one could combine inclination measurements through a change of variable.

The top right panel shows an attempt to combine five measurements generated around a mean of $\mu = 0.97$ and a standard deviation of $\sigma = 0.05$. This example illustrates the usability of combining spin measurements clustered around the maximal value. In this case, the inferred distribution (green dashed line) again closely recovers the assumed underlying distribution, with the mode and credible intervals of the assumed and derived distributions being in good agreement. In

this case, the derived distribution appears to be slightly shifted toward lower spin values, likely due to the requirement of the beta distribution to return to a value of zero at the edge of the interval.

The bottom panels of Figure 30 show an attempt to combine three measurements drawn from a Gaussian with a mean of $\mu = 0.5$ and a standard deviation of $\sigma = 0.05$. The left panel shows the combined distribution when all three measurements are weighted equally, well recovering the assumed distribution. The right panel weights the second measurement (shown

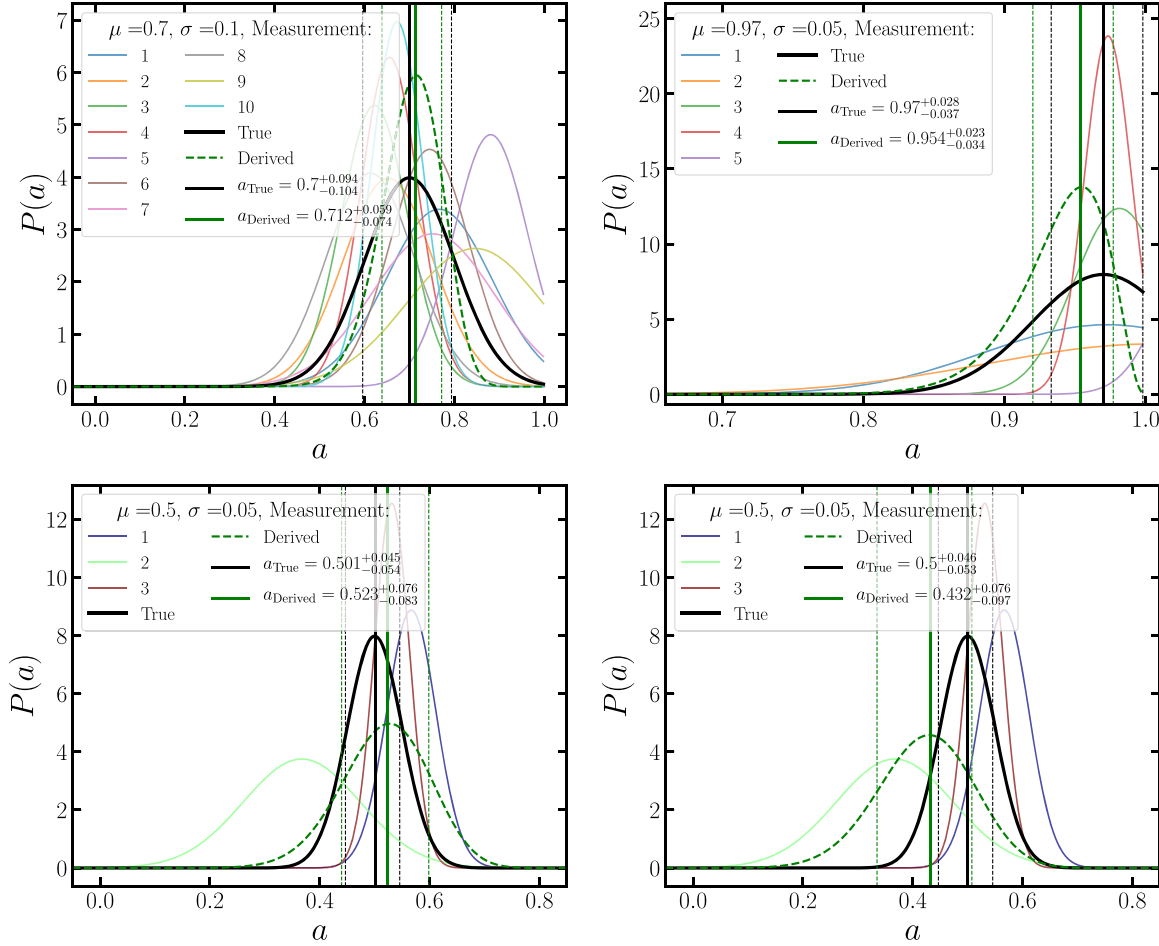


Figure 30. Top left: combining 10 Gaussian “measurements” generated from a Gaussian distribution of median $\mu = 0.7$ and $\sigma = 0.1$ (shown through the solid black curve). Our combined measurement is shown through the dashed green curve, and the solid vertical green and black lines represent the modes of the true and inferred distributions, respectively, with the vertical dashed lines representing the 1σ credible intervals. Top right: combining five Gaussian “measurements” generated from a Gaussian distribution of median $\mu = 0.97$ and $\sigma = 0.05$. The lines’ descriptions are consistent with the previous panel. Note the different, reduced parameter range of the x -axis. Bottom left: combining three Gaussian “measurements” generated from a Gaussian distribution of median $\mu = 0.5$ and $\sigma = 0.05$. Bottom right: same as the bottom left panel, but we weight the second “measurement” eight times as much as the other two, influencing the inferred distribution toward that value.

through the solid green line) eight times more than the other two measurements. The inferred distribution much better recovers the second “measurement,” which was more heavily weighted, while also slightly accounting for the other two measurements.

Often, when multiple observations of the same source are available, an option is to fit the spectra jointly, linking parameters that are expected to stay constant between observations. In this case, the BH spin and the inclination of the inner accretion disk could be linked between observations. The constraints on the parameters would simultaneously account for all the data that are being fit, providing more credible measurements. However, fitting multiple NuSTAR spectra with complicated models quickly becomes a task too computationally intensive, which requires unfeasible times to run. In order to test the robustness of our result combining method against the possibility of fitting the spectra jointly with the parameters linked, we fit two of the three observations of MAXI J0637-430 used in the analysis presented in Section 3.5 jointly. We fit the spectra of the two observations in the 3–50 keV band, linking the BH spin, the inclination of the inner disk, and the column density along the line of sight, and

allowed all other parameters to vary freely, as described in Section 2.1.

Fitting the spectra jointly using $\text{TBabs} * (\text{diskbb} + \text{powerlaw})$ returns $\chi^2/\nu = 1651.15/634$, with clear signs of reflection. Similarly to the individual fits, the best-performing models in terms of χ^2 that account for reflection are $\text{TBabs} * (\text{diskbb+relxill})$, returning $\chi^2/\nu = 707.67/619$, and $\text{TBabs} * (\text{diskbb+relxillD})$ with $\log(n) = 19$, returning $\chi^2/\nu = 710.5/622$. The latter performs significantly better in terms of DIC, with $\Delta\text{DIC} = 200$ better than the former. Therefore, we report the measurements based on the $\text{TBabs} * (\text{diskbb+relxillD})$ with $\log(n) = 19$ MCMC run. We find $a = 0.980^{+0.005}_{-0.009}$ and $\theta = 59^{+3}_{-2}$ degrees. In comparison, when fitting the spectra individually and combining the results using our algorithm, we find $a = 0.97 \pm 0.02$ and $\theta = 62^{+3}_{-4}$ degrees. The results formally agree well within their uncertainties, suggesting that our method produces results that are robust and precise. However, it is worth noting that the combined result also takes advantage of the third available observation. The quoted statistical uncertainties on both the spin and inclination measurements are larger when combining the measurements when compared to the measurements based on a joint fit. This is linked to the fact that the errors quoted are

simply statistical, and the combined measurement begins to include systematic errors, which are likely to contribute significantly.

Appendix C Sources Wherin No Measurement Was Possible

C.1. XTE J1859+226

NuSTAR observed XTE J1859+226 once (ObsID 90701305002) for 41 ks. This observation was described by Draghis et al. (2021a). The spectra are background-dominated above ~ 20 keV. Fitting with the power law model returns $\chi^2/\nu = 187/208$ when the data are binned to have a minimum S/N = 5, and $\chi^2/\nu = 304/340$ when using optimal binning. No reflection features are apparent and a spin measurement is not possible.

C.2. 4U 1755-338

4U 1755-338 was observed once by NuSTAR (ObsID 90601313002), and the observation was first described by Draghis et al. (2020a). During the observation, the source was in a “high/soft” state, with the emission being dominated by the accretion disk. The source is detected up to an energy ~ 25 keV. Fitting the spectra using diskbb+powerlaw produces a good fit, returning $\chi^2/\nu = 416/374$. No reflection features are apparent.

C.3. M31 ULX-1 (CXOM31 J004253.1+411422)

The position of M31 ULX-1 was covered by 11 NuSTAR observations: ObsIDs 50026001002, 50026001004, 50111001002, 50110001002, 50110001004, 50101001002, 50110001006, 50201001002, 50302001002, 50302001004, and 50302001006. The source is not detected in any of the 11 observations.

C.4. M31 ULX-2 (XMMU J004243.6+412519)

There are four NuSTAR observations of the region containing M31 ULX-2: ObsIDs 50302001002, 50302001004, 50302001006, and 30365002002. The source is not detected in any of the four observations.

C.5. XTE J1748-288

NuSTAR observation 40012019001 was pointed at $\sim 8'$ from XTE J1748-288, placing the known location of the source close to the edge of the detectors. However, the source was quiescent during the NuSTAR observation and not detected.

C.6. SS 433

SS 433 is an XB that is best known for launching extended relativistic jets ($v = 0.26c$; Margon & Anderson 1989) that are loaded with baryons (see, e.g., Marshall et al. 2013). The X-ray spectrum of the source is dominated by emission from the variable and precessing jets, complicating efforts to detect emission from the inner disk. Moreover, the jets may be launched because SS 433 harbors a compact object that is accreting far above its Eddington limit (e.g., Fabrika et al. 2015). Especially in this case, the central engine may be enshrouded within an optically thick spherical flow, or at least partially obscured by a vertically extended disk that further serves to obscure signatures from the innermost accretion flow.

Therefore, despite emerging evidence that SS 433 may harbor a BH rather than a neutron star (e.g., Picchi et al. 2020), SS 433 fails several of our criteria for examination, and it is excluded from our analysis. However, Fogantini et al. (2023) performed an analysis of the spectra obtained from the 10 NuSTAR observations of SS 433.

C.7. XTE J0421+560

XTE J0421+560 is the X-ray counterpart of CI Camelopardalis, which is believed to be a B[e] star. The nature of the compact object in the system is not constrained, and Ishida et al. (2004) argued that the emission from the system during quiescence does not allow placing constraints on the nature of the compact object, but that the ASCA observations taken during the 1998 outburst of the source broadly point toward the compact object being a white dwarf. Constraints on the nature of a compact object can be placed through spin measurements: a spin higher than $a = 0.7$ (Lo & Lin 2011) indicates that it must be a BH (see, e.g., Draghis et al. 2023 for an example analysis). Therefore, we chose to analyse this source despite a lack of clear evidence of it harboring a BH.

The spectra from ObsID 90201040002 of XTE J0421+560 do not require a diskbb component. We fit the spectra in the 3–20 keV band. Fitting with powerlaw gives $\chi^2/\nu = 103.2/95$. The two best-performing models are TBabs * relxillD with $\log(n) = 19$ with $\chi^2/\nu = 92.37/87$ and TBabs * relxill with $\chi^2/\nu = 93.41/87$.

Running MCMC on both models, the chains produce similar DICs, 109.07 and 109.42, respectively. In both cases, the spin is low, $a < 0.26$. However, running steppar between -0.998 and 0.998 in spin shows differences of $\Delta\chi^2 = 0.1$ across the entire parameter space. Even though reflection is evident in this observation, the spin cannot be constrained given the quality of the data.

C.8. IC 10 X-1

There is one NuSTAR observation of IC 10 X-1 (ObsID 30001014002). Using the continuum fitting method, Steiner et al. (2016) measured the spin of the BH in IC 10 X-1 to be $a = 0.85^{+0.04}_{-0.07}$ (90% confidence).

Fitting the 3–20 keV spectrum with TBabs * (diskbb + powerlaw) produces a good fit, with $\chi^2/\nu = 111.91/96$. Replacing the power law component with models from the relxill family significantly improves the fit, with the best-performing model TBabs * (diskbb+relxilCp) returning $\chi^2/\nu = 81.10/86$. We find that the fits are unable to constrain the BH spin. 68% of the posterior samples in the MCMC run take spin values $a \leq 0.17$. This measurement could be biased toward low values by constraining the accretion disk to extend all the way to the ISCO. Still, assuming the mass and distance estimates from Steiner et al. (2016) ($M \sim 15 M_\odot$ and $d \sim 800$ kpc), and given the 3–20 keV flux in the NuSTAR observation, this would result in an Eddington fraction of $\sim 3\%$, well within the expected theoretical range for which the inner disk is expected to extend to the ISCO. Additionally, the environment around the BH is likely to be significantly more complicated than the simplistic assumption of this model. As the S/N of the observation is low, we do not pursue more complicated models.

C.9. M33 X-7

There are two NuSTAR observations that cover the position of the source (ObsID 50310001002 and 50310001004). M33 X-7 is not detected during the two observations, taken in 2017 March and July. No spin measurement was possible.

C.10. M33 X-6

In the same two NuSTAR observations as for M33 X-7 (ObsID 50310001002 and 50310001004), the source M33 X-6 is clearly detected. For ObsID 50310001002 we fit the spectra in the 3–15 keV band, while for ObsID 50310001004 we fit in the 3–10 keV band. For the former, fitting the 3–15 keV spectra with $\text{TBabs} * \text{powerlaw}$ returns $\chi^2/\nu = 95.91/80$, while the best-performing reflection model $\text{TBabs} * \text{relxilllp}$ returns $\chi^2/\nu = 90.75/73$. Similarly, for ObsID 50310001004, fitting with $\text{TBabs} * \text{powerlaw}$ produces a good fit, returning $\chi^2/\nu = 54.72/50$, while the best reflection model $\text{TBabs} * \text{relxill}$ returns $\chi^2/\nu = 50.48/41$, with the improvement in statistic not being justified by the increase in the number of free parameters. In both cases, the addition of a reflection component is not justified statistically.

C.11. M33 X-8

There are two NuSTAR observations of M33 X-8 (ObsID 50310002001 and 50310002003) in which the source is clearly detected. Fitting the 50310002001 spectra in the 3–15 keV band using $\text{TBabs} * (\text{diskbb} + \text{powerlaw})$ returns $\chi^2/\nu = 118.97/89$, while the best-performing reflection model $\text{TBabs} * (\text{diskbb} + \text{relxilCp})$ returns $\chi^2/\nu = 116.20/80$. For the 50310002003 observation, also fitting in the 3–15 keV band, the $\text{TBabs} * (\text{diskbb} + \text{powerlaw})$ model returns a good fit, with $\chi^2/\nu = 60.72/86$, while the best-performing reflection model $\text{TBabs} * (\text{diskbb} + \text{relxilD})$ with $\log(n) = 19$ fixed returns $\chi^2/\nu = 55.89/78$. The statistical improvement owed to the addition of reflection is not justified by the increase in the number of free parameters, suggesting that reflection is not statistically significant.

C.12. IGR J17451-3022

There is one NuSTAR observation in the direction of this source (ObsID 30601014003), but the offset between the position of IGR J17451-3022 and the pointing of NuSTAR was $\sim 9.3'$, meaning that the system was near the edge of the field of view of NuSTAR. This observation cannot be used for a spin measurement.

C.13. Swift J1357.2-0933

There are three NuSTAR observations of Swift J1357.2-0933. For ObsID 90201057002, we fit the 3–79 keV spectrum; for 90301005002, we fit the 3–50 keV spectrum; and for 90501325002, we fit the 3–20 keV spectrum. We fit all three observations jointly. The quality of the fits does not improve through the addition of a diskbb component nor by including absorption through TBabs , as expected given that the estimated column density along the line of sight is relatively small, $\sim 3 \times 10^{20} \text{ cm}^{-2}$.

Fitting the six spectra with powerlaw gives a cumulative $\chi^2/\nu = 928.89/808$. Visually inspecting the residuals does not reveal clear signs of reflection. When fitting the spectra with a power law with a high-energy cutoff (cutoffpl), the quality

of the fit improves significantly, to $\chi^2/\nu = 874.08/805$. We tested whether reflection is present by fitting the spectra first with xillver (producing $\chi^2/\nu = 858.98/797$), and with the models in the relxill family. Of those, relxillCp produced the best statistic, returning $\chi^2/\nu = 861.18/787$. Note that the value of χ^2 is worse than in the case of unblurred reflection (xillver), suggesting that any reflection does not originate from the innermost regions of the accretion disk.

We computed the AIC and BIC for the four mentioned models. Of those, cutoffpl and xillver produce the lowest values, suggesting stronger statistical significance. Comparing the two models, cutoffpl performs better than xillver in terms of both AIC and BIC producing $\text{AIC} = 79.17$ and $\text{BIC} = 135.64$ versus $\text{AIC} = 80.93$ and $\text{BIC} = 175.05$ for xillver . The lower values of both AIC and BIC produced by fitting the data with cutoffpl when compared to xillver suggests that reflection is not statistically significant in this source, during the three observations.

C.14. Cyg X-3

There are four archival NuSTAR observations of Cyg X-3: ObsIDs 10102002002, 90202051002, 90202051004, and 90502319002. Using the estimates for the BH mass of $2.4_{-1.1}^{+2.1} M_\odot$ (Zdziarski et al. 2013) and for the distance to the system of 7.4 ± 1.1 kpc (McCollough et al. 2016), we conclude that all four observations happened while the source was at an Eddington fraction between the limits for which we expect the accretion disk to extend all the way to the ISCO. Therefore, in principle, all four observations could be used in our analysis.

However, Cyg X-3 is a small BH in a binary with a Wolf-Rayet (WR) star that is feeding the accretion onto the compact object through stellar winds. Therefore, in addition to the high column density along the line of sight due to the location of Cyg X-3 in the plane of the galaxy, we expect a significant amount of absorption and re-emission within the intra-binary medium. Due to the high amount of obscuration within the system, we chose to analyse only the observation obtained while the source was in the hardest state of the ones available. Of the four available NuSTAR observations, ObsID 10102002002 has both the lowest soft flux and highest hard flux, suggesting both that the soft emission from the stellar winds is reduced and that the flux from the corona is enhanced (or less absorbed). This is the same observation treated by Koljonen & Tomsick (2020).

Fitting the spectra obtained from ObsID 10102002002 with the same series of models that we apply to our entire sample returns unacceptable fits. No model is able to properly fit the enhanced emission in the Fe K region. When using the $\text{TBabs} * (\text{diskbb} + \text{powerlaw})$ model, $\chi^2/\nu = 69088.50/456$, and when attempting to account for relativistic reflection by replacing the powerlaw component with relxill returns $\chi^2/\nu = 11347.22/447$. Clearly, the simplistic treatment does not suffice for this source.

A significantly better fit is obtained when introducing two apec components and two zxipcf absorption components to the model, and replacing the powerlaw component with a power law with a high-energy cutoff component (cutoffpl). The first pair of apec and zxipcf was added to describe the effect of the stellar wind from the WR companion, while the second pair was added in order to describe the effects of an accretion disk wind. This model returns $\chi^2/\nu = 1101.06/442$.

While nominally a poor fit, this is a very significant improvement from previous models.

However, while this model includes a contribution from the accretion disk through the `diskbb` component and from the compact corona through the `cutoffpl` component, it does not include reflection features. Therefore, we added a `xillver` component to represent unblurred reflection to test the statistical significance of the presence of reflection. In Xspec parlance, the complete model is `TBabs * zxipcf * zxipcf * (diskbb+cutoffpl+xillver+apec +apec)` and returns $\chi^2/\nu = 620.09/436$. In this model, we set the reflection fraction of the `xillver` component to negative values in order to model only the contribution of reflection. For both `apec` components, the redshift was fixed to zero, and the metal abundance was linked between components, taking a moderate value of ~ 1.5 . For the `zxipcf` components, the one describing the stellar wind had a low ionization ($\log \xi \sim 0.9$), higher covering fraction ($f \sim 0.9$), and lower column density ($N_{\text{H}} \sim 5 \times 10^{23} \text{ cm}^{-2}$), while the component describing the accretion disk wind had a higher ionization ($\log \xi \sim 4$), lower covering fraction ($f \sim 0.7$), higher column density ($N_{\text{H}} \sim 1.8 \times 10^{24} \text{ cm}^{-2}$), and was allowed to have a negative redshift (blueshift), taking a value of $z \sim -0.043$, which if real would correspond to a wind being launched at $\sim 4\%$ of the speed of light. The photon index of $\Gamma \sim 2.4$ and the high-energy cutoff of $E_{\text{cut}} \sim 10 \text{ keV}$ were linked between `xillver` and `cutoffpl`. The predicted ionization of the `xillver` component is moderately low ($\log \xi \sim 1.3$), indicative of distant reflection, while the Fe abundance is subsolar $A_{\text{Fe}} \sim 0.62$. The inclination θ and reflection fraction R are unconstrained. The values reported here come from the direct Xspec fit, and no MCMC analysis was run on the parameter space, which is why no uncertainties are reported for the parameters, and we report these values only for completeness.

When substituting the `xillver` component with the relativistically blurred `relxill` version, the quality of the fit decreases to $\chi^2/\nu = 641.13/431$. While it is possible that the fit converged to a local minimum, the quality of the fit appeared insensitive to the relativistic reflection parameters. Using a model with both `relxill` and `xillver` produces $\chi^2/\nu = 619.78/427$, with the improvement in χ^2 not being justified by the increase in the number of free parameters. Since the quality of the fit decreases through the addition of relativistically blurred reflection when compared to unblurred reflection, we conclude that while reflection is present, it likely happens at relatively large distances from the compact object, making a spin measurement from the current NuSTAR data unachievable. In the future, pairing NuSTAR or HEX-P (Madsen et al. 2018) data with XRISM (Tashiro et al. 2018) and eventually ATHENA (Barret et al. 2018) will allow distinguishing between the emission from stellar winds, accretion disk, disk winds, and relativistic reflection to enable spin measurements, and Cygnus X-3 is a prime and exciting candidate for this work.

ORCID iDs

- Paul A. Draghis <https://orcid.org/0000-0002-2218-2306>
 Jon M. Miller <https://orcid.org/0000-0003-2869-7682>
 Abderahmen Zoghbi <https://orcid.org/0000-0002-0572-9613>
 Mark Reynolds <https://orcid.org/0000-0003-1621-9392>

Elisa Costantini <https://orcid.org/0000-0001-8470-749X>
 John A. Tomsick <https://orcid.org/0000-0001-5506-9855>

References

- Abbott, B. P. & Kagra Collaboration 2020a, *LRR*, **23**, 3
 Abbott, B. P., Abbott, R., Abbott, T. D., et al. 2016, *PhRvL*, **116**, 061102
 Abbott, B. P. & LIGO Scientific Collaboration 2019, *PhRvX*, **9**, 031040
 Abbott, R., Abbott, T. D., Abraham, S., et al. 2020b, *PhRvD*, **102**, 043015
 Abbott, R., Abbott, T. D., Abraham, S., et al. 2021a, *PhRvX*, **11**, 021053
 Abbott, R., Abbott, T. D., Abraham, S., LIGO Scientific Collaboration and Virgo Collaboration, et al. 2021b, *PhRvX*, **11**, 021053
 Agrawal, P. C. 2006, *AdSpR*, **38**, 2989
 Akaike, H. 1974, *ITAC*, **19**, 716
 Arnaud, K. A. 1996, in ASP Conf. Ser. 101, Astronomical Data Analysis Software and Systems V, ed. G. H. Jacoby & J. Barnes (San Francisco, CA: ASP), 17
 Astropy Collaboration, Price-Whelan, A. M., Sipőcz, B. M., et al. 2018, *AJ*, **156**, 123
 Astropy Collaboration, Robitaille, T. P., Tollerud, E. J., et al. 2013, *A&A*, **558**, A33
 Atri, P., Miller-Jones, J. C. A., Bahramian, A., et al. 2020, *MNRAS*, **493**, L81
 Bardeen, J. M. 1970, *Natur*, **226**, 64
 Bardeen, J. M., & Pettersson, J. A. 1975, *ApJL*, **195**, L65
 Bardeen, J. M., Press, W. H., & Teukolsky, S. A. 1972, *ApJ*, **178**, 347
 Barret, D., Lam Trong, T., den Herder, J.-W., et al. 2018, *Proc. SPIE*, **10699**, 106991G
 Belczynski, K., Bulik, T., & Bailyn, C. 2011, *ApJL*, **742**, L2
 Belczynski, K., Taam, R. E., Rantsiou, E., & van der Sluys, M. 2008, *ApJ*, **682**, 474
 Bhargava, Y., Belloni, T., Bhattacharya, D., Motta, S., & Ponti, G. 2021, *MNRAS*, **508**, 3104
 Blandford, R. D., & Znajek, R. L. 1977, *MNRAS*, **179**, 433
 Bolton, C. T. 1972, *NPhS*, **240**, 124
 Bonson, K., & Gallo, L. C. 2016, *MNRAS*, **458**, 1927
 Brenneman, L. W., & Reynolds, C. S. 2006, *ApJ*, **652**, 1028
 Burrows, D. N., Hill, J. E., Nousek, J. A., et al. 2005, *SSRv*, **120**, 165
 Chen, Z., Gou, L., McClintock, J. E., et al. 2016, *ApJ*, **825**, 45
 Corral-Santana, J. M., Casares, J., Muñoz-Darias, T., et al. 2016, *A&A*, **587**, A61
 Dauser, T., García, J., Parker, M. L., Fabian, A. C., & Wilms, J. 2014, *MNRAS*, **444**, L100
 Dauser, T., García, J. A., Joyce, A., et al. 2022, *MNRAS*, **514**, 3965
 Dong, Y., García, J. A., Steiner, J. F., & Gou, L. 2020, *MNRAS*, **493**, 4409
 Dong, Y., Liu, Z., Tuo, Y., et al. 2022, *MNRAS*, **514**, 1422
 Draghis, P. A., Balakrishnan, M., & Miller, J. M. 2023, *ApJ*, in press, arXiv:2303.04164
 Draghis, P., Miller, J. M., Balakrishnan, M., et al. 2020a, *ATel*, **13665**, 1
 Draghis, P. A., Miller, J. M., Balakrishnan, M., et al. 2021a, *ATel*, **14512**, 1
 Draghis, P. A., Miller, J. M., Cackett, E. M., et al. 2020b, *ApJ*, **900**, 78
 Draghis, P. A., Miller, J. M., Zoghbi, A., et al. 2021b, *ApJ*, **920**, 88
 El-Batal, A. M., Miller, J. M., Reynolds, M. T., et al. 2016, *ApJL*, **826**, L12
 Event Horizon Telescope Collaboration, Akiyama, K., Alberdi, A., et al. 2019, *ApJL*, **875**, L1
 Fabrika, S., Ueda, Y., Vinokurov, A., Sholukhova, O., & Shidatsu, M. 2015, *NatPh*, **11**, 551
 Feng, Y., Zhao, X., Gou, L., et al. 2022a, *MNRAS*, **516**, 2074
 Feng, Y., Zhao, X., Gou, L., et al. 2022b, *SCPMA*, **65**, 219512
 Feng, Y., Zhao, X., Li, Y., et al. 2022c, *ApJ*, **925**, 142
 Fishbach, M., & Kalogera, V. 2022, *ApJL*, **929**, L26
 Fishbach, M., Kimball, C., & Kalogera, V. 2022, *ApJL*, **935**, L26
 Fogantini, F. A., García, F., Combi, J. A., et al. 2023, *A&A*, **669**, A149
 Foreman-Mackey, D. 2016, *JOSS*, **1**, 24
 Foreman-Mackey, D., Hogg, D. W., Lang, D., & Goodman, J. 2013, *PASP*, **125**, 306
 Fragos, T., & McClintock, J. E. 2015, *ApJ*, **800**, 17
 Gallegos-García, M., Fishbach, M., Kalogera, V., Berry, C. P. L., & Doctor, Z. 2022, *ApJL*, **938**, L19
 García, J., Dauser, T., Lohfink, A., et al. 2014, *ApJ*, **782**, 76
 García, J. A., Steiner, J. F., Grinberg, V., et al. 2018, *ApJ*, **864**, 25
 García, J. A., Steiner, J. F., McClintock, J. E., et al. 2015, *ApJ*, **813**, 84

- Gelman, A., Carlin, J. B., Stern, H. S., & Rubin, D. B. 2004, Bayesian Data Analysis, Texts in Statistical Science Series (2nd ed.; Boca Raton, FL: Chapman & Hall/CRC), <http://www.stat.columbia.edu/~gelman/book/>
- Gendreau, K. C., Arzoumanian, Z., & Okajima, T. 2012, *Proc. SPIE*, 8443, 844313
- George, I. M., & Fabian, A. C. 1991, *MNRAS*, 249, 352
- Gou, L., McClintock, J. E., Liu, J., et al. 2009, *ApJ*, 701, 1076
- Gou, L., McClintock, J. E., Remillard, R. A., et al. 2014, *ApJ*, 790, 29
- Gou, L., McClintock, J. E., Steiner, J. F., et al. 2010, *ApJL*, 718, L122
- Grefenstette, B. W., Ludlam, R. M., Thompson, E. T., et al. 2021, *ApJ*, 909, 30
- Guan, J., Tao, L., Qu, J. L., et al. 2021, *MNRAS*, 504, 2168
- Hao, J. F., & Zhang, S. N. 2009, *ApJ*, 702, 1648
- Harris, C. R., Millman, K. J., van der Walt, S. J., et al. 2020, *Natur*, 585, 357
- Harrison, F. A., Craig, W. W., Christensen, F. E., et al. 2013, *ApJ*, 770, 103
- Hiemstra, B., Méndez, M., Done, C., et al. 2011, *MNRAS*, 411, 137
- Hirai, R., & Mandel, I. 2021, *PASA*, 38, e056
- Homan, J., Bright, J., Motta, S. E., et al. 2020, *ApJL*, 891, L29
- Hunter, J. D. 2007, *CSE*, 9, 90
- Iben, I. J., Tutukov, A. V., & Yungelson, L. R. 1995, *ApJS*, 100, 217
- Ishida, M., Morio, K., & Ueda, Y. 2004, *ApJ*, 601, 1088
- Jana, A., Chang, H.-K., Chatterjee, A., Naik, S., & Safi-Harb, S. 2022, *ApJ*, 936, 3
- Jana, A., Jaisawal, G. K., Naik, S., et al. 2021a, *RAA*, 21, 125
- Jana, A., Naik, S., Chatterjee, D., & Jaisawal, G. K. 2021b, *MNRAS*, 507, 4779
- Jia, N., Zhao, X., Gou, L., et al. 2022, *MNRAS*, 511, 3125
- Kaastra, J. S., & Bleeker, J. A. M. 2016, *A&A*, 587, A151
- Kammoun, E. S., Nardini, E., & Risaliti, G. 2018, *A&A*, 614, A44
- King, A. L., Walton, D. J., Miller, J. M., et al. 2014, *ApJL*, 784, L2
- Kolehmainen, M., & Done, C. 2010, *MNRAS*, 406, 2206
- Koljonen, K. I. I., & Tomsick, J. A. 2020, *A&A*, 639, A13
- Krawczynski, H., Muleri, F., Dovčíak, M., et al. 2022, *Sci*, 378, 6620
- Liotine, C., Zevin, M., Berry, C., Doctor, Z., & Kalogera, V. 2022, arXiv:2210.01825
- Liska, M., Hesp, C., Tchekhovskoy, A., et al. 2021, *MNRAS*, 507, 983
- Liu, J., McClintock, J. E., Narayan, R., Davis, S. W., & Orosz, J. A. 2008, *ApJL*, 679, L37
- Lo, K.-W., & Lin, L.-M. 2011, *ApJ*, 728, 12
- MacDonald, R. K. D., Bailyn, C. D., Buxton, M., et al. 2014, *ApJ*, 784, 2
- Madsen, K. K., Christensen, F. E., Craig, W. W., et al. 2017, arXiv:1711.02719
- Madsen, K. K., Harrison, F., Broadway, D., et al. 2018, *Proc. SPIE*, 10699, 106996M
- Maitra, D., Miller, J. M., Reynolds, M. T., Reis, R., & Nowak, M. 2014, *ApJ*, 794, 85
- Mandel, I., & Fragos, T. 2020, *ApJL*, 895, L28
- Margon, B., & Anderson, S. F. 1989, *ApJ*, 347, 448
- Marshall, H. L., Canizares, C. R., Hillwig, T., et al. 2013, *ApJ*, 775, 75
- Martí, J., Mirabel, I. F., Rodríguez, L. F., & Smith, I. A. 2002, *A&A*, 386, 571
- McCollough, M. L., Corrales, L., & Dunham, M. M. 2016, *ApJL*, 830, L36
- McKinney, W. 2010, SciPy 2010, 56, doi:<https://conference.scipy.org/proceedings/scipy2010/mckinney.html>
- Michell, J. 1784, *Philosophical Transactions of the Royal Society of London*, 74, 35
- Middleton, M. J., Miller-Jones, J. C. A., & Fender, R. P. 2014, *MNRAS*, 439, 1740
- Middleton, M. J., Sutton, A. D., Roberts, T. P., Jackson, F. E., & Done, C. 2012, *MNRAS*, 420, 2969
- Miller, J. M., Gendreau, K., Ludlam, R. M., et al. 2018, *ApJL*, 860, L28
- Miller, J. M., Parker, M. L., Fuerst, F., et al. 2013, *ApJL*, 775, L45
- Miller, J. M., Reynolds, C. S., Fabian, A. C., Miniutti, G., & Gallo, L. C. 2009, *ApJ*, 697, 900
- Miller, J. M., Tomsick, J. A., Bachetti, M., et al. 2015, *ApJL*, 799, L6
- Molla, A. A., Chakrabarti, S. K., Debnath, D., & Mondal, S. 2017, *ApJ*, 834, 88
- Mondal, S. 2010, *ApJ*, 708, 1442
- Mori, K., Hailey, C. J., Mandel, S., et al. 2019, *ApJ*, 885, 142
- Mushotzky, R., Aird, J., Barger, A. J., et al. 2019, *BAAS*, 51, 107
- Nealon, R., Price, D. J., & Nixon, C. J. 2015, *MNRAS*, 448, 1526
- Neijssel, C. J., Vinciguerra, S., Vigna-Gómez, A., et al. 2021, *ApJ*, 908, 118
- Novikov, I. D., & Thorne, K. S. 1973, in BHs (Les Astres Occlus), ed. C. DeWitt & B. DeWitt (New York: Gordon and Breach), 343
- Nowak, M. A., Wilms, J., Pottschmidt, K., et al. 2012, *ApJ*, 744, 107
- Olejak, A., & Belczynski, K. 2021, *ApJL*, 921, L2
- Orosz, J. A., Kuulkers, E., van der Klis, M., et al. 2001, *ApJ*, 555, 489
- Pahari, M., Bhattacharyya, S., Rao, A. R., et al. 2018, *ApJ*, 867, 86
- Park, S. Q., Miller, J. M., McClintock, J. E., et al. 2004, *ApJ*, 610, 378
- Parker, M. L., Tomsick, J. A., Kennea, J. A., et al. 2016, *ApJL*, 821, L6
- Parker, M. L., Tomsick, J. A., Miller, J. M., et al. 2015, *ApJ*, 808, 9
- Pérez, F., & Granger, B. E. 2007, *CSE*, 9, 21
- Picchi, P., Shore, S. N., Harvey, E. J., & Berdyugin, A. 2020, *A&A*, 640, A96
- Pike, S. N., Negoro, H., Tomsick, J. A., et al. 2022, *ApJ*, 927, 190
- Prabhakar, G., Mandal, S., Athulya, M. P., & Nandi, A. 2022, *MNRAS*, 514, 6102
- Pürrer, M., Hannam, M., & Ohme, F. 2016, *PhRvD*, 93, 084042
- Ramachandran, V., Oskinova, L. M., Hamann, W. R., et al. 2022, *A&A*, 667, A77
- Rao, A., & Vadawale, S. V. 2012, *ApJL*, 757, L12
- Reback, J., jbrockmendel, McKinney, W., et al. 2022, pandas-dev/pandas: Pandas v1.4.3, Zenodo, doi:[10.5281/zenodo.6702671](https://doi.org/10.5281/zenodo.6702671)
- Reeves, J., Done, C., Pounds, K., et al. 2008, *MNRAS*, 385, L108
- Reis, R. C., Miller, J. M., Reynolds, M. T., Fabian, A. C., & Walton, D. J. 2012, *ApJ*, 751, 34
- Reis, R. C., Reynolds, M. T., Miller, J. M., et al. 2013, *ApJ*, 778, 155
- Reynolds, C. S. 2021, *ARA&A*, 59, 117
- Reynolds, C. S., & Fabian, A. C. 2008, *ApJ*, 675, 1048
- Rout, S. K., Vadawale, S., & Méndez, M. 2020, *ApJL*, 888, L30
- Salvesen, G., Miller, J. M., Reis, R. C., & Begelman, M. C. 2013, *MNRAS*, 431, 3510
- Schnittman, J. D., Krolik, J. H., & Noble, S. C. 2016, *ApJ*, 819, 48
- Schwarz, G. 1978, *AnSta*, 6, 461
- Schwarzschild, K. 1999, arXiv:physics/9905030
- Shafee, R., McClintock, J. E., Narayan, R., et al. 2006, *ApJL*, 636, L113
- Shafee, R., Narayan, R., & McClintock, J. E. 2008, *ApJ*, 676, 549
- Shakura, N. I., & Sunyaev, R. A. 1973, *A&A*, 500, 33
- Sharma, P., Sharma, R., Jain, C., Dewangan, G. C., & Dutta, A. 2021, *RAA*, 21, 214
- Shaw, A. W., Miller, J. M., Grinberg, V., et al. 2022, *MNRAS*, 516, 124
- Smirnov, N. V. 1939, *Bull. Math. Univ. Moscou*, 2, 3
- Smith, R. K., Brickhouse, N. S., Liedahl, D. A., & Raymond, J. C. 2001, *ApJL*, 556, L91
- Sokal, A. 1996, in Functional Integration: Basics and Applications, NATO Science Series B, Vol. 361, ed. C. DeWitt-Morette, P. Cartier, & A. Folacci (Boston, MA: Springer), 131, https://link.springer.com/content/pdf/10.1007/978-1-4899-0319-8_6.pdf
- Spiegelhalter, D. J., Best, N. G., Carlin, B. P., & Van Der Linde, A. 2002, *Journal of the Royal Statistical Society: Series B (Statistical Methodology)*, 64, 583
- Sreehari, H., Nandi, A., Das, S., et al. 2020, *MNRAS*, 499, 5891
- Stecchini, P. E., D'Amico, F., Jablonski, F., Castro, M., & Braga, J. 2020, *MNRAS*, 493, 2694
- Stefanov, I. Z., & Tasheva, R. P. 2017, arXiv:1711.11398
- Steiner, J. F., McClintock, J. E., Orosz, J. A., et al. 2014, *ApJL*, 793, L29
- Steiner, J. F., McClintock, J. E., & Reid, M. J. 2012, *ApJL*, 745, L7
- Steiner, J. F., McClintock, J. E., Remillard, R. A., et al. 2010, *ApJL*, 718, L117
- Steiner, J. F., Reis, R. C., McClintock, J. E., et al. 2011, *MNRAS*, 416, 941
- Steiner, J. F., Walton, D. J., García, J. A., et al. 2016, *ApJ*, 817, 154
- Tananbaum, H., Gursky, H., Kellogg, E., Giacconi, R., & Jones, C. 1972, *ApJL*, 177, L5
- Tao, L., Tomsick, J. A., Qu, J., et al. 2019, *ApJ*, 887, 184
- Tashiro, M., Maejima, H., Toda, K., et al. 2018, *Proc. SPIE*, 10699, 520
- Tetarenko, B. E., Sivakoff, G. R., Heinke, C. O., & Gladstone, J. C. 2016, *ApJS*, 222, 15
- The LIGO Scientific Collaboration, the Virgo Collaboration, the KAGRA Collaboration, et al. 2021a, arXiv:2111.03606
- The LIGO Scientific Collaboration, the Virgo Collaboration, the KAGRA Collaboration, et al. 2021b, arXiv:2111.03634
- The LIGO Scientific Collaboration, the Virgo Collaboration, et al. 2021c, arXiv:2108.01045
- Thorne, K. S. 1974, *ApJ*, 191, 507
- Tomsick, J. A., Parker, M. L., García, J. A., et al. 2018, *ApJ*, 855, 3
- Tomsick, J. A., Yamaoka, K., Corbel, S., et al. 2009, *ApJL*, 707, L87
- Torres, M. A. P., Casares, J., Jiménez-Ibarra, F., et al. 2020, *ApJL*, 893, L37
- Tursunov, A. A., & Kološ, M. 2018, *PAN*, 81, 279
- van den Heuvel, E. P. J. 1976, in IAU Symp. 73, Structure and Evolution of Close Binary Systems, ed. P. Eggleton, S. Mitton, & J. Whelan (Dordrecht: Reidel), 35
- Vasudevan, R. V., Fabian, A. C., Reynolds, C. S., et al. 2016, *MNRAS*, 458, 2012

- Verner, D. A., Ferland, G. J., Korista, K. T., & Yakovlev, D. G. 1996, *ApJ*, **465**, 487
- Virtanen, P., Gommers, R., Oliphant, T. E., et al. 2020, *NatMe*, **17**, 261
- Vitale, S., Gerosa, D., Haster, C.-J., Chatzioannou, K., & Zimmerman, A. 2017, *PhRvL*, **119**, 251103
- Walton, D. J., Mooley, K., King, A. L., et al. 2017, *ApJ*, **839**, 110
- Wang, Y., Méndez, M., Altamirano, D., et al. 2018, *MNRAS*, **478**, 4837
- Webster, B. L., & Murdin, P. 1972, *Natur*, **235**, 37
- Wilms, J., Allen, A., & McCray, R. 2000, *ApJ*, **542**, 914
- Xu, Y., Harrison, F. A., Kennea, J. A., et al. 2018, *ApJ*, **865**, 18
- Xu, Y., Harrison, F. A., Tomsick, J. A., et al. 2020a, *ApJ*, **893**, 42
- Xu, Y., Harrison, F. A., Tomsick, J. A., et al. 2020b, *ApJ*, **893**, 30
- Zdziarski, A. A., Mikolajewska, J., & Belczynski, K. 2013, *MNRAS*, **429**, L104
- Zevin, M., Bavera, S. S., Berry, C. P. L., et al. 2021, *ApJ*, **910**, 152
- Zevin, M., Berry, C. P. L., Coughlin, S., Chatzioannou, K., & Vitale, S. 2020, *ApJL*, **899**, L17
- Zhao, X., Gou, L., Dong, Y., et al. 2021, *ApJ*, **916**, 108